# Ester-containing imidazolium-type ionic liquid crystals derived from biobased fatty alcohols

*Enrique del Río, Thomas Vidil\*, Wafa Gati, Étienne Grau, Daniel Taton\*, Henri Cramail\**

Univ. Bordeaux, CNRS, Bordeaux INP, LCPO, UMR 5629, F-33600, Pessac, France

*To whom correspondence should be addressed:

thomas.vidil@enscbp.fr,

daniel.taton@enscbp.fr,

henri.cramail@enscbp.fr

**ABSTRACT:** The need to take into account the life cycle of ionic liquids (ILs), from the sourcing of the raw materials involved in their synthesis to their disposal and degradation, has become paramount in the design of new IL-type molecular structures. In the case of 1-alkyl-3-methylimidazolium salts, one of the prominent IL families, there is an increasing demand for synthetic methods involving (i) the substitution of the petro-based alkyl derivatives by readily available bio-sourced surrogates, and (ii) the functionalization of the alkyl tail with hetero-functional groups enabling the (bio)degradation of the IL after use. Herein, a straightforward and industrially viable synthesis of lipidic imidazolium salts is reported, starting from different bio-sourced fatty alcohols, including oleic, stearyl and lauryl alcohols. The procedure is based on the acrylation of the fatty alcohol, followed by the aza-Michael addition of the imidazole group onto the acrylate moiety. Subsequent quaternization, using either methyl iodide or methyl tosylate, provides a library of 1-alkylpropionate-3-methylimidazolium salts with various alkyl chain length (C18, C12, C11) and incorporating different types of counter-anions (iodate, tosylate, tetrafluoroborate). These ester-containing analogs of classical 1-alkyl-3-methylimidazolium salts are all ILs, *i.e.*, with a melting point below 100 °C. In addition, most of them exhibit a liquid crystal behavior and can be referred to as ionic liquid crystals (ILCs). The thermal stability, as well as the phase transitions of these ILs, have been investigated by thermogravimetric analysis and differential scanning calorimetry, respectively, while the molecular structure into the crystalline phase and the mesophase is studied by X-ray scattering. Interestingly, ILCs featuring unsaturated alkyl tails exhibit a low melting point, close to room temperature and the presence of the ester function is shown to provide an enhanced stabilization of the mesophase.

**Keywords**

Imidazolium-based ionic liquids – Ionic liquid crystals – Renewable feedstock – Vegetable oils –

Aza-Michael addition – Smectic-A mesophase – Biodegradable

**Introduction**

Since their discovery in the early 19th century,[1] ionic liquids (ILs) have infiltrated every corner of modern chemistry.[2, 3] Initially foreseen as an alternative to conventional organic solvents,[4] their utility has now been illustrated in virtually all fields of molecular chemistry, including separation[5, 6] and extraction[5, 7-9] technologies, organo-catalysis,[10, 11] electrochemistry,[12, 13] or even biochemistry[14, 15] and material sciences.[16, 17] Among the limitless structural possibilities of ILs,[2] the association of 1-alkyl-3-methylimidazolium cations to weakly-coordinating anions have been center stage over the past decades.[18, 19] The intrinsic asymmetry of the imidazolium cation is indeed a key feature to obtain a liquid salt over a large temperature window.[20]

Moreover, the combination of the $\pi$-$\pi$ interactions of the rigid imidazolium core with the van der Walls interactions of the flexible alkyl tail can promote the formation of mesomorphic phases, as established by Seddon et *al*.[21-23] Imidazolium-based ILs can indeed self-organize into liquid crystalline mesophases,[24] referred to as ionic liquid crystals (ILCs).[25] Interestingly, their excellent solvating properties combined with their anisotropic ordered structures can be exploited to orient the regio- or stereo-selectivity of common organic reactions.[26] For instance, 1-dodecyl-3-methylimidazolium chloride was used to control the *exo/endo* selectivity of the Diels-Alder addition of diethyl maleate onto cyclopentadiene.[26]

Despite their intriguing properties, 1-alkyl-3-methylimidazolium ILs and ILCs are still barely used at an industrial level.[27, 28] One major limitation is their production cost compared to that of conventional organic solvents and building blocks used in the chemical industry.[29] Moreover, their environmental impact is more questionable than initially thought.[30-33] First, imidazolium-type ILs are usually obtained from non-renewable petroleum-based building blocks.[34, 35] On top of that, the

risk of environmental persistence and ecotoxicity, in case of accidental discharge or contamination, is a noteworthy obstacle to their large-scale use.[36] Several studies have shown that 1-alkyl-3-methylimidazolium ILs and ILCs are poorly biodegradable,[37] and can persist in many environmental compartments.[38] Therefore, the potential benefits of their superior chemical and thermal stability do not always balance the downsides that come along.[39]

Greener synthetic pathways to environmentally benign ILs have been envisaged. One solution is to use building blocks obtained from renewable resources.[35, 40, 41] To access lipidic 1-alkyl-3-methylimidazolium ILs,[42-47] the group of Davis et *al*. used long alkyl chains that are readily available from an abundant and cheap renewable feedstock: vegetable oils. The resulting ILs were shown to display thermotropic and/or lyotropic mesophases.[48] Interestingly, the phase transition temperatures could be tuned as a function of the number of unsaturation of the lipidic tail.[44] The synthesis of lipidic 1-alkyl-3-methylimidazolium IL(C)s is based on the direct addition of 1-methylimidazole onto the alkyl halide derived from the corresponding fatty alcohol.[42] They have been used as separating phase in chromatography processes[43, 45, 49] and as electrolytes in supercapacitors and memory devices.[48, 50]

IL(C)s eco-persistence, the other facet of their deleterious impacts on the environment, has been intensively addressed as well.[51] Scammels et *al*. paved the way to the rational design of IL(C)s with enhanced biodegradability[52-56] by incorporating an hydrolyzable ester moiety into the alkyl tail of 1-alkyl-3-methylimidazolium cations.[53] The esters functions enable an enzymatic hydrolysis step, initiating a pathway to further breakdown products. In particular, Scammels et *al*. measured a 100% increase of the biological degradation of 1-(propylacetate)-3-methylimidazolium octylsulfate, as compared to its ester-free counterparts, namely, 1-butyl-3-methylimidazolium octylsulfate.[53] For this reason, 1-(alkylacetate)-3-methylimidazolium were considered as potential

organogelators for personal care preparations, and as biodegradable solvents for the chemical industry.[57, 58] They are usually obtained through the addition of 1-methylimidazole onto $\alpha$-bromoalkylesters,[59, 60] as first reported by Bodor *et al.* in 1980.[60]

Interestingly, the reconsideration of the life cycle of imidazolium-type ILs, from the sourcing of the raw materials used for their synthesis to their disposal and degradation, is related to the functionalization of their *N*-alkyl substituents. In the above-mentioned examples, Davis *et al.* introduced unsaturation by using bio-based building blocks, while Scammels *et al.* inserted esters to promote the biodegradation of the ILs. In other words, the reduction of ILs' environmental impact has become a driving force behind the conception of new imidazolium salts.

In this context, here we report a novel and straightforward synthetic method for the preparation of imidazolium-type ILs featuring a bio-sourced alkyl tail and incorporating an ester function. Saturated and monounsaturated fatty alcohols of various length were functionalized with an acrylate function and grafted onto the imidazolium core, following an approach based on the Michael addition of imidazole onto the acrylate function. The resulting ILs are fully characterized in terms of chemical and thermal properties. For those exhibiting a liquid crystalline behavior, an in-depth characterization of their mesophase was carried out using X-ray scattering. The results are compared with those of more conventional 1-alkyl-3-methylimidazolium IL(C)s. Our new platform features close-to-room temperature IL(C)s that are air and moisture stable on a wide temperature range, while exhibiting a heat-induced degradation for lower temperatures ([200 °C – 250 °C] than benchmark ILs. This higher susceptibility for thermal degradation is attributed to the presence of the ester functionality in their molecular structure.[61] These bio-based and high added-value chemicals have a great potential in processing technologies and in material science, in virtue of their ionic structure and mesomorphism, respectively.
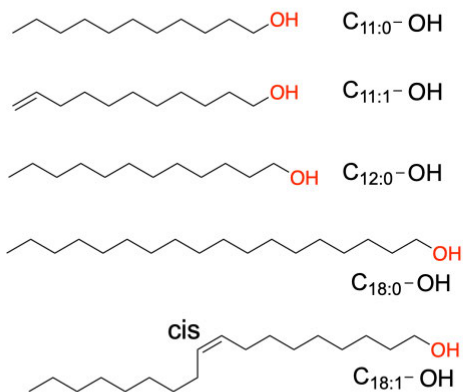
## Results and Discussion

*Synthesis of 1-(alkylpropionate)-3-methylimidazolium IL(C)s, [$C_{x:y}E_{(2)}ImMe$]X*

**A** Synthesis of ester-containing lipidic imidazolium-based IL(C)s
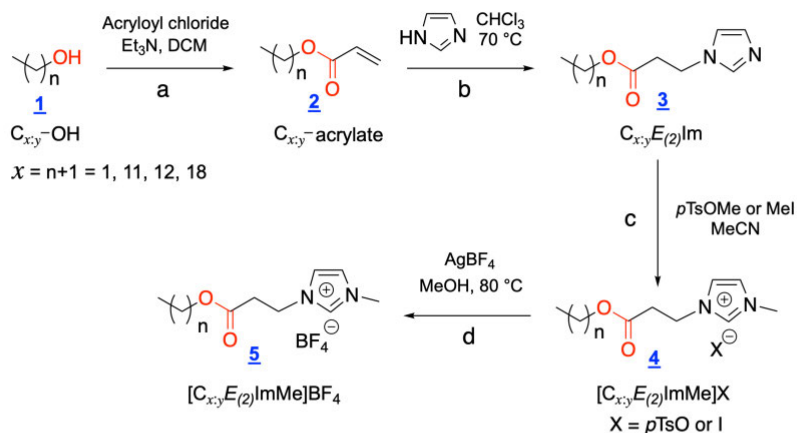


**B** Fatty alcohols used in this study



**C**

| (x:y) | Anion, X | | |
|---|---|---|---|
| | pTsO | I | BF$_4$ |
| (1:0) | • | • | |
| (11:0) | • | • | • |
| (11:1) | • | • | |
| (12:0) | • | • | • |
| (18:0) | • | • | |
| (18:1) | • | • | |

**Scheme 1**: (A) Synthesis of lipidic imidazolium ILs containing an ester function *via* – a – the functionalization of fatty alcohols (1) with an acrylate function followed by – b – the Michael addition of imidazole onto the fatty acrylates (2) and – c – the quaternization of the ester-containing lipidic imidazole (3) with pTsOMe or MeI to yield the corresponding paratoluenesulfonate or iodate ILs (4). The iodate ILs were converted into tetrafluoroborate equivalents (5) *via* anion

metathesis with AgBF$_4$ – d. (B) Chemical structure of the fatty alcohols used in this study, (C) List of the synthesized ionic liquids.

In this work, a new family of lipidic imidazolium IL(C)s is synthesized, starting from readily available and bio-sourced fatty alcohols. The synthetic approach is inspired by works reported by Li et *al.* regarding the synthesis of ester-containing imidazolium salts (Scheme 1A).[62] The synthesis first involves the reaction of the fatty alcohol, C$_{x:y}$-OH (**1**), with acryloyl chloride, to quantitatively afford the corresponding fatty acrylates, **2**. Different types of fatty alcohols, C$_{x:y}$-OH, were used, *x* being the total number of carbon atoms in the fatty chain and *y* the total number of unsaturations (Scheme 1B). In the case of C$_{12:0}$-OH and C$_{18:0}$-OH, the corresponding acrylates, namely, dodecylacrylate (C$_{12:0}$-acrylate) and octadecylacrylate (C$_{18:0}$-acrylate), respectively, were directly obtained from commercial resources and used as received. Methyl acrylate (C$_{1:0}$-acrylate) was used as a short-chain reference in order to examine the distinctive features arising from the fatty analogs.

The aza-Michael addition of imidazole onto the acrylates was then performed in chloroform. The resulting 1-(alkylpropionate)-imidazoles are noted C$_{x:y}E_{(m)}$Im (**3**), where *E* indicates the presence of an ester bond in-between the aromatic core of the imidazole (Im) and the fatty chain (C$_{x:y}$), and *m* is the number of carbon atoms in-between Im and *E*. Herein, for the whole series, *m* = 2. C$_{x:y}E_{(2)}$Im were purified by column chromatography over silica, with the exception of C$_{18:1}E_{(2)}$Im, which was purified by recrystallization. All compounds were isolated with very good yields (~ 85%). They were then quaternized using two strong electrophiles, namely, methyl iodide and methyl *p*-toluenesulfonate, to yield iodide and *p*-toluenesulfonate (*p*TsO) 1-(alkylpropionate)-3-methylimidazolium ILs (**4**), denoted as [C$_{x:y}E_{(2)}$ImMe]I and [C$_{x:y}E_{(2)}$ImMe]*p*TsO, respectively.

The reactions were nearly quantitative. The last step to access the tetrafluoroborate analogs, $[C_{x:y}E_{(2)}ImMe]BF_4$, (**5**), was achieved by anion metathesis between $[C_{x:y}E_{(2)}ImMe]I$ and silver tetrafluoroborate, $AgBF_4$. All the IL(C)s were obtained with an overall yield higher than 80% relatively to the alcohol precursors (**1**). The library of IL(C)s thus synthesized is summarized in Scheme 1C. Their $^1H$ and $^{13}C$ NMR spectra are available in the supplementary information (Figures S1 to S20). The structural integrity of these novel compounds was further confirmed by high-resolution mass spectrometry (HRMS) of the ion couples (see supplementary information). The high-resolution mass spectra in the positive ion mode are available in Figures S21 to S32. This new synthetic strategy is competitive with the more conventional synthesis of lipidic 1-alkyl-3-methylimidazolium ILs, $[C_{x:y}ImMe]X$ (ester-free), reported earlier.[44] Moreover, the yields obtained exceed those of the synthesis of ester-containing lipidic 1-(alkylacetate)-3-methylimidazolium ILs, $[C_{x:y}E_{(1)}ImMe]X$, according to the protocol of Bodor *et al*.[60]

Hereafter, the thermal and structural properties of the synthesized $[C_{x:y}E_{(2)}ImMe]X$ IL(C)s are reported and compared with those of more conventional $[C_{x:y}ImMe]X$ and $[C_{x:y}E_{(1)}ImMe]X$ IL(C)s.

*DSC of $[C_{x:y}E_{(2)}ImMe]X$ IL(C)s*

Prior to DSC measurements, all the ILs were characterized by thermogravimetric analysis under air and nitrogen atmospheres (see supplementary information; Table S1 and Figures S33 to S47). The temperature onset of the thermal degradation of the $[C_{x:y}E_{(2)}ImMe]X$ ILs are found to be approximately 50 °C smaller than those of $[C_{x:y}ImMe]X$ analogs.[22, 63] Advantageously, it has been proven that a higher susceptibility to thermal degradation correlates with a higher biodegradability

in the case of ester-containing $[C_{x:y}E_{(1)}ImMe]X$ ILs.[53] However, the biodegradation of $[C_{x:y}E_{(2)}ImMe]X$ ILs synthesized in this work has not been evaluated. Given their structural analogy with $[C_{x:y}E_{(1)}ImMe]X$ ILs, as well as their susceptibility to heat-induced degradation, it is very likely that they exhibit high biological degradation as well.
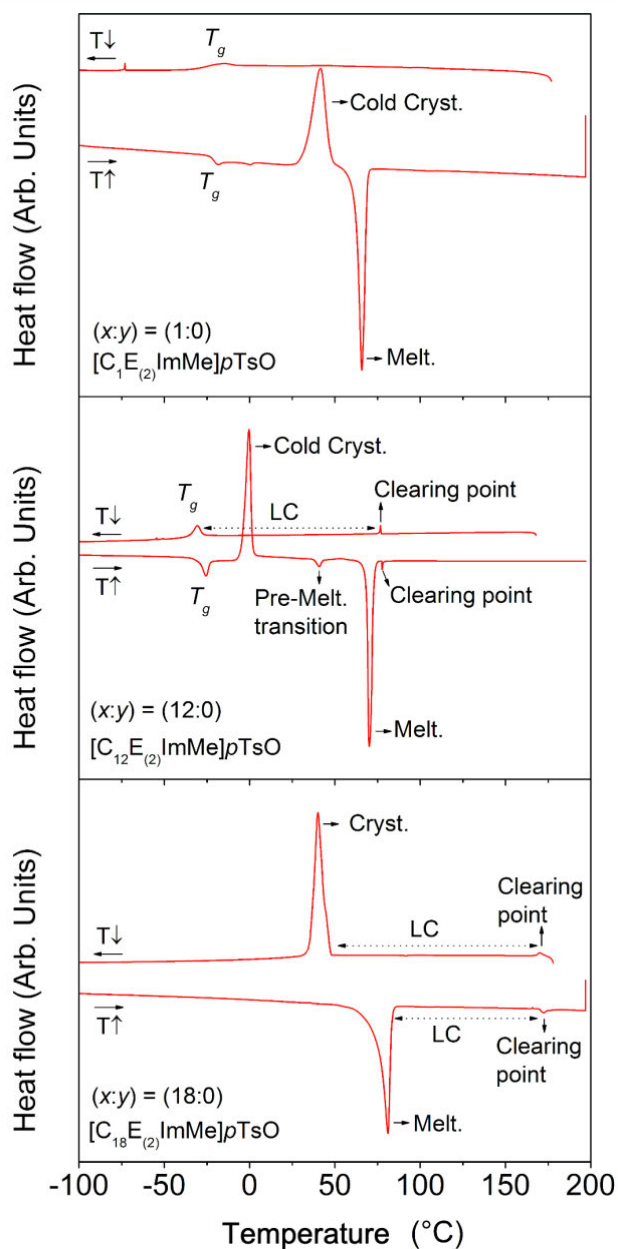
**Figure 1**: Differential scanning calorimetry (10 °C min⁻¹, Al Pan) traces of the cooling (T↓, upper curve) and second heating (T↑, lower curve) for (a) [C$_{1:0}$E$_{(2)}$ImMe]$p$TsO, (b) [C$_{12:0}$E$_{(2)}$ImMe]$p$TsO and (c) [C$_{18:0}$E$_{(2)}$ImMe]$p$TsO.

The DSC curves of [C$_{x:y}$E$_{(2)}$ImMe]pTsO are shown in Figure 1 for (x:y) = (1:0), (12:0), (18:0). With the exception of (x:y) = (18:0), the cooling ramps of the salts do not exhibit any crystallization peak. This is due to the marked tendency of [C$_{x:y}$E$_{(2)}$ImMe]pTsO to supercool and to form a glass before crystallizing.[22] For this reason, the heating ramps of [C$_{1:0}$E$_{(2)}$ImMe]pTsO and [C$_{12:0}$E$_{(2)}$ImMe]pTsO are characterized by a strong exothermic peak, as a result of their cold crystallization, followed by an intense endothermic melting peak. In contrast, [C$_{18:0}$E$_{(2)}$ImMe]pTsO does not exhibit any cold crystallization peak, proving that the crystallization was completed upon cooling. The temperatures and the enthalpy of transitions – $T_g$ for the glass transition, $T_m$ and $\Delta H_m$ for the melting point, and $T_c$ and $\Delta H_c$ for the crystallization (or cold crystallization when applicable) – are reported in Table 1. $T_m$ is found to slightly increase with $x$, the length of the alkyl tail. A similar observation was reported for a series of [C$_{x:y}$ImMe]X ILs.[22]

| Anion, [X] | (x:y) | $T_g$ (°C) | *Crystallization* | | *Melting* | | $LC \rightarrow I$ [d] | | $I \rightarrow LC$ [e] | |
| --- | --- | --- | --- | --- | --- | --- | --- | --- | --- | --- |
| | | | $T_c$ (°C) | $\Delta H_c$ (kJ mol⁻¹) | $T_m$ (°C) | $\Delta H_m$ (kJ mol⁻¹) | $T_{(LC)h}$ (°C) | $\Delta H_{(LC)h}$ (kJ mol⁻¹) | $T_{(LC)c}$ (°C) | $\Delta H_{(LC)c}$ (kJ mol⁻¹) |
| [$p$TsO] | (1:0) | -21 | 42 [b] | 26 | 66 | 27 | - | - | - | - |
| | (11:0) | -37 | 25 [b] | 31 | 46/58/65 [c] | 35 | - | - | - | - |
| | (11:1) | -41 | 32 [b] | 23 | 48 | 24 | - | - | - | - |

| | | | | | | | | | |
|---|---|---|---|---|---|---|---|---|---|
| | (12:0) | -29 | -0.3 [b] | 30 | 70 | 38 | 78 | 0.31 | 77 | 0.32 |
| | (18:0) | - | 40 [a] | 54 | 81 | 55 | 172 | 0.55 | 170 | 0.73 |
| | (18:1) | -43 | 24 [b] | 9 | 33 | 9 | 148 | 0.95 | 146 | 0.90 |
| [I] | (1:0) | -35 | - | - | - | - | - | - | - | - |
| | (11:0) | - | -16 [a] (-7 [b]) (35 [b]) | 18 (9) (6) | 84 | 45 | 123 | 0.42 | 122 | 0.41 |
| | (11:1) | - | -7 [b] | 27 | 45 | 35 | - | - | 34 | 0.17 |
| | (12:0) | - | 22 [a] | 39 | 63 | 45 | 164 | 0.64 | 163 | 0.70 |
| | (18:0) | - | 56/47 [a, c] | 62 | 81 | 63 | >200 | NA | >200 | NA |
| | (18:1) | -45 | 5 | 32 | 29/34 [c] | 37 | >200 | NA | >200 | NA |
| [BF$_4$] | (11:0) | -21 | -5 [a] (-2 [b]) (26 [b]) | 15 (15) (4) | 64 | 45 | 107 | 0.37 | 106 | 0.36 |
| | (12:0) | -19 | 11 [a] (4 [b]) | 18 (18) | 43 | 41 | 144 | 0.59 | 144 | 0.58 |

**Table 1**: Thermal data from DSC thermograms of IL(C)s synthesized in this work. The transition temperatures are measured from the peak maximum for the first order transitions (crystallization, melting and clearing point) and the transition midpoints for the glass transitions. [a] Regular crystallization during the cooling cycle, [b] cold crystallization during the heating cycle, [c] transition with multiple peaks, [d] liquid crystal to isotropic liquid transition (heating ramp), [e] isotropic liquid to liquid crystal transition (cooling ramp).

In the case of [C$_{12:0}$E$_{(2)}$ImMe]pTsO and [C$_{18:0}$E$_{(2)}$ImMe]pTsO, pre-melting and post-melting peaks of smaller enthalpy are also visible upon heating. The small pre-melting peak can be ascribed to a change of conformation of C$_{x:y}$ within the crystal lattice during heating.[64] As for the post-melting peak, it is attributed to a transition from a liquid crystal (LC) to an isotropic liquid, also referred to as the clearing point. This was confirmed by polarized optical microscopy (POM)

imaging, as well as small angle X-ray scattering (SAXS) measurements (see discussion hereafter). The reverse transition, *i.e.*, from the isotropic liquid to the LC, is also visible upon cooling. The temperature and the enthalpy of these transitions – $T_{(LC)h}$ and $\Delta H_{(LC)h}$ for the heating ramp and $T_{(LC)c}$ and $\Delta H_{(LC)c}$ for the cooling ramp – are also reported in Table 1. Clearly, $T_{(LC)h} \sim T_{(LC)c}$ and $\Delta H_{(LC)h} \sim \Delta H_{(LC)c}$ for the whole series. Unless otherwise specified, the rest of the discussion will be focused on the LC to isotropic liquid transition, i.e., $T_{(LC)h}$ and $\Delta H_{(LC)h}$ which will be noted $T_{LC}$ and $\Delta H_{LC}$.
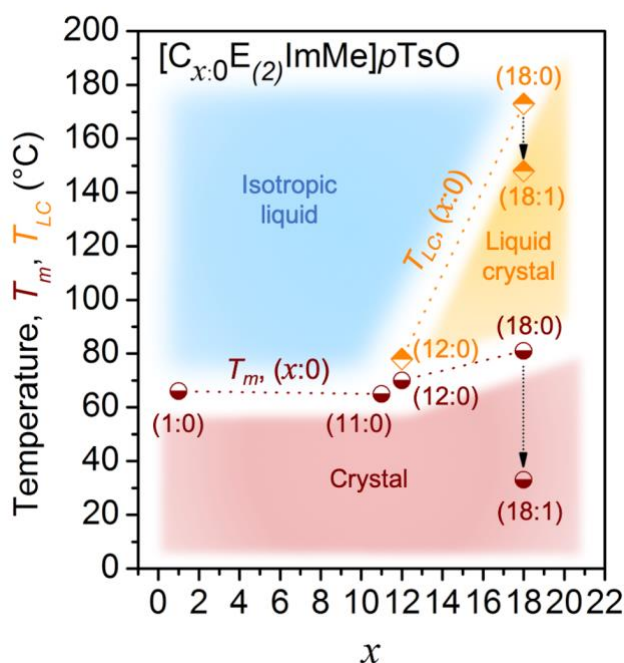


**Figure 2**: Schematic phase diagram for [C$_{x:0}$E$_{(2)}$ImMe]pTsO IL(C)s showing the melting temperature, $T_m$ (half-filled circle), and clearing temperature, $T_{LC}$ (half-filled diamond), as measured on the heating cycle of the corresponding DSC thermograms.

The clearing temperature, $T_{LC}$, shows a larger dependence on the alkyl chain length than the melting point. For instance, $T_{LC}$ varies from 78 °C for [C$_{12:0}$E$_{(2)}$ImMe]pTsO to 173 °C for

[$C_{18:0}E_{(2)}$ImMe]pTsO, while $T_m$ varies from 70 °C to 81 °C for the same compounds. This is well illustrated by plotting a basic phase diagram representing the variations of $T_m$ and $T_{LC}$ as a function of $x$ (Figure 2). One can note the expansion of the temperature range of the LC mesophase, $\Delta T_{C \to L}$ = $T_{LC}$ – $T_m$ (Eq. 1), from $\Delta T_{C \to L}$ = 8 °C for [$C_{12:0}E_{(2)}$ImMe]pTsO to $\Delta T_{C \to L}$ = 92 °C [$C_{18:0}E_{(2)}$ImMe]pTsO. This is mostly due to the increase of van der Waals interactions, as observed for classical [$C_{x:y}$ImMe]X ILs.[21-23] The whole series of [$C_{x:y}E_{(2)}$ImMe]X IL(C)s were analyzed by DSC (see Table 1 and Figures S48 to S61). It is noteworthy that all the salts are low melting point crystals, with $T_m$ < 100 °C. In that sense, they are consistent with the common definition of ionic liquids, *i.e.,* molten salts with melting point lower than 100 °C. Some of these IL(C)s exhibit convoluted thermograms with both regular crystallization upon cooling, and cold crystallization upon heating.

When considering the influence of the number of unsaturation into the lipidic tail (the *y* parameter), a significant decrease of the transition temperatures is observed for [$C_{18:1}E_{(2)}$ImMe]pTsO ($T_m$ = 33 °C; $T_{LC}$ = 148 °C), as compared to [$C_{18:0}E_{(2)}$ImMe]pTsO ($T_m$ = 81 °C; $T_{LC}$ = 173 °C). Data related to [$C_{18:1}E_{(2)}$ImMe]pTsO were added in the phase diagram of [$C_{x:0}E_{(2)}$ImMe]pTsO (Figure 2) to better illustrate the effect of the unsaturation. Both the melting and the clearing transitions are substantially impacted with a stronger effect on the melting temperature, $\Delta T_m$ = 48 °C, as compared to the clearing temperature, $\Delta T_{LC}$ = 25 °C. The introduction of a *cis* double bond results in a *"kinked"* tail structure, reducing the molecular packing efficiency both in the solid and the LC phases. Interestingly, the melting temperature of the resulting [$C_{18:1}E_{(2)}$ImMe]pTsO ($T_m$ = 33 °C) is very close to room temperature. Incorporation of an unsaturation into the alkyl chain of common *non-mesomorphic* [$C_{x:y}$ImMe]X ILs was first reported by Davis *et al.* as a strategy to obtain room temperature lipidic ILs.[44] Our results demonstrate that

this strategy is also relevant for the modulation of the clearing temperature of lipidic ILCs. More interestingly, the unsaturated ILC, [C$_{18:1}$E$_{(2)}$ImMe]pTsO, exhibits a wider mesophase, $\Delta T_{C \to L}$ = 115 °C, than its fully saturated counterparts, [C$_{18:0}$E$_{(2)}$ImMe]pTsO, $\Delta T_{C \to L}$ = 92 °C.

With the result obtained for [C$_{11:0}$E$_{(2)}$ImMe]X and [C$_{11:1}$E$_{(2)}$ImMe]X, it is possible to evaluate the influence of the unsaturation located at the end of the lipidic tail. Thus, the $T_m$ value decreases from 84 °C for [C$_{11:0}$E$_{(2)}$ImMe]I to 45 °C for [C$_{11:1}$E$_{(2)}$ImMe]I ($\Delta T_m$ = 39 °C). Furthermore, [C$_{11:1}$E$_{(2)}$ImMe]I exhibits an isotropic-to-LC transition upon cooling, for a temperature below its melting point, $T_{(LC)c}$ = 34 °C (Figure S56). The mesophase is not observed upon heating, *i.e.*, direct transition from crystal to isotropic liquid. This is characteristic of a metastable monotropic LC phase.[25] By opposition, all other ILCs investigated in this study are enantiotropic, *i.e.* they exhibit thermodynamically stable LC phases, both upon heating and cooling. Considering the influence of the terminal unsaturation on $T_{(LC)c}$, a significant decrease is observed, from 123 °C for [C$_{11:0}$E$_{(2)}$ImMe]I to 34 °C for [C$_{11:1}$E$_{(2)}$ImMe]I ($\Delta T_{(LC)c}$ = 89 °C). These results demonstrate that a subtle change in the conformation of the lipidic tail dramatically impact the phase transition of our bio-based ILCs.

Regarding the influence of the counter-anion, X, the melting temperature varies as follow: [pTsO] ~ [I] > [BF$_4$]. This result is in line with the general rule stating that mismatching in ion size, shape and symmetry results in lower melting points.[65] For X = I and X = BF$_4$, the melting point increases with the length of the fatty tail for even values of *x*. The case of [C$_{11:0}$E$_{(2)}$ImMe]X, where *x* = 11, reveals a pronounced odd-even effect. Indeed, for both X = I and X = BF$_4$, the melting point of [C$_{11:0}$E$_{(2)}$ImMe]X is 20 °C higher than for [C$_{12:0}$E$_{(2)}$ImMe]X. Regular *n*-alkanes with an odd number of carbon atoms are known for their lower abilities to pack into ordered periodic crystalline structures, and thus lower melting points, in comparison to *n*-alkanes with an

even number of carbon atoms.[66] Herein, coupling the lipidic tail to the imidazolium core results in the opposite trend, *i.e.* [C$_{x:0}$E$_{(2)}$ImMe]X ILs, where *x* is an odd number, exhibit higher packing ability and higher melting points. A similar trend was reported for ester-free [C$_{x:0}$ImMe]X ILs.[22]
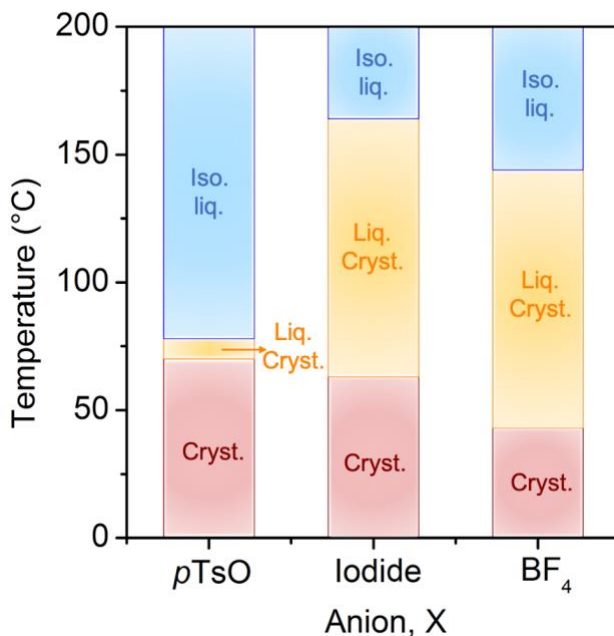


**Figure 3**: Temperature ranges for the crystal (red), liquid crystal (orange) and isotropic liquid (blue) phases for [C$_{12:0}$E$_{(2)}$ImMe]X where X = *p*TsO, I, and BF$_4$. The melting, $T_m$, and the clearing, $T_{LC}$, temperatures used in this diagram are obtained from the heating cycle of the corresponding DSC thermograms.

It is worth noting that $T_{LC}$ values vary in a different order than $T_m$ values. For $T_{LC}$, the counter-anion effect is as follow: [I] > [BF$_4$] > [*p*TsO]. Figure 3 shows the temperature windows of the different phases observed for [C$_{12:0}$E$_{(2)}$ImMe]X (X = I, BF$_4$ and *p*TsO). The temperature span of the mesophase, $\Delta T_{C \to L}$ (*cf.* Eq. 1), is the smallest for X = *p*TsO ($\Delta T_{C \to L}$ = 8°C). For both X = I and X = BF$_4$, larger mesophases are observed, with $\Delta T_{C \to L}$ ~ 40 °C. For a given cation, $\Delta T_{C \to L}$ is

generally dependent on the ability of the anion to build an extended hydrogen bonding network within the ionic sublayers.[25] In particular, it has been observed that halide anions (Cl$^-$ and Br$^-$) develop strong hydrogen bonding networks with the acidic hydrogen atom in C2-position of the imidazolium ring. Halogen containing anions, such as $BF_4^-$, can develop similar interactions, but to a less extent, due to the lower charge density on each halide (*i.e.*, F).[65] For these reasons, the mesophase stability, $\Delta T_{C \rightarrow L}$, decreases in the order [Cl] ~ [Br] > [BF4]. To our knowledge, there are no data available for [$C_{x:0}$ImMe]X ILCs where X = I. Due to the lower overall anion charge density of I$^-$, $\Delta T_{C \rightarrow L}$ is expected to decrease, as compared to the chloride and bromide counterparts. Hence, it is not surprising that [$C_{12:0}E_{(2)}$ImMe]I and [$C_{12:0}E_{(2)}$ImMe]BF4 exhibit a similar mesophase stability ($\Delta T_{C \rightarrow L}$ ~ 40 °C). In the case of [$C_{12:0}E_{(2)}$ImMe]*p*TsO, the very small temperature window of the mesophase ($\Delta T_{C \rightarrow L}$ ~ 8 °C) is probably a consequence of the bulkiness of the *p*TsO anion, combined with the poor ability of the sulfonate head-group to develop oriented hydrogen bonds with the acidic proton of the imidazolium core.

In order to gain more insight into the role played by the ester linkage, the DSC data collected for [$C_{x:y}E_{(2)}$ImMe]X were compared with the background literature for [$C_{x:y}$ImMe]X. In particular, the thermal properties of [$C_{x:0}$ImMe]BF4, for *x* varying from 1 to 18, were extensively studied by Seddon et *al*.[22] In the case of [$C_{12:0}E_{(2)}$ImMe]BF4 ($T_m$ = 43 °C and $T_{LC}$ = 144 °C), both melting and clearing points are in-between those reported for [$C_{14:0}$ImMe]BF4 ($T_m$ = 42 °C and $T_{LC}$ = 129 °C) and [$C_{15:0}$ImMe]BF4 ($T_m$ = 55 °C and $T_{LC}$ = 148 °C).

By taking a closer look, [$C_{12:0}E_{(2)}$ImMe]BF4 and [$C_{14:0}$ImMe]BF4, whose total number of CH2 units into the lipidic tail is identical, exhibit the same melting temperature. However, the clearing point of [$C_{12:0}E_{(2)}$ImMe]BF4 is much closer to that of [$C_{15:0}$ImMe]BF4. Furthermore, the mesophase of [$C_{12:0}E_{(2)}$ImMe]BF4, $\Delta T_{C \rightarrow L}$ ~101 °C, is broader than that of [$C_{15:0}$ImMe]BF4, $\Delta T_{C \rightarrow L}$

~ 93 °C, and [C$_{14:0}$ImMe]BF$_4$, $\Delta T_{C \to L}$ ~ 87 °C. These results strongly suggest that the ester moiety of [C$_{x:y}E_{(2)}$ImMe]X ILs is involved in the stabilization of the mesophase, very likely through the polarizability of the $\pi$ electrons of the carbonyl group. Tseng *et al.* came to the same conclusion for [C$_{x:y}E_{(1)}$ImMe]X ILCs.[57] The authors observed that [C$_{x:y}E_{(1)}$ImMe]BF$_4$ exhibit wider mesophase than their [C$_{x:y}$ImMe]BF$_4$ analogs. For [C$_{12:0}E_{(1)}$ImMe]BF$_4$, they measured $T_m$ = 52 °C and $T_{LC}$ = 164 °C, i.e. $\Delta T_{C \to L}$ ~ 112 °C. By comparison, $T_m$ = 43 °C and $T_{LC}$ = 144 °C, *i.e.* $\Delta T_{C \to L}$ ~101 °C, for [C$_{12:0}E_{(2)}$ImMe]BF$_4$. Thus, it appears that decreasing the size of the spacer in-between the imidazolium core and the ester moiety results in a slight increase of $T_m$ and $\Delta T_{C \to L}$.

*POM of [C$_{x:y}E_{(2)}$ImMe]X IL(C)s*

As indicated earlier, the thermotropic liquid crystalline properties of [C$_{x:y}E_{(2)}$ImMe]X were confirmed by using polarized optical microscopy (POM), equipped with a heating platform. By slowly cooling the samples from the isotropic liquid (5 °C min$^{-1}$), micrograph textures, suggesting a layered smectic A (SmA) mesophase, appear for all the samples that exhibited a post-melting peak of small enthalpy in their DSC thermogram. Figure 4a displays a typical micrograph obtained for [C$_{12:0}E_{(2)}$ImMe]$p$TsO at 75 °C ($T_m$ = 70 °C, $T_{LC}$ = 78 °C from DSC measurements). In that case, a fan-like texture with striking birefringence, characteristic of a SmA mesophase, is observed. Figure 4b illustrates the micrograph for [C$_{18:0}E_{(2)}$ImMe]$p$TsO ($T_m$ = 81 °C, $T_{LC}$ = 173 °C) recorded at T = 100 °C. In that case, dichroism is no longer visible due to the homeotropic alignment of the liquid crystal domain, *i.e.*, the optical axis is oriented perpendicularly to the microscope slides. When the film is deformed by shearing the slides, an oily-streak texture is observed (Figure 4b), another distinctive signature of the SmA mesophase.
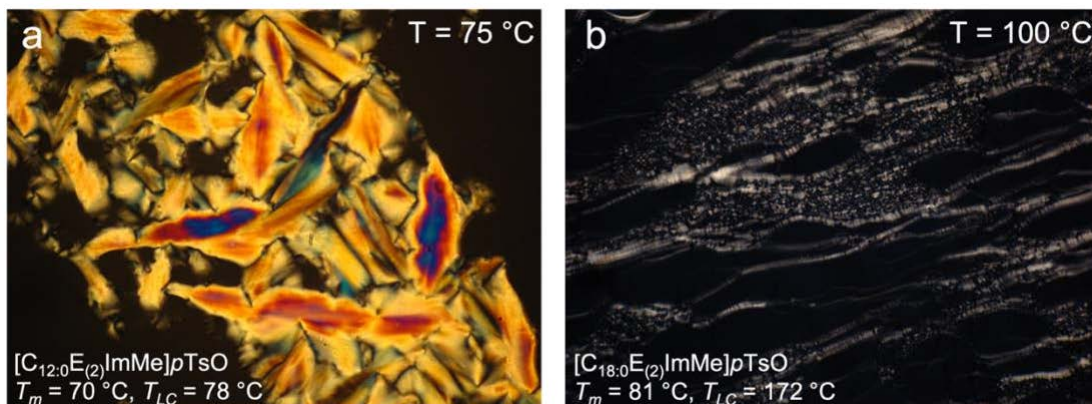
**Figure 4**: Optical microscopic texture of the mesophase (Smectic A) observed under crossed polarizers at elevated temperature for (a) [$C_{12:0}E_{(2)}$ImMe]$p$TsO, T = 75 °C (fan-like texture with birefringence) and (b) [$C_{18:0}E_{(2)}$ImMe]$p$TsO, T = 100 °C (oily streak texture).

Fan-like textures and/or oily-streak textures, characteristic of a SmA mesophase, were observed for all the [$C_{x:y}E_{(2)}$ImMe]X salts showing a clearing transition on their DSC thermogram (see corresponding POM micrographs in Figures S62 to S68). In the case of [$C_{18:0}E_{(2)}$ImMe]I and [$C_{18:1}E_{(2)}$ImMe]I (Figures S66 and S67), for which clearing transitions are not apparent in DSC, presumably because they are beyond the maximum temperature of the heating cycle, the same oily streak texture was observed by shearing the sample after heating above their melting point. This is consistent with a mesomorphic behavior over the temperature range explored in this study.

Overall, these results suggest that [$C_{x:0}E_{(2)}$ImMe]X exhibit SmA mesophase for $x$ values as low as $x = 12$ in the case of X = $p$TsO (no mesophase for $x = 11$), and $x = 11$ in the case of X = I$^-$ and BF$_4^-$ (the cases $x \leq 10$ were not investigated). For [$C_{x:0}$ImMe]BF$_4$, Seddon *et al.* observed a SmA mesophase for $x$ values as low as $x = 12$ (no mesophase for $x \leq 11$). Similarly, for

[C$_{x:0}$E$_{(1)}$ImMe]BF$_4$, Tseng *et al.* reported a SmA mesophase for *x* values as low as *x* = 12 (the cases *x* ≤ 11 were not investigated).

*SAXS of [C$_{x:y}$E$_{(2)}$ImMe]X IL(C)s*

SAXS data were collected for all the ILCs as a function of temperature, in complement to DSC and POM analyses. The diffraction patterns obtained for [C$_{18:0}$E$_{(2)}$ImMe]$p$TsO ($T_m$ = 81 °C, $T_{LC}$ = 173 °C ) at (*i*) T = 30 °C (crystal), (*i*) T = 120 °C (mesophase) and (*iii*) T = 190 °C (isotropic liquid) are displayed in Figure 5. The diffractogram obtained at T = 30 °C (crystal) shows a principal scattering peak for $q^*$ = 0.19 Å$^{-1}$ and higher order peaks, $2q^*$, $3q^*$ and $4q^*$, that are consistent with a lamellar ordering. The layer spacing in the crystalline phase, $d_{Cr}$ = 35.4 Å, is calculated using the Bragg's law, $d = 2\pi/q^*$ (Eq. 2). A large number of peaks, corresponding to repeating distance within the layers (*e.g.*, cation-cation, anion-anion), are found in the large-*q* region. They are consistent with the high ordering of the crystalline phase.[67] Upon heating up to T = 120 °C (mesophase), the principal scattering peak, $q^*$, and the higher order peaks, $2q^*$ and $3q^*$, persist, meaning the lamellar ordering is maintained above the melting point ($T_m$ = 81 °C, from DSC measurement). This correlates with the observation of the characteristic texture of a lamellar SmA mesophase by POM. The calculation of the layer spacing in the mesophase gives $d_{SmA}$ = 34.9 Å (*cf.* Eq. 2). Peaks in the large-*q* region are lost in this case, indicating a decrease in positional ordering within the layer plane.  Instead, a very broad single peak is observed, which is characteristic of the fluid-like alkyl chain region.[68] By further increasing the temperature to T = 190 °C (liquid), the principal scattering peak broadens and the higher order peaks disappear. The resulting single broad reflection is characteristic of a disordered structure, thus confirming that the

system behaves as an isotropic liquid beyond the clearing point, $T_{LC}$ = 173 °C, as determined by DSC.
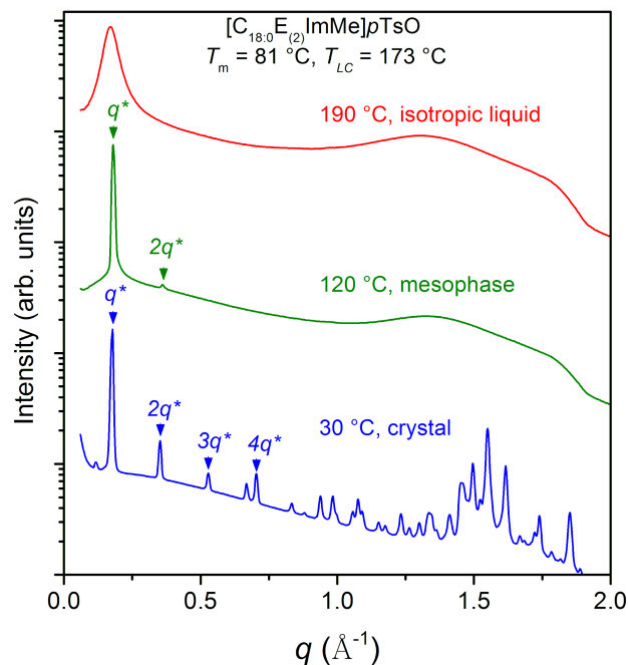


**Figure 5**: Small angle X-ray scattering patterns for [$C_{18:0}E_{(2)}$ImMe]$p$TsO ($T_m$ = 81°C, $T_{LC}$ = 173 °C) in the crystal (30 °C), SmA (120°C) and isotropic (190°C) phases. The patterns were acquired during a heating cycle. In the crystal phase and the mesophase the principal scattering peak ($q*$) and the higher order reflection peaks (multiple of $q*$) are indicated by pointed down triangles. Curves have been shifted vertically for clarity.

When comparing the $d$-spacing, $d_{Cr}$ and $d_{SmA}$, to the fully extended length of the cation ($L$, calculated by using Chem3D® software, see Figure S69), the following order is observed: $L < d_{Cr}$, $d_{SmA} < 2L$. This suggests an arrangement into a bilayer structure, with partial interdigitation of the alkyl chains, possibly with a tilt angle with respect to the layer normal, as schematically depicted in Figure 6. The resulting bimolecular layering in the mesophase is often referred to as Smectic

A2, SmA2.[67] A similar arrangement was reported for both [C$_{x:0}$ImMe]X[67] and [C$_{x:0}$E$_{(I)}$ImMe]X[57] ILCs in the crystal phase and the mesophase.
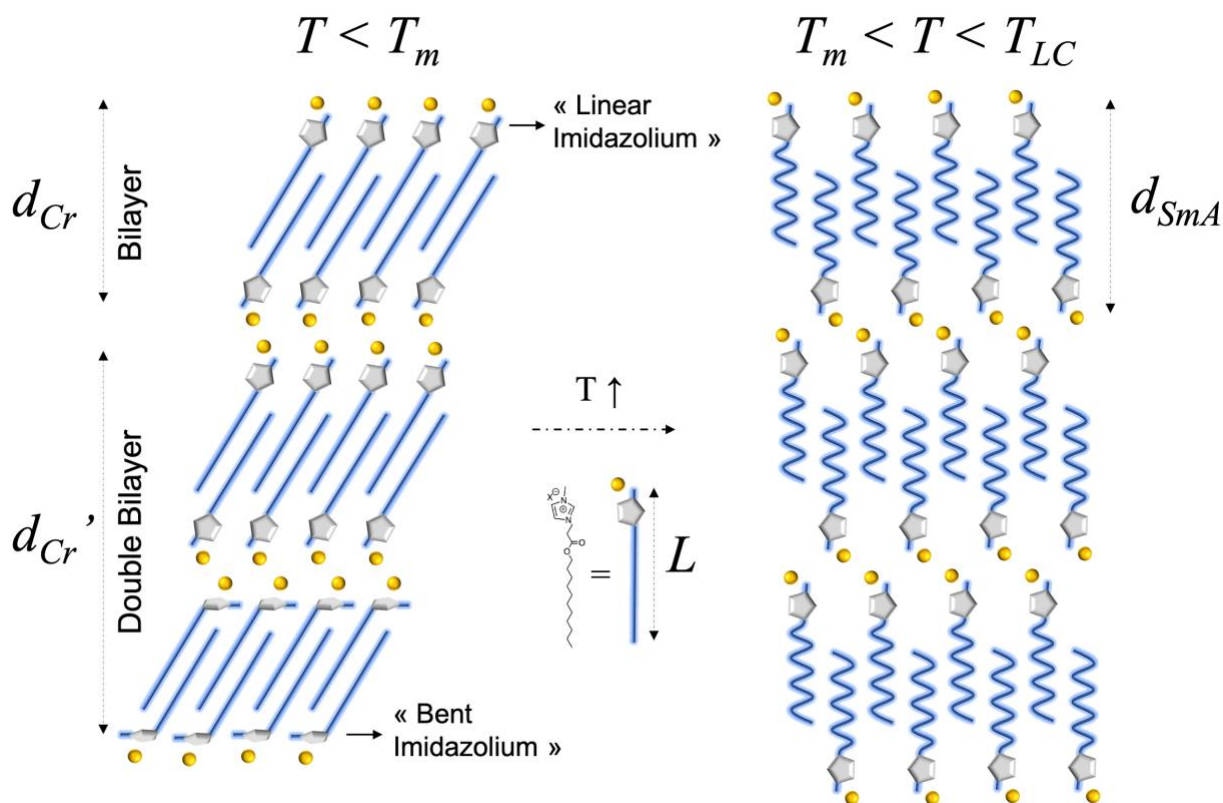


**Figure 6**: Schematic representation of the bilayer arrangement with interdigitation of the alkyl chains, in the crystalline phase and in the mesophase

In the crystal phase, a much less intense peak is observed in the small-$q$ region ($q$ = 1.67 Å$^{-1}$, $d_{Cr}'$ = 52.9 Å), which does not fit the regular repeating unit of the lamellar structure. This particular feature was also observed for conventional ester-free [C$_{x:0}$ImMe]X ILs by Bradley *et al.*,[67] and was attributed to a different layer spacing, possibly a double bilayer, arising from differing conformations of the imidazolium core in alternating layers. Indeed, as depicted in Figure 6, the

imidazolium ring can exhibit a linear or a bent conformation, as compared to the alkyl tail. Both conformations were reported to coexist in single crystals of $[C_{x:0}ImMe]Cl$.[69]

Surprisingly, for $[C_{18:0}E_{(2)}ImMe]pTsO$, $d_{Cr} \sim d_{SmA}$, unlike conventional $[C_{x:0}ImMe]X$ (with X = halide or $BF_4^-$) for which the $d$-spacing usually increases from the crystal phase to the mesophase. The SAXS diffractograms of $[C_{12:0}E_{(2)}ImMe]pTsO$ and $[C_{18:1}E_{(2)}ImMe]pTsO$, (Figures S70 and S71) suggest the same bilayer arrangement both in the crystal phase and in the mesophase. The values of $d_{Cr}$ and $d_{SmA}$ are reported in Table 2. As expected, the $d$-spacing decreases with $x$. It is worth noting that the introduction of an unsaturation has very little impact on $d_{SmA}$.

The diffractograms of $[C_{x:y}E_{(2)}ImMe]I$ were also collected (see Figures S72 to S75 and Table 2 for $d$-spacing values). For $(x:y) = (12:0)$, $(18:0)$ and $(18:1)$, the same lower and upper bound, $i.e.$ $L < d_{Cr}, d_{SmA} < 2L$, are observed, suggesting a similar bilayer arrangement into the $SmA_2$ mesophase. However for $(x:y) = (11:0)$, $d_{Cr} < L$ and $L < d_{SmA} < 2L$, indicating some peculiarities in the crystalline phase for this alkyl chain length, although the mesophase is similar to the other ILCs of this study. This is further illustrated by the very large expansion of $[C_{11:0}E_{(2)}ImMe]I$, $d_{SmA}$ - $d_{Cr} = 13$ Å, during the crystal-to-mesophase transition, as compared to $d_{SmA}$ - $d_{Cr} \sim 4$ Å for the other $[C_{x:y}E_{(2)}ImMe]I$ ILCs. These results suggest that $[C_{11:0}E_{(2)}ImMe]I$ adopts a bilayer arrangement ($SmA_2$) in the crystalline phase, with a much higher molecular packing density than the other ILs. This observation is in line with results obtained by DSC, where a pronounced odd-even effect was evidenced for $[C_{11:0}E_{(2)}ImMe]I$. Indeed, $[C_{11:0}E_{(2)}ImMe]I$ is characterized by a higher melting point than $[C_{12:0}E_{(2)}ImMe]I$, most probably due to a higher packing ability in the crystalline phase. This is further supported by single-crystal X-ray analysis presented hereafter.

Figures S76 and S77 represent the diffractograms obtained for $[C_{x:y}E_{(2)}ImMe]BF_4$ with $(x:y)$ = (12:0) and (11:0). The $d$-spacing values are reported in Table 2. Remarkably, $[C_{11:0}E_{(2)}ImMe]BF_4$

exhibits the same peculiarities as [C$_{11:0}$E$_{(2)}$ImMe]I, *i.e.*, $d_{Cr} < L$ and $L < d_{SmA} < 2L$, again supporting

the hypothesis that the C$_{11:0}$ alkyl tail promotes a high molecular packing density.

| Anion, [X] | (x:y) | $T_m$ (°C) | $T_{LC}$ (°C) | $L$ (Å) [a] | Crystal | | SmA$_2$ | |
|---|---|---|---|---|---|---|---|---|
| | | | | | $d_{Cr}$ (Å) | $T_{Cr}$ (°C) | $d_{SmA}$ (Å) | $T_{SmA}$ (°C) |
| [pTsO] | (12:0) | 70 | 78 | 22.1 | 30.0 | 25 | 29.5 | 74 |
| | (18:0) | 81 | 172 | 29.6 | 35.4 | 30 | 34.9 | 120 |
| | (18:1) | 33 | 148 | 26.1 | NA[b] | NA[b] | 35.7 | 40 |
| [I] | (11:0) | 84 | 123 | 21.0 | 17.1 | 25 | 30.1 | 100 |
| | (12:0) | 63 | 164 | 22.1 | 28.4 | 56 | 32.0 | 110 |
| | (18:0) | 81 | >200 | 29.6 | 36.1 | 75 | 38.7 | 120 |
| | (18:1) | 29/34 | >200 | 26.1 | NA[b] | NA[b] | 37.8 | 100 |
| [BF$_4$] | (11:0) | 64 | 107 | 21.0 | 17.4 | 25 | 30.8 | 100 |
| | (12:0) | 43 | 144 | 22.1 | 34.8 | 25 | 32.7 | 100 |

**Table 2**: Layer spacing of the ILCs determined by small angle X-ray scattering in the crystalline

phase, $d_{Cr}$, and in the SmA2 phase, $d_{SmA}$. The values are based on the position of the principal

scattering peak, $q^*$, of the SAXS pattern acquired for the measuring temperatures $T_{Cr}$ and $T_{SmA}$,

respectively. [a] $L$ is the fully extended length of the cation calculated by using Chem3D® software.

[b] For (x:y) = (18:1), the salts behaves as room temperature (RT) ILs ($T_m$ very close to RT) and it

was not possible to study the crystalline phase by SAXS.

*Single crystal X-ray analysis of [C$_{x:y}$E$_{(2)}$ImMe]X IL(C)s*

In order to fully elucidate the structure suggested by SAXS experiments, single crystal X-ray

analysis was conducted for ILCs providing crystals of sufficient quality. Well-formed single

crystals of [C$_{18:0}$E$_{(2)}$ImMe]pTsO, [C$_{11:0}$E$_{(2)}$ImMe]I, as well as [C$_{11:0}$E$_{(2)}$ImMe]BF$_4$, were grown

from cold methanol solutions. Details of the crystallographic data of these three compounds are

given in Table S2. Attempts to crystallize the other salts, *i.e.* of lower melting point, were unsuccessful.
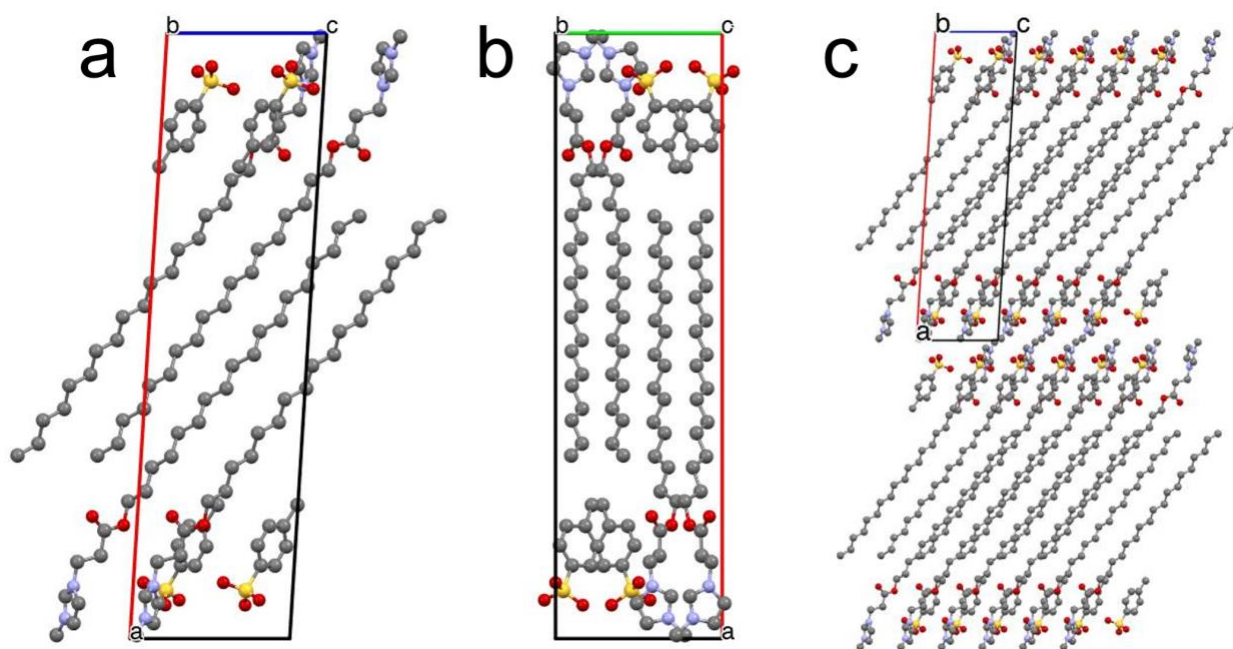


**Figure 7**: Crystal structure of [C$_{18:0}$E$_{(2)}$ImMe]$p$TsO at 25 °C. (a) unit cell along *b* axis, (b) unit cell along *c* axis, (c) overall bilayer structure showing the interdigitation and the tilted alkyl chains along *b* axis.

The data obtained for [C$_{18:0}$E$_{(2)}$ImMe]$p$TsO confirm that the crystal structure consists of sheets of imidazolium rings and tosylate anions, separated by interdigitated alkyl chains. The unit cell is represented in Figures 7a and 7b (along *b* and *a* axis, respectively), while Figure 7c depicts the interdigitated pattern (along *b* axis). The layer distance is equal to 35.5 Å (see Figure S78), in very good accordance with the *d*-spacing measured by SAXS ($d_{Cr} = 35.4$ Å). Remarkably, the imidazole rings are almost perpendicular to the layer plan. Indeed, the plan formed by the imidazolium ring intersects the layer plan with an angle of about 87° (Figure S79). As suggested by SAXS, the alkyl

chains are tilted as compared to the layer plan. They form an angle of about 39° with the normal layer (see Figure S78). When considering the tosylate anion, the sulfonate head group is oriented toward the imidazolium head group, while the aromatic ring points towards the interdigitated alkyl chains. The very short distance between two consecutive bilayers makes it possible for the sulfonate head group to develop O···H−C interactions, *i.e.,* weak hydrogen bonds, with neighboring imidazolium head groups located within the same bilayer, and in the in-front bilayer (Figure S80). Similarly, the oxygen atoms of the sulfonate head group develop O···H−C interactions with the hydrogens in alpha position of the carbonyl group of one neighboring cation (see Figure S81). To our knowledge, this is the first time the crystal structure of a 1-long alkyl chain-3-methylimidazolium salt featuring a tosylate counter-anion is reported. The orientation of the imidazolium cation is very similar to that of other $[C_{18:0}ImMe]X$ ILs and ILCs. For instance, hexafluorophophate[23] and bis(fluorosulfonyl)imide[70] salts of $[C_{18:0}ImMe]$ exhibit a comparable interdigitated structure with imidazole ring perpendicular to the layer plan.
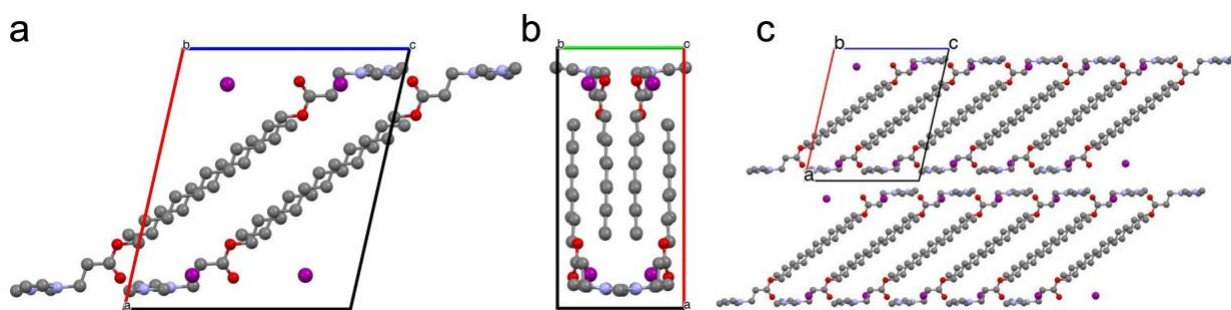


**Figure 8**: Crystal structure of $[C_{11:0}E_{(2)}ImMe]I$ at 25 °C. (a) unit cell along *b* axis, (b) unit cell along *c* axis, (c) overall bilayer structure showing the interdigitation and the tilted alkyl chains along *b* axis.

The crystal structure of $[C_{11:0}E_{(2)}ImMe]I$ is presented in Figure 8. Similarly to $[C_{18:0}E_{(2)}ImMe]pTsO$, it consists of sheets of imidazolium rings and iodide anions, separated by interdigitated alkyl chains. However, the orientation of the cation is totally different. Indeed, the imidazolium rings are parallel to the layer plan. They form a border between two consecutive bilayers, suggesting that strong $\pi$-$\pi$ interactions are developed between those layers. In this configuration, the imidazolium rings occupy a minimal space along the normal layer. Furthermore, the alkyl chain are tilted with an angle of about 52° (Figure S82), as compared to the normal layer, against 37° for the alkyl chains of $[C_{18:0}E_{(2)}ImMe]pTsO$.

These features result in a strong minimization of the layer distance, $d_{Cr}$ = 17.2 Å (see Figure S82), which is in very good accordance with the estimation of $d_{Cr}$ by SAXS measurement ($d_{Cr}$ = 17.1 Å). It is also worth noting that the oxygen atom of the carbonyl group is arranged nearly in the plan of the imidazolium ring. In this configuration, the carbonyl group can develop O···H−C interactions with neighboring imidazolium head groups located within the same bilayer, and in the in-front bilayer (see Figure S83). It is thus actively contributing to the stabilization of the whole crystalline structure. The iodide anion is located within the bilayer, 1 Å below the plan formed by the imidazolium ring and in the center of the triangle formed by the imidazolium rings of three cations. It develops weak interactions with one hydrogen per surrounding cation (see Figure S84). Interestingly, Tseng *et al.* reported that $[C_{16:0}E_{(1)}ImMe]Br$ exhibits a crystal structure with the same parallel arrangement of the imidazolium rings in the layer plan.[57] In that case, however, the oxygen atom of the carbonyl group points towards the inner part of the bilayer and does not contribute to the stabilization of the ionic layer.

The crystal structure of $[C_{11:0}E_{(2)}ImMe]BF_4$ (Figures S85 and S86) is very similar to that of $[C_{11:0}E_{(2)}ImMe]I$, with a layer distance of 17.0 Å (again in good agreement with the result obtained

by SAXS, $d_{Cr} = 17.4$ Å), and interdigitated alkyl chains forming an angle of 53° with the normal layer.

Although these data do not permit to draw unequivocal conclusion regarding which parameters (*e.g.*, *x* and X) is responsible for the parallel or orthogonal orientation of the imidazolium head groups relatively to the layer plan, they demonstrate that this new family of IL(C)s exhibits original molecular ordering. They could be useful in applications including anisotropic conductive materials or molecular templating. The most original feature is the contribution of the carbonyl group of the ester moiety to the stabilization of the ionic layer, through the development of specific interactions in the plan formed by imidazolium head groups.

**Conclusions**

A library of 1-alkyl-3-methylimidazolium-type IL(C)s was designed, following a strategy based on three (for X = I⁻ or *p*TsO⁻) or four (for X = BF₄⁻) consecutive reaction steps starting from biosourced fatty alcohols. The synthesis involves the Michael addition of imidazole onto the acrylic-functionalized fatty alcohols, followed by the quaternization of the imidazole ring using different alkylating agents. This strategy introduces an ester moiety within the *N*-alkyl substituent, and possibly a C=C double bond when unsaturated fatty alcohols are employed.

The thermal and structural properties of these ILs were thoroughly investigated by NMR, DSC, TGA, POM and SAXS. Their higher susceptibility to thermal degradation, as compared to ester-free 1-alkyl-3-methylimidazolium ILs, was evidenced by TGA analysis, and attributed to the presence of the cleavable ester function. A higher sensitivity to biodegradation is anticipated on the basis of previous results reported for other ester-containing 1-alkyl-3-methylimidazolium ILs.

Most of these newly synthesized ILs also exhibit liquid crystalline properties, as established by DSC, POM, single crystal X-Ray and SAXS analyses. The temperature window of their mesophase was found to dramatically depend on the size of the alkyl substituent, the anion and on the degree of unsaturation. Characterization by POM and SAXS revealed that these ILCs self-organize into a smectic A ordering, which is characterized by a bilayer arrangement with partial interdigitation of the alkyl chains and a tilt angle with respect to the normal layer. Analysis of the crystal structure gave further insight, showing that self-assembled structures involve sheets of imidazolium rings and anions, separated by interdigitated alkyl chains. Interestingly, the orientation of the imidazolium head group can be either parallel or orthogonal to the layer plan, depending both on the size of the alkyl chain and the nature of the anion. Moreover, the ester moiety plays a key role in the crystal structure by developing $O \cdots H-C$ interactions both within bilayers and in-between neighboring bilayers.

By combining the use of bio-sourced precursors (fatty alcohols) with nearly quantitative synthetic steps (Michael addition), this work provides an efficient synthesis of new ILs and ILCs with easily tunable properties and a reduced environmental impact. The ester moiety and the potential unsaturation provide a versatile means to manipulate the thermal and structural properties of these IL(C)s. The latter could be used to program their degradation after disposal (cleavage of the ester bond) or for further valorization after synthesis (post-functionalization and/or polymerization using an unsaturated polymerizable moiety, for instance). The multistep synthesis of these new ester-containing IL(C)s still suffers from the use of toxic solvents (*e.g.*, chloroform) and reagents (*e.g.*, acryloyl chloride, methyl iodide). In this regard, we are currently investigating a new synthetic pathway providing analogous structures (*i.e.*, $[C_{x:y}E_{(2)}ImMe]X$) in one-step with halogen-free reagents and solvents.

**Associated content**

The supporting information is available free of charge

Experimental details and characterization data (PDF): synthetic procedures, $^1$H and $^{13}$C NMR spectra and analysis, HRMS spectra and analysis, TGA and DSC thermograms, polarized optical microscopy, calculation of the fully extended length of the cation, temperature dependent SAXS patterns, single crystal X-ray analysis.

Crystallographic Information Files (CIF): [C$_{18:0}$$E_{(2)}$ImMe]$p$TsO, [C$_{11:0}$$E_{(2)}$ImMe]I, [C$_{11:0}$$E_{(2)}$ImMe]BF$_4$.

**Authors information**

*Corresponding authors*

Thomas Vidil: thomas.vidil@enscbp.fr

Daniel Taton: daniel.taton@enscbp.fr

Henri Cramail: henri.cramail@enscbp.fr

**Notes**

The authors declare no competing financial interest

**References**

1.      Walden, P., Molecular weights and electrical conductivity of several fused salts. *Bulletin de l'Académie Impériale des Sciences de St.-Pétersbourg* **1914**, 405-422, DOI: NA
2.      Singh, S. K.; Savoy, A. W., Ionic liquids synthesis and applications: An overview. *Journal of Molecular Liquids* **2020,** *297*, 112038, DOI: 10.1016/j.molliq.2019.112038
3.      Hallett, J. P.; Welton, T., Room-Temperature Ionic Liquids: Solvents for Synthesis and Catalysis. 2. *Chemical Reviews* **2011,** *111* (5), 3508-3576, DOI: 10.1021/cr1003248
4.      Welton, T., Room-temperature ionic liquids. Solvents for synthesis and catalysis. *Chemical Reviews* **1999,** *99* (8), 2071-2083, DOI: 10.1021/cr980032t
5.      Ventura, S. P. M.; Silva, F. A. E.; Quental, M. V.; Mondal, D.; Freire, M. G.; Coutinho, J. A. P., Ionic-Liquid-Mediated Extraction and Separation Processes for Bioactive Compounds: Past, Present, and Future Trends. *Chemical Reviews* **2017,** *117* (10), 6984-7052, DOI: 10.1021/acs.chemrev.6b00550
6.      Villa, R.; Alvarez, E.; Porcar, R.; Garcia-Verdugo, E.; Luis, S. V.; Lozano, P., Ionic liquids as an enabling tool to integrate reaction and separation processes. *Green Chemistry* **2019,** *21* (24), 6527-6544, DOI: 10.1039/c9gc02553g
7.      Ayati, A.; Ranjbari, S.; Tanhaei, B.; Sillanpaa, M., Ionic liquid-modified composites for the adsorptive removal of emerging water contaminants: A review. *Journal of Molecular Liquids* **2019,** *275*, 71-83, DOI: 10.1016/j.molliq.2018.11.016
8.      Micheau, C.; Arrachart, G.; Turgis, R.; Lejeune, M.; Draye, M.; Michel, S.; Legeai, S.; Pellet-Rostaing, S., Ionic Liquids as Extraction Media in a Two-Step Eco-Friendly Process for Selective Tantalum Recovery. *Acs Sustainable Chemistry & Engineering* **2020,** *8* (4), 1954-1963, DOI: 10.1021/acssuschemeng.9b06414
9.      Boyd, R.; Jin, L.; Nockemann, P.; Robertson, P. K. J.; Stella, L.; Ruhela, R.; Seddon, K. R.; Gunaratne, H. Q. N., Ionic liquids tethered to a preorganised 1,2-diamide motif for extraction of lanthanides. *Green Chemistry* **2019,** *21* (10), 2583-2588, DOI: 10.1039/c9gc00089e
10.     Ullah, Z.; Khan, A. S.; Muhammad, N.; Ullah, R.; Alqahtani, A. S.; Shah, S. N.; Ben Ghanem, O.; Bustam, M. A.; Man, Z., A review on ionic liquids as perspective catalysts in transesterification of different feedstock oil into biodiesel. *Journal of Molecular Liquids* **2018,** *266*, 673-686, DOI: 10.1016/j.molliq.2018.06.024

11.      Vekariya, R. L., A review of ionic liquids: Applications towards catalytic organic transformations. *Journal of Molecular Liquids* **2017,** *227*, 44-60, DOI: 10.1016/j.molliq.2016.11.123

12.      Salanne, M., Ionic Liquids for Supercapacitor Applications. *Topics in Current Chemistry* **2017,** *375* (3), 63, DOI: 10.1007/s41061-017-0150-7

13.      Forsyth, M.; Porcarelli, L.; Wang, X. E.; Goujon, N.; Mecerreyes, D., Innovative Electrolytes Based on Ionic Liquids and Polymers for Next-Generation Solid -State Batteries. *Accounts of Chemical Research* **2019,** *52* (3), 686-694, 10.1021/acs.accounts.8b00566

14.      Egorova, K. S.; Gordeev, E. G.; Ananikov, V. P., Biological Activity of Ionic Liquids and Their Application in Pharmaceutics and Medicine. *Chemical Reviews* **2017,** *117* (10), 7132-7189, DOI: 10.1021/acs.chemrev.6b00562

15.      Capela, E. V.; Santiago, A. E.; Rufino, A.; Tavares, A. P. M.; Pereira, M. M.; Mohamadou, A.; Aires-Barros, M. R.; Coutinho, J. A. P.; Azevedo, A. M.; Freire, M. G., Sustainable strategies based on glycine-betaine analogue ionic liquids for the recovery of monoclonal antibodies from cell culture supernatants. *Green Chemistry* **2019,** *21* (20), 5671-5682, DOI: 10.1039/c9gc02733e

16.      Watanabe, M.; Thomas, M. L.; Zhang, S. G.; Ueno, K.; Yasuda, T.; Dokko, K., Application of Ionic Liquids to Energy Storage and Conversion Materials and Devices. *Chemical Reviews* **2017,** *117* (10), 7190-7239, DOI: 10.1021/acs.chemrev.6b00504

17.      Yang, Q. W.; Zhang, Z. Q.; Sun, X. G.; Hu, Y. S.; Xing, H. B.; Dai, S., Ionic liquids and derived materials for lithium and sodium batteries. *Chemical Society Reviews* **2018,** *47* (6), 2020-2064, DOI: 10.1039/c7cs00464h

18.      Thomas, E.; Thomas, D.; Bhuvaneswari, S.; Vijayalakshmi, K. P.; George, B. K., 1-Hexadecyl-3-methylimidazolium chloride: Structure, thermal stability and decomposition mechanism. *Journal of Molecular Liquids* **2018,** *249*, 404-411, DOI: 10.1016/j.molliq.2017.11.029

19.      Inoue, T.; Ebina, H.; Dong, B.; Zheng, L. Q., Electrical conductivity study on micelle formation of long-chain imidazolium ionic liquids in aqueous solution. *Journal of Colloid and Interface Science* **2007,** *314* (1), 236-241, DOI: 10.1016/J.JCIS.2007.05.052

20.      Zheng, W.; Mohammed, A.; Hines, L. G.; Xiao, D.; Martinez, O. J.; Bartsch, R. A.; Simon, S. L.; Russina, O.; Triolo, A.; Quitevis, E. L., Effect of Cation Symmetry on the Morphology and Physicochemical Properties of Imidazolium Ionic Liquids. *Journal of Physical Chemistry B* **2011,** *115* (20), 6572-6584, DOI: 10.1021/jp1115614

21.      Bowlas, C. J.; Bruce, D. W.; Seddon, K. R., Liquid-crystalline ionic liquids. *Chemical Communications* **1996,** (14), 1625-1626, DOI: 10.1039/cc9960001625

22.      Holbrey, J. D.; Seddon, K. R., The phase behaviour of 1-alkyl-3-methylimidazolium tetrafluoroborates; ionic liquids and ionic liquid crystals. *Journal of the Chemical Society-Dalton Transactions* **1999,** (13), 2133-2139, DOI: 10.1039/a902818h

23.      Gordon, C. M.; Holbrey, J. D.; Kennedy, A. R.; Seddon, K. R., Ionic liquid crystals: hexafluorophosphate salts. *Journal of Materials Chemistry* **1998,** *8* (12), 2627-2636, DOI: 10.1039/a806169f

24.      Hayes, R.; Warr, G. G.; Atkin, R., Structure and Nanostructure in Ionic Liquids. *Chemical Reviews* **2015,** *115* (13), 6357-6426, DOI: 10.1021/cr500411q

25.      Goossens, K.; Lava, K.; Bielawski, C. W.; Binnemans, K., Ionic Liquid Crystals: Versatile Materials. *Chemical Reviews* **2016,** *116* (8), 4643-4807, DOI: 10.1021/cr400334b

26.      Lee, C. K.; Huang, H. W.; Lin, I. J. B., Simple amphiphilic liquid crystalline N-alkylimidazolium salts. A new solvent system providing a partially ordered environment. *Chemical Communications* **2000,** (19), 1911-1912, DOI: 10.1039/b004462h

27.      Plechkova, N. V.; Seddon, K. R., Applications of ionic liquids in the chemical industry. *Chemical Society Reviews* **2008,** *37* (1), 123-150, DOI: 10.1039/b006677j

28.      Gutowski, K. E., Industrial uses and applications of ionic liquids. *Physical Sciences Reviews* **2018,** *3* (5), 1, DOI: 10.1515/psr-2017-0191

29.      George, A.; Brandt, A.; Tran, K.; Zahari, S.; Klein-Marcuschamer, D.; Sun, N.; Sathitsuksanoh, N.; Shi, J.; Stavila, V.; Parthasarathi, R.; Singh, S.; Holmes, B. M.; Welton, T.; Simmons, B. A.; Hallett,

J. P., Design of low-cost ionic liquids for lignocellulosic biomass pretreatment. *Green Chemistry* **2015,** *17* (3), 1728-1734, DOI: 10.1039/c4gc01208a

30.     Thi, P. T. P.; Cho, C. W.; Yun, Y. S., Environmental fate and toxicity of ionic liquids: A review. *Water Research* **2010,** *44* (2), 352-372, DOI: 10.1016/j.watres.2009.09.030

31.     Scammells, P. J.; Scott, J. L.; Singer, R. D., Ionic liquids: The neglected issues. *Australian Journal of Chemistry* **2005,** *58* (3), 155-169, DOI: 10.1071/CH04272

32.     Jastorff, B.; Stormann, R.; Ranke, J.; Molter, K.; Stock, F.; Oberheitmann, B.; Hoffmann, W.; Hoffmann, J.; Nuchter, M.; Ondruschka, B.; Filser, J., How hazardous are ionic liquids? Structure-activity relationships and biological testing as important elements for sustainability evaluation. *Green Chemistry* **2003,** *5* (2), 136-142, DOI: 10.1039/b211971d.

33.     Petkovic, M.; Seddon, K. R.; Rebelo, L. P. N.; Pereira, C. S., Ionic liquids: a pathway to environmental acceptability. *Chemical Society Reviews* **2011,** *40* (3), 1383-1403, DOI: 10.1039/c004968a

34.     Zhu, S.; Chen, R.; Wu, Y.; Chen, Q.; Zhang, X.; Yu, Z., A Mini-Review on Greenness of Ionic Liquids. *Chemical and Biochemical Engineering Quarterly* **2009,** *23* (2), 207-211, DOI: NA

35.     Hulsbosch, J.; De Vos, D. E.; Binnemans, K.; Ameloot, R., Biobased Ionic Liquids: Solvents for a Green Processing Industry? *Acs Sustainable Chemistry & Engineering* **2016,** *4* (6), 2917-2931, DOI: 10.1021/acssuschemeng.6b00553

36.     Ostadjoo, S.; Berton, P.; Shamshina, J. L.; Rogers, R. D., Scaling-Up Ionic Liquid-Based Technologies: How Much Do We Care About Their Toxicity? Prima Facie Information on 1-Ethyl-3-Methylimidazolium Acetate. *Toxicological Sciences* **2018,** *161* (2), 249-265, DOI: 10.1093/toxsci/kfx172

37.     Neumann, J.; Steudte, S.; Cho, C. W.; Thoming, J.; Stolte, S., Biodegradability of 27 pyrrolidinium, morpholinium, piperidinium, imidazolium and pyridinium ionic liquid cations under aerobic conditions. *Green Chemistry* **2014,** *16* (4), 2174-2184, DOI: 10.1039/c3gc41997e

38.     Barycki, M.; Sosnowska, A.; Puzyn, T., AquaBoxIL - a computational tool for determining the environmental distribution profile of ionic liquids. *Green Chemistry* **2018,** *20* (14), 3359-3370, DOI: 10.1039/c8gc01582a

39.     Wu, B.; Dai, C. N.; Chen, B. H.; Yu, G. Q.; Liu, N.; Xu, R. N., Ionic Liquid versus Traditional Volatile Organic Solvent in the Natural Gas Dehydration Process: A Comparison from a Life Cycle Perspective. *Acs Sustainable Chemistry & Engineering* **2019,** *7* (23), 19194-19201, DOI: 10.1021/acssuschemeng.9b05194

40.     M'Sahel, M.; Obadia, M. M.; Medimagh, R.; Serghei, A.; Zina, M. S.; Drockenmuller, E., Biosourced 1,2,3-triazolium ionic liquids derived from isosorbide. *New Journal of Chemistry* **2016,** *40* (1), 740-747, DOI: 10.1039/c5nj02660a

41.     Elloumi, A. K.; Miladi, I. A.; Serghei, A.; Taton, D.; Aissou, K.; Ben Romdhane, H.; Drockenmuller, E., Partially Biosourced Poly(1,2,3-triazolium)-Based Diblock Copolymers Derived from Levulinic Acid. *Macromolecules* **2018,** *51* (15), 5820-5830, DOI: 10.1021/acs.macromol.8b00962

42.     Kwan, M. L.; Mirjafari, A.; McCabe, J. R.; O'Brien, R. A.; Essi, D. F.; Baum, L.; West, K. N.; Davis, J. H., Synthesis and thermophysical properties of ionic liquids: cyclopropyl moieties versus olefins as T-m-reducing elements in lipid-inspired ionic liquids. *Tetrahedron Letters* **2013,** *54* (1), 12-14, DOI: 10.1016/j.tetlet.2012.09.101

43.     Langham, J. V.; O'Brien, R. A.; Davis, J. H.; West, K. N., Solubility of CO2 and N2O in an Imidazolium-Based Lipidic Ionic Liquid. *Journal of Physical Chemistry B* **2016,** *120* (40), 10524-10530, DOI: 10.1021/acs.jpcb.6b05474

44.     Murray, S. M.; O'Brien, R. A.; Mattson, K. M.; Ceccarelli, C.; Sykora, R. E.; West, K. N.; Davis, J. H., The Fluid-Mosaic Model, Homeoviscous Adaptation, and Ionic Liquids: Dramatic Lowering of the Melting Point by Side-Chain Unsaturation. *Angewandte Chemie-International Edition* **2010,** *49* (15), 2755-2758, DOI: 10.1002/anie.200906169

45.     Green, B. D.; O'Brien, R. A.; Davis, J. H.; West, K. N., Ethane and Ethylene Solubility in an Imidazolium-Based Lipidic Ionic Liquid. *Industrial & Engineering Chemistry Research* **2015,** *54* (18), 5165-5171, DOI: 10.1021/ie505071t

46.     Murray, S. M.; Zimlich, T. K.; Mirjafari, A.; O'Brien, R. A.; Davis, J. H.; West, K. N., Thermophysical Properties of Imidazolium-Based Lipidic Ionic Liquids. *Journal of Chemical and Engineering Data* **2013,** *58* (6), 1516-1522, DOI: 10.1021/je301004f

47.     Mirjafari, A.; Murray, S. M.; O'Brien, R. A.; Stenson, A. C.; West, K. N.; Davis, J. H., Structure-based tuning of T-m in lipid-like ionic liquids. Insights from Tf2N- salts of gene transfection agents. *Chemical Communications* **2012,** *48* (60), 7522-7524, DOI: 10.1039/c2cc33609j

48.     Sasi, R.; Sarojam, S.; Devaki, S. J., High Performing Biobased Ionic Liquid Crystal Electrolytes for Supercapacitors. *Acs Sustainable Chemistry & Engineering* **2016,** *4* (6), 3535-3543, DOI: 10.1021/acssuschemeng.6b00585

49.     Nan, H.; Zhang, C.; O'Brien, R. A.; Benchea, A.; Davis, J. H.; Anderson, J. L., Lipidic ionic liquid stationary phases for the separation of aliphatic hydrocarbons by comprehensive two-dimensional gas chromatography. *Journal of Chromatography A* **2017,** *1481*, 127-136, DOI: 10.1016/j.chroma.2016.12.032

50.     Sasi, R.; Jinesh, K. B.; Devaki, S. J., Anisotropic Phase Formation Induced Enhancement of Resistive Switching in Bio-based Imidazolium Ionic Liquid Crystals. *Chemistryselect* **2017,** *2* (1), 315-319, DOI: 10.1002/slct.201601715

51.     Costa, S. P. F.; Azevedo, A. M. O.; Pinto, P.; Saraiva, M., Environmental Impact of Ionic Liquids: Recent Advances in (Eco)toxicology and (Bio)degradability. *Chemsuschem* **2017,** *10* (11), 2321-2347, DOI: 10.1002/cssc.201700261

52.     Gathergood, N.; Scammells, P. J., Design and preparation of room-temperature ionic liquids containing biodegradable side chains. *Australian Journal of Chemistry* **2002,** *55* (9), 557-560, DOI: 10.1071/CH02148

53.     Garcia, M. T.; Gathergood, N.; Scammells, P. J., Biodegradable ionic liquids - Part II. Effect of the anion and toxicology. *Green Chemistry* **2005,** *7* (1), 9-14, DOI: 10.1039/b411922c

54.     Gathergood, N.; Garcia, M. T.; Scammells, P. J., Biodegradable ionic liquids: Part I. Concept, preliminary targets and evaluation. *Green Chemistry* **2004,** *6* (3), 166-175, DOI: 10.1039/b315270g

55.     Gathergood, N.; Scammells, P. J.; Garcia, M. T., Biodegradable ionic liquids - Part III. The first readily biodegradable ionic liquids. *Green Chemistry* **2006,** *8* (2), 156-160, DOI: 10.1039/b516206h

56.     Harjani, J. R.; Farrell, J.; Garcia, M. T.; Singer, R. D.; Scammells, P. J., Further investigation of the biodegradability of imidazolium ionic liquids. *Green Chemistry* **2009,** *11* (6), 821-829, DOI: 10.1039/b900787c

57.     Tseng, J. C. W.; Rondla, R.; Su, P. Y. S.; Lin, I. J. B., The roles of betaine-ester analogues of 1-N-alkyl-3-N '-methyl imidazolium salts: as amphotropic ionic liquid crystals and organogelators. *Rsc Advances* **2013,** *3* (47), 25151-25158, DOI: 10.1039/c3ra43067g

58.     Al-Mohammed, N. N.; Hussen, R. S. D.; Ali, T. H.; Alias, Y.; Abdullah, Z., Tetrakis-imidazolium and benzimidazolium ionic liquids: a new class of biodegradable surfactants. *Rsc Advances* **2015,** *5* (28), 21865-21876, DOI: 10.1039/c4ra16811a

59.     Garcia, M. T.; Ribosa, I.; Perez, L.; Manresa, A.; Comelles, F., Aggregation Behavior and Antimicrobial Activity of Ester-Functionalized Imidazolium- and Pyridinium-Based Ionic Liquids in Aqueous Solution. *Langmuir* **2013,** *29* (8), 2536-2545, DOI: 10.1021/la304752e

60.     Bodor, N.; Kaminski, J. J.; Selk, S., SOFT DRUGS .1. LABILE QUATERNARY AMMONIUM-SALTS AS SOFT ANTI-MICROBIALS. *Journal of Medicinal Chemistry* **1980,** *23* (5), 470-474, DOI: NA

61.     The biodegradation of the IL(C)s synthesized in this work was not tested.

62.     Li, X.; Ni, X. F.; Liang, Z. H.; Shen, Z. Q., Preparation of main-chain imidazolium-functionalized amphiphilic block copolymers through combination of condensation polymerization and nitroxide-mediated free radical polymerization and their micelle study. *Journal of Polymer Science Part a-Polymer Chemistry* **2012,** *50* (10), 2037-2044, DOI: 10.1002/pola.25978

63.     Maton, C.; De Vos, N.; Stevens, C. V., Ionic liquid thermal stabilities: decomposition mechanisms and analysis tools. *Chemical Society Reviews* **2013,** *42* (13), 5963-5977, DOI: 10.1039/c3cs60071h

64.     Nishikawa, K.; Wang, S. L.; Katayanagi, H.; Hayashi, S.; Hamaguchi, H. O.; Koga, Y.; Tozaki, K. I., Melting and freezing behaviors of prototype ionic liquids, 1-butyl-3-methylimidazolium bromide and

its chloride, studied by using a nano-watt differential scanning calorimeter. *Journal of Physical Chemistry B* **2007,** *111* (18), 4894-4900, DOI: 10.1021/jp0671852

65.    McDaniel, J. G.; Yethiraj, A., Understanding the Properties of Ionic Liquids: Electrostatics, Structure Factors, and Their Sum Rules. *Journal of Physical Chemistry B* **2019,** *123* (16), 3499-3512, DOI: 10.1021/acs.jpcb.9b00963

66.    Yang, K.; Cai, Z. K.; Jaiswal, A.; Tyagi, M.; Moore, J. S.; Zhang, Y., Dynamic Odd-Even Effect in Liquid n-Alkanes near Their Melting Points. *Angewandte Chemie-International Edition* **2016,** *55* (45), 14090-14095, DOI: 10.1002/anie.201607316

67.    Bradley, A. E.; Hardacre, C.; Holbrey, J. D.; Johnston, S.; McMath, S. E. J.; Nieuwenhuyzen, M., Small-angle X-ray scattering studies of liquid crystalline 1-alkyl-3-methylimidazolium salts. *Chemistry of Materials* **2002,** *14* (2), 629-635, DOI: 10.1021/cm010542v

68.    Godinho, M. H.; Cruz, C.; Teixeira, P. I. C.; Ferreira, A. J.; Costa, C.; Kulkarni, P. S.; Afonso, C. A. M., Shear-induced lamellar phase of an ionic liquid crystal at room temperature. *Liquid Crystals* **2008,** *35* (2), 103-107, DOI: 10.1080/02678290701824181

69.    Downard, A.; Earle, M. J.; Hardacre, C.; McMath, S. E. J.; Nieuwenhuyzen, M.; Teat, S. J., Structural studies of crystalline 1-alkyl-3-methylimidazolium chloride salts. *Chemistry of Materials* **2004,** *16* (1), 43-48, DOI: 10.1021/cm034344a

70.    Li, T.; Xu, F.; Shi, W., Ionic liquid crystals based on 1-alkyl-3-methylimidazolium cations and perfluorinated sulfonylimide anions. *Chemical Physics Letters* **2015,** *628*, 9-15, DOI: 10.1016/j.cplett.2015.04.003

**Table of content**
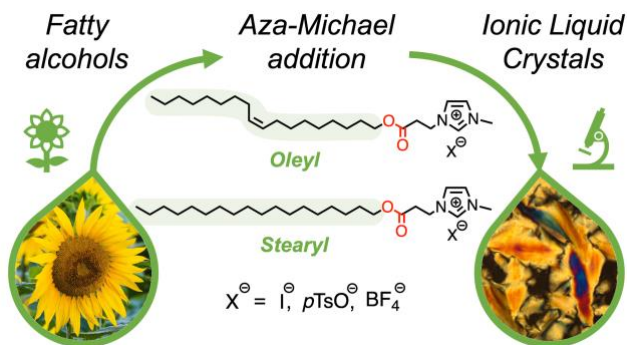
**Synopsys**

Ester-containing imidazolium-type ionic liquid crystals were synthesized according to an industrially-viable protocol based on the aza-Michael addition of imidazole onto biobased fatty acrylates.

# Ester-containing imidazolium ionic liquid crystals derived from biobased fatty alcohols

*Enrique del Río, Thomas Vidil\*, Wafa Gati, Étienne Grau, Daniel Taton\*, Henri Cramail\**

Univ. Bordeaux, CNRS, Bordeaux INP, LCPO, UMR 5629, F-33600, Pessac, France

\*To whom correspondence should be addressed:

thomas.vidil@enscbp.fr,

daniel.taton@enscbp.fr,

henri.cramail@enscbp.fr

Number of pages: 82

Number of figures: 86

Number of tables: 3

**Note**: no unexpected or unusually high safety hazards were encountered with the reported work

# 1. Materials

Oleyl alcohol (>98%, NuCheck Prep Inc.) was used as received. 1-Undecenol, 1-Undecanol, methyl acrylate, lauryl acrylate, stearyl acrylate, acryloyl chloride, methyl-para-toluene sulfonate, methyl iodide, $AgBF_4$ were supplied by Aldrich and used as received. Methanol used for anion metathesis was dried over sodium methoxide and freshly distilled prior to use. Acetonitrile was dried over activated molecular sieves and freshly distilled prior to use. Dichloromethane was dried with Glass Contour solvent purification system.

# 2. Methods

*Nuclear Magnetic Resonance*

NMR spectra of all compounds were recorded in the indicated deuterated solvent at 298 K on a Bruker Advance I NMR spectrometer (400 MHz for $^1$H NMR, 100 MHz for $^{13}$C NMR). Chemical shifts are reported in parts per million (ppm) on the $\delta$ scale relative to $Me_4Si$ ($\delta$ = 0 ppm for $^1$H NMR), $CDCl_3$ ($\delta$ = 77.2 ppm for $^{13}$C NMR) as internal references.

*High Resolution Mass Spectrometry*

High-resolution Mass spectra were performed by the CESAMO (Bordeaux, France) on a Qexactive mass spectrometer (Thermo Scientific). The instrument is equipped with an ESI source and spectra were recorded in both the negative and the positive ion mode. The spray voltage was maintained at 3200 V and capillary temperature set at 320°C. Samples were introduced by injection through a 20 $\mu$L sample loop into a 300 $\mu$L min$^{-1}$ flow of methanol from the LC pump.

*Thermogravimetric analysis*

TGA were performed using a TA instruments Q50 under nitrogen or air atmosphere, from room temperature to 700 °C at 10 °C min$^{-1}$ with typical sample size of 10-15 mg in Pt pans. The weight loss was recorded as a function of temperature.

*Differential scanning calorimetry*

DSC thermograms were performed on a DSC Q100 apparatus from TA instruments using standard aluminum T-zero pans with hermetic lids containing 5 to 10 mg of the sample. Scans were conducted under an inert atmosphere ($N_2$). For each sample, two cycles from -120 to 200 °C at 10 °C min$^{-1}$ were performed, and the transition temperatures were calculated from the cooling run for the isotropic liquid to liquid crystal transition and the crystallization, and from the second heating run for the melting and the liquid crystal to isotropic liquid transition.

*Polarized optical microscopy*

POM was carried out using a Zeiss AX10 Lab.A1 microscope under cross-polarized light. The samples were sandwiched in-between a microscope slide and a cover glass. The pictures were recorded using a Zeiss Axiocam 105 color camera. The temperature was varied using a Mettler Toledo FP82HT Hot stage controlled with a Mettler Toledo FP90 Central processor.

*Small Angle X-Ray Scattering*

SAXS experiments were performed at the Centre de Recherche Paul Pascal (CRPP) at Université de Bordeaux using a high-resolution X-ray spectrometer Xeuss 2.0 from Xenoxs operating with radiation wavelength of $\lambda = 1.54$ Å. 2D scattering patterns were collected by using a PILATUS 300 K Dectris detector with a sample-to-detector distance of 1631 mm. The beam center position and the angular range were calibrated by using a silver behenate standard sample. The SAXS patterns were radially averaged around the direct beam position by using the Xenocs XSACT software. Samples were heated using a Peltier device with a heating rate of 10 °C min$^{-1}$.

*Single crystal X-ray analysis*

The data for the crystal structure were collected on a Bruker microstar X8 PROTEUM with a classical kappa geometry and Platinum135 CCD camera. The structures were solved by the AB-initio method implemented in SHELXD and refined with SHELXL.[1] Full-matrix least-squares refinement was performed on F2 for all unique reflections, minimizing w(Fo2-Fc2)2, with anisotropic displacement parameters for non-hydrogen atoms. The positions of the H atoms were deduced from coordinates of the non-H atoms. The non-H atoms were refined with anisotropic temperature parameters.

# 3. General synthetic procedures and NMR data

## 3.1. General procedure for the synthesis of alkyl acrylate
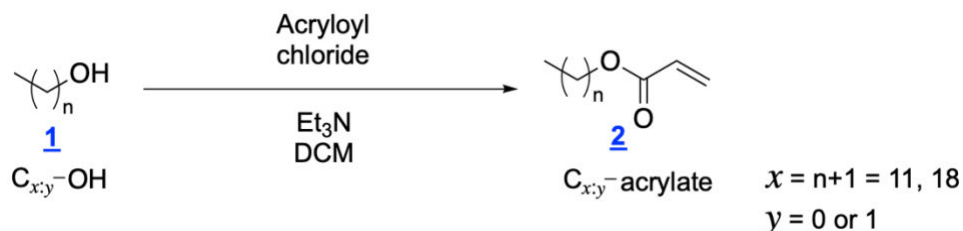


**Scheme S1**: Acrylation of the fatty alcohols

All acrylates were synthesized following a reported procedure.[2] Alcohol (26.4 mmol), 20 mL of dry dichloromethane and 1.5 equivalents of dry triethylamine (39.6 mmol) are introduced in a flame-dried

flask equipped with a magnetic stirring bar. The reaction mixture is then cooled to 0 °C after which 1.3 equivalents of acryloyl chloride (34.3 mmol) are added dropwise. The cold bath is then removed, and the reaction mixture is stirred at room temperature for two hours. Once the reaction is finished, the dichloromethane is evaporated and replaced by petroleum ether. The resulting precipitate is filtrated off over celite. The organic phase obtained is washed with 10 % HCl (2 × 20 mL), saturated solution of sodium bicarbonate (2 × 20 mL) and brine. Finally, the obtained solution is dried over magnesium sulfate and the solvent is evaporated under reduced pressure to obtain a crude material that is used in the next step without further purification.

### 3.2. General procedure for the Michael addition of imidazole to the acrylates, synthesis of 1-alkylpropionate-imidazole $C_{x:y}E_{(2)}$Im
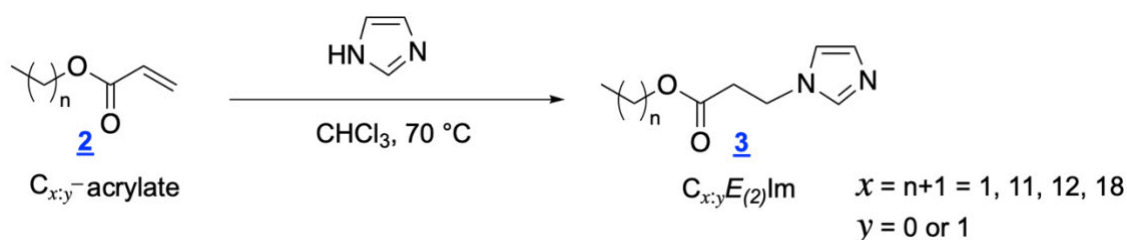


**Scheme S2**: Aza-Michael addition of imidazole onto the fatty acrylates

Acrylate (12.4 mmol), 10 mL of chloroform and 1.5 equivalents of imidazole (18.6 mmol) are introduced in a 50 mL round button flask equipped with a magnetic stirring bar. The reaction is heated under reflux for one day and monitored by $^1$H NMR. Upon reaction completion, the chloroform is evaporated under reduced pressure and the resulting product is purified by flash chromatography using gradient mixture of ethyl acetate and heptane.

In the case of methyl acrylate, the reaction is conducted in presence of excess of acrylate (1.5 equivalents). After reaction completion, all solvent and excess of acrylate are evaporated under reduced pressure. The resulting crude material is obtained in satisfying purity and is used without further purification in the next step.
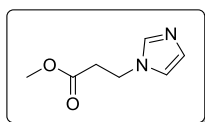

$C_{1:0}E_{(2)}$Im *1-methylpropionate-imidazole*. $^1$H-NMR (CDCl$_3$, 400 MHz) δ (ppm): 7.35 (s, N-C*H*-N, 1 H), 6.86 (s, N-CH-C*H*-N, 1 H), 6.79 (s, N-C*H*-CH-N, 1 H), 4.11 (t, CH$_2$-C*H*$_2$-N, 2 H, *J*= 6.4 Hz), 3.52 (s, C*H*$_3$-O, 3 H), 2.63 (t, CO-C*H*$_2$-CH$_2$, 2 H, J = 6.8 Hz). $^{13}$C-NMR (CDCl$_3$, 100 MHz) δ (ppm): 170.9 (C=O), 137.1 (N-*C*H-N), 129.4 (N-*C*H-CH-N), 118.8 (N-CH-*C*H-N), 51.9 (*C*H$_3$-O), 42.1 (CH$_2$-*C*H$_2$-N), 35.6 (CO-*C*H$_2$-CH$_2$).
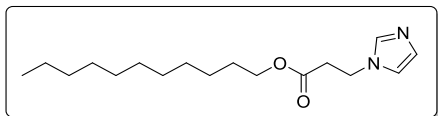
 C$_{11:0}$E$_{(2)}$Im 1-undecanylpropionate-Imidazole. 82% yield. $^1$H-NMR (CDCl$_3$, 400 MHz) δ (ppm): 7.42 (s, N-C*H*-N, 1 H), 6.94 (s, N-CH-C*H*-N, 1 H), 6.85 (s, N-C*H*-CH-N, 1 H), 4.18 (t, CH$_2$-C*H$_2$*-N, 2 H, *J* = 6.4 Hz), 3.99 (t, CH$_2$-C*H$_2$*-O, 2 H, *J* = 6.8 Hz), 2.69 (t, CO-C*H$_2$*-CH$_2$, 2 H, *J* = 6.8 Hz), 1.51 (m, C*H$_2$*-CH$_2$-O, 2 H), 1.25-1.10 (m, CH$_3$-(C*H$_2$*)$_8$, 16 H), 0.80 (t, C*H$_3$*-CH$_2$, 3 H, *J* = 6.8 Hz). $^{13}$C-NMR (CDCl$_3$, 100 MHz) δ (ppm): 170.7 (C=O), 137.2 (N-*C*H-N), 129.5 (N-*C*H-CH-N), 118.8 (N-CH-*C*H-N), 65.2 (CH$_2$-*C*H$_2$-O), 42.2 (CH$_2$-*C*H$_2$-N), 36.0 (CO-*C*H$_2$-CH$_2$), 31.9 (*C*H$_2$-CH$_2$-O), 30 − 22 (CH$_3$-(*C*H$_2$)$_8$), 14.1 (*C*H$_3$-CH$_2$).
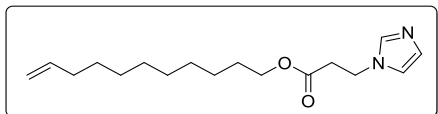
 C$_{11:1}$E$_{(2)}$Im 1-undecenylpropionate-imidazole. 84% yield. $^1$H-NMR (CDCl$_3$, 400 MHz) δ (ppm): 7.42 (s, N-C*H*-N, 1 H), 6.94 (s, N-CH-C*H*-N, 1 H), 6.85 (s, N-C*H*-CH-N, 1 H), 5.72 (m, CH2=C*H*, 1 H), 4.88 (d, C*H$_2$*=CH, 1 H, *J* = 17.2 Hz), 4.83 (d, C*H$_2$*=CH, 1 H, *J* = 10.0 Hz), 4.17 (t, CH$_2$-C*H$_2$*-N, 2 H, *J* = 6.4 Hz), 3.99 (t, CH$_2$-C*H$_2$*-O, 2 H, *J* = 6.8 Hz), 2.68 (t, CO-C*H$_2$*-CH$_2$, 2 H, *J* = 6.8 Hz), 1.95 (m, CH$_2$=CH-C*H$_2$*, 2 H), 1.51 (m, C*H$_2$*-CH$_2$-O, 2 H), 1.3-1.1 (m, (CH$_2$)$_6$, 12 H). $^{13}$C-NMR (CDCl$_3$, 100 MHz) δ (ppm): 170.5 (C=O), 139.0 (CH$_2$=*C*H), 137.2 (N-*C*H-N), 129.5 (N-*C*H-CH-N), 118.7 (N-CH-*C*H-N), 114.1 (*C*H$_2$=CH) 65.2 (CH$_2$-*C*H$_2$-O), 42.2 (CH$_2$-*C*H$_2$-N), 35.8 (CO-*C*H$_2$-CH$_2$), 33.6 (*C*H$_2$-CH$_2$-O), 30 − 25 ((*C*H$_2$)$_7$).
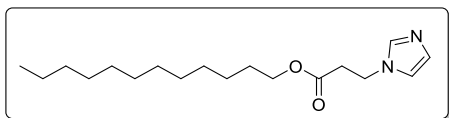
 C$_{12:0}$E$_{(2)}$Im 1-dodecanylpropionate-imidazole. 87% yield. $^1$H-NMR (CDCl$_3$, 400 MHz) δ (ppm): 7.52 (s, N-C*H*-N, 1 H), 7.03 (s, N-CH-C*H*-N, 1 H), 6.92 (s, N-C*H*-CH-N, 1 H), 4.24 (t, CH$_2$-C*H$_2$*-N, 2 H, *J* = 6.8 Hz), 4.06 (t, CH$_2$-C*H$_2$*-O, 2 H, *J* = 6.8 Hz), 2.75 (t, CO-C*H$_2$*-CH$_2$, 2 H, *J* = 6.8 Hz), 1.58 (m, C*H$_2$*-CH$_2$-O, 2 H), 1.3-1.1 (m, CH$_3$-(C*H$_2$*)$_9$, 18 H), 0.86 (t, C*H$_3$*-CH$_2$, 3 H, *J* = 6.8 Hz) . $^{13}$C-NMR (CDCl$_3$, 100 MHz) δ (ppm): 170.6 (C=O), 137.3 (N-*C*H-N), 129.5 (N-*C*H-CH-N), 118.8 (N-CH-*C*H-N), 65.3 (CH$_2$-*C*H$_2$-O), 42.3 (CH$_2$-*C*H$_2$-N), 36.1 (CO-*C*H$_2$-CH$_2$), 32.0 (*C*H$_2$-CH$_2$-O), 30 − 22 (CH$_3$-(*C*H$_2$)$_9$), 14.2 (*C*H$_3$-CH$_2$).
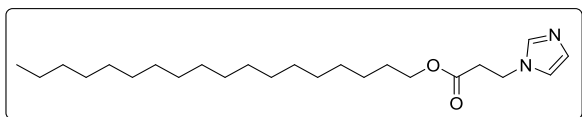
 C$_{18:0}$E$_{(2)}$Im 1-octadecanylpropionate-imidazole. 90% yield. $^1$H-NMR (CDCl$_3$, 400 MHz) δ (ppm): 7.59 (s, N-C*H*-N, 1 H), 7.10 (s, N-CH-C*H*-N, 1 H), 6.94 (s, N-C*H*-CH-N, 1 H), 4.27 (t, CH$_2$-C*H$_2$*-N, 2 H, *J* = 6.4 Hz), 4.08 (t, CH$_2$-C*H$_2$*-O, 2 H, *J* = 6.8 Hz), 2.77 (t, CO-C*H$_2$*-CH$_2$, 2 H, *J* = 6.8 Hz), 1.58 (m, C*H$_2$*-CH$_2$-O, 2 H), 1.3-1.1 (m, CH$_3$-(C*H$_2$*)$_{15}$, 30 H), 0.88 (t, C*H$_3$*-CH$_2$, 3 H, *J* = 6.8 Hz). $^{13}$C-NMR (CDCl$_3$, 100 MHz) δ (ppm): 170.6 (C=O), 137.2 (N-*C*H-N), 129.4 (N-*C*H-CH-N), 118.9 (N-CH-*C*H-N), 65.4 (CH$_2$-*C*H$_2$-O), 42.4 (CH$_2$-*C*H$_2$-N), 36.1 (CO-*C*H$_2$-CH$_2$), 32.0 (*C*H$_2$-CH$_2$-O), 30 − 22 (CH$_3$-(*C*H$_2$)$_{15}$), 14.2 (*C*H$_3$-CH$_2$).
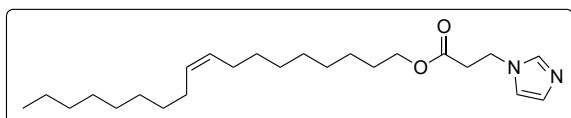
 C$_{18:1}$E$_{(2)}$Im 1-octadecenylpropionate-imidazole. 87% yield. $^1$H-NMR (CDCl$_3$, 400 MHz) δ (ppm): 7.42 (s, N-C*H*-N, 1 H), 6.95 (s, N-CH-C*H*-N, 1 H), 6.85 (s, N-C*H*-CH-

N, 1 H), 5.26 (m, C$H$=C$H$, 2 H), 4.18 (t, CH$_2$-C$H_2$-N, 2 H, $J$ = 6.4 Hz), 3.99 (t, CH$_2$-C$H_2$-O, 2 H, $J$ = 6.8 Hz), 2.68 (t, CO-C$H_2$-CH$_2$, 2 H, $J$ = 6.8 Hz), 1.93 (m, C$H_2$-CH=CH, 4 H), 1.51 (m, C$H_2$-CH$_2$-O, 2 H), 1.3-1.1 (m, CH$_3$-(C$H_2$)$_{11}$, 22 H), 0.80 (t, C$H_3$-CH$_2$, 3 H, $J$ = 6.8 Hz). $^{13}$C-NMR (CDCl$_3$, 100 MHz) δ (ppm): 170.5 (C=O), 137.2 (N-$C$H-N), 129.9 ($C$H=CH), 129.6 (CH=$C$H), 129.5 (N-$C$H-CH-N), 118.7 (N-CH-$C$H-N), 65.2 (CH$_2$-$C$H$_2$-O), 42.2 (CH$_2$-$C$H$_2$-N), 35.9 (CO-$C$H$_2$-CH$_2$), 31.8 ($C$H$_2$-CH$_2$-O), 30 − 22 (CH$_3$-($C$H$_2$)$_{13}$), 14.0 ($C$H$_3$-CH$_2$).

### 3.3. General procedure for the quaternization of C$_{x:y}$E$_{(2)}$Im with $p$TsOMe, synthesis of 1-alkylpropionate-3-methylimidazolium $p$-toluenesulfonate, [C$_{x:y}$E$_{(2)}$ImMe]$p$TsO
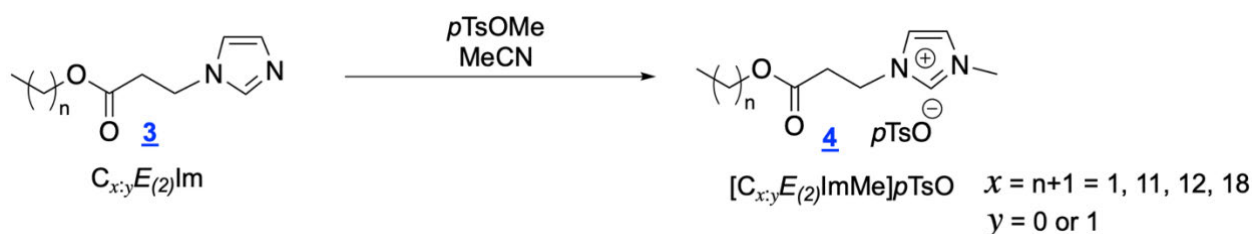


Scheme S3: Quaternization with methyl tosylate

1-alkylpropionate-imidazole (2.91 mmol), 3.5 mL of anhydrous acetonitrile and 1 equivalent of $p$TsOMe (2.91 mmol) were introduced in a Schlenk flask equipped with a magnetic bar and under nitrogen atmosphere. The reaction was heated at 70 °C for 24 hours. Once the reaction was completed, the solvent was evaporated under reduce pressure and the product was washed with diethylether (3 x 10 mL).
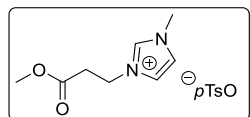


[C$_{1:0}$E$_{(2)}$ImMe]$p$TsO *[1-methylpropionate-3-methylimidazolium] p-toluenesulfonate.* 97% yield. $^1$H-NMR (CDCl$_3$, 400 MHz) δ (ppm): 9.56 (s, N-C$H$-N, 1 H), 7.68 (d, CH-Ar, 2 H, $J$ = 8 Hz) 7.49 (s, N-CH-C$H$-N, 1 H), 7.39 (s, N-C$H$-CH-N, 1 H), 7.09 (d, CH-Ar, 2 H, $J$ = 8 Hz), 4.42 (t, CH$_2$-C$H_2$-N, 2 H, $J$ = 6.4 Hz), 3.83 (s, C$H_3$-N, 3 H),  3.58 (s, C$H_3$-O, 3 H), 2.86 (t, CO-C$H_2$-CH$_2$, $J$ = 6.4 Hz) 2.28 (s, C$H_3$-CAr, 3 H). $^{13}$C-NMR (CDCl$_3$, 100 MHz) δ (ppm): 170.9 (C=O), 143.9 ($C$Ar), 139.4 ($C$Ar), 137.9 (N-$C$H-N), 128.7 ($C$HAr x 2), 125.8 ($C$HAr x 2), 123.5 (N-CH-$C$H-N), 123.0 (N-$C$H-CH-N), 52.2 ($C$H$_3$-O), 45.1 ($C$H$_2$-CH$_2$-N), 36.3 ($C$H$_3$-N), 34.3 (CO-$C$H$_2$-CH$_2$), 21.3 ($C$H$_3$-CAr).
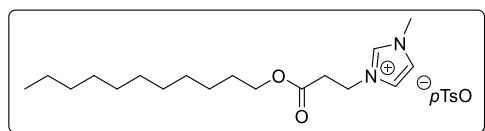


[C$_{11:0}$E$_{(2)}$ImMe]$p$TsO *1-undecanylpropionate-3-methylimidazolium p-toluenesulfonate.* 96% yield. $^1$H-NMR (CDCl$_3$, 400 MHz) δ (ppm): 9.62 (s, N-C$H$-N, 1 H), 7.71 (d, CH-Ar, 2 H, $J$ = 8.2 Hz), 7.46 (s, N-CH-C$H$-N, 1 H), 7.38 (s, N-C$H$-CH-N, 1 H), 7.10 (d, CH-Ar, 2 H, $J$ = 8.2 Hz), 4.45 (t, CH$_2$-C$H_2$-N, 2 H, $J$ = 6.0 Hz), 3.98 (t, CH$_2$-C$H_2$-O, 2 H, $J$ = 6.8 Hz), 3.87 (s, C$H_3$-N, 3 H), 2.86 (t, CO-C$H_2$-CH$_2$, 2 H, $J$ = 6.4 Hz), 2.30 (s, C$H_3$-CAr, 3 H), 1.53 (m, C$H_2$-CH$_2$-O, 2 H), 1.3-1.1 (m, CH$_3$-(C$H_2$)$_8$, 16

H), 0.84 (t, C$H_3$-CH$_2$, 3 H, $J$ = 6.8 Hz). $^{13}$C-NMR (CDCl$_3$, 100 MHz) δ (ppm): 170.7 (C=O), 143.8 (CAr), 139.4 (CAr), 138.1 (N-CH-N), 128.7 (CHAr x 2), 125.9 (CHAr x 2), 123.4 (N-CH-CH-N), 123.0 (N-CH-CH-N), 65.5 (CH$_2$-CH$_2$-O), 45.2 (CH$_2$-CH$_2$-N), 36.4 (CH$_3$-N), 34.6 (CO-CH$_2$-CH$_2$), 31.9 (CH$_2$-CH$_2$-O), 30 − 22 (CH$_3$-(CH$_2$)$_8$), 21.3 (CH$_3$-CAr), 14.1 (CH$_3$-CH$_2$). HRMS (ESI), m/z calculated for C$_{18}$H$_{33}$N$_2$O$_2$ [C$_{11:0}$E$_{(2)}$ImMe]$^+$: 309.25365, found 309.25294, m/z calculated for C$_7$H$_7$O$_3$S $p$TsO$^-$: 171.01214, found 171.01176.
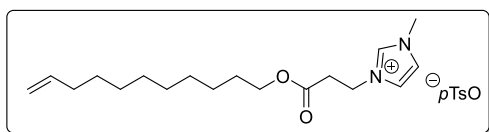


[C$_{11:1}$E$_{(2)}$ImMe]$p$TsO                1-undecenylpropionate-3-methylimidazolium *p-toluenesulfonate*. 94% yield.$^1$H-NMR (CDCl$_3$, 400 MHz) δ (ppm): 9.62 (s, N-CH-N, 1 H), 7.72 (d, CH-Ar, 2 H, $J$ = 8.2 Hz), 7.46 (s, N-CH-CH-N, 1 H), 7.40 (s, N-CH-CH-N, 1 H), 7.11 (d, CH-Ar, 2 H, $J$ = 7.6 Hz), 5.78 (m, CH2=CH, 1 H), 4.94 (d, CH$_2$=CH, 1 H, $J$ = 17.2 Hz), 4.88 (d, CH$_2$=CH, 1 H, $J$ = 10.0 Hz), 4.45 (t, CH$_2$-CH$_2$-N, 2 H, $J$ = 6.0 Hz), 3.99 (t, CH$_2$-CH$_2$-O, 2 H, $J$ = 6.8 Hz), 3.87 (s, CH$_3$-N, 3 H), 2.86 (t, CO-CH$_2$-CH$_2$, 2 H, $J$ = 6.4 Hz), 2.31 (s, CH$_3$-CAr, 3 H), 2.00 (m, CH$_2$=CH-CH$_2$, 2 H) 1.53 (m, CH$_2$-CH$_2$-O, 2 H), 1.4-1.1 (m, (CH$_2$)$_6$, 12 H). $^{13}$C-NMR (CDCl$_3$, 100 MHz) δ (ppm): 170.7 (C=O), 143.8 (CAr), 139.3 (CAr), 139.1 (CH$_2$=CH), 138.1 (N-CH-N), 128.7 (CHAr x 2), 125.9 (CHAr x 2), 123.4 (N-CH-CH-N), 123.0 (N-CH-CH-N), 114.2 (CH$_2$=CH) 65.5 (CH$_2$-CH$_2$-O), 45.1 (CH$_2$-CH$_2$-N), 36.4 (CH$_3$-N), 34.5 (CO-CH$_2$-CH$_2$), 33.8 (CH$_2$-CH$_2$-O), 30 − 25 ((CH$_2$)$_7$), 21.3 (CH$_3$-CAr). HRMS (ESI), m/z calculated for C$_{18}$H$_{31}$N$_2$O$_2$ [C$_{11:1}$E$_{(2)}$ImMe]$^+$: 307.23800, found 307.23736, m/z calculated for C$_7$H$_7$O$_3$S $p$TsO$^-$: 171.01214, found 171.01176.
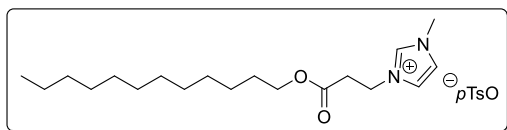


[C$_{12:0}$E$_{(2)}$ImMe]$p$TsO                1-dodecanylpropionate-3-methylimidazolium *p-toluenesulfonate*. 98% yield. $^1$H-NMR (CDCl$_3$, 400 MHz) δ (ppm): 9.70 (s, N-CH-N, 1 H), 7.75 (d, CH-Ar, 2 H, $J$ = 8.0 Hz), 7.48 (s, N-CH-CH-N, 1 H), 7.34 (s, N-CH-CH-N, 1 H), 7.13 (d, CH-Ar, 2 H, $J$ = 7.6 Hz), 4.52 (t, CH$_2$-CH$_2$-N, 2 H, $J$ = 6.4 Hz), 4.02 (t, CH$_2$-CH$_2$-O, 2 H, $J$ = 6.8 Hz), 3.93 (s, CH$_3$-N, 3 H), 2.91 (t, CO-CH$_2$-CH$_2$, 2 H, $J$ = 6.0 Hz), 2.34 (s, CH$_3$-CAr, 3 H), 1.57 (m, CH$_2$-CH$_2$-O, 2 H), 1.3-1.1 (m, CH$_3$-(CH$_2$)$_9$, 18 H), 0.88 (t, CH$_3$-CH$_2$, 3 H, $J$ = 7.2 Hz) . $^{13}$C-NMR (CDCl$_3$, 100 MHz) δ (ppm): 170.9 (C=O), 143.6 (CAr), 139.6 (CAr), 138.3 (N-CH-N), 128.8 (CHAr x 2), 125.9 (CHAr x 2), 123.2 (N-CH-CH-N), 123.1 (N-CH-CH-N), 65.6 (CH$_2$-CH$_2$-O), 45.3 (CH$_2$-CH$_2$-N), 36.5 (CH$_3$-N), 34.6 (CO-CH$_2$-CH$_2$), 32.0 (CH$_2$-CH$_2$-O), 30 − 22 (CH$_3$-(CH$_2$)$_9$), 21.4 (CH$_3$-CAr), 14.2 (CH$_3$-CH$_2$). HRMS (ESI), m/z calculated for C$_{19}$H$_{35}$N$_2$O$_2$ [C$_{12:0}$E$_{(2)}$ImMe]$^+$: 323.26930, found 323.26875, m/z calculated for C$_7$H$_7$O$_3$S $p$TsO$^-$: 171.01214, found 171.01171.
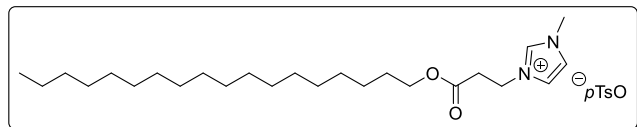
[C$_{18:0}$E$_{(2)}$ImMe]pTsO 1-octadecanylpropionate)-3-methylimidazolium *p-toluenesulfonate*. 99% yield. $^1$H-NMR (CDCl$_3$, 400 MHz) δ (ppm): 9.66 (s, N-C*H*-N, 1 H), 7.73 (d, CH-Ar, 2 H, *J* = 8.4 Hz), 7.48 (s, N-CH-C*H*-N, 1 H), 7.39 (s, N-C*H*-CH-N, 1 H), 7.12 (d, CH-Ar, 2 H, *J* = 8.0 Hz), 4.48 (t, CH$_2$-C*H$_2$*-N, 2 H, *J* = 6.0 Hz), 4.00 (t, CH$_2$-C*H$_2$*-O, 2 H, *J* = 6.8 Hz), 3.90 (s, C*H$_3$*-N, 3 H), 2.88 (t, CO-C*H$_2$*-CH$_2$, 2 H, *J* = 6.4 Hz), 2.32 (s, C*H$_3$*-CAr, 3 H), 1.53 (m, C*H$_2$*-CH$_2$-O, 2 H), 1.3-1.1 (m, CH$_3$-(C*H$_2$*)$_{15}$, 30 H), 0.86 (t, C*H$_3$*-CH$_2$, 3 H, *J* = 6.8 Hz). $^{13}$C-NMR (CDCl$_3$, 100 MHz) δ (ppm): 170.8 (C=O), 143.8 (*C*Ar), 139.4 (*C*Ar), 138.2 (N-*C*H-N), 128.7 (*C*HAr x 2), 125.9 (*C*HAr x 2), 123.3 (N-CH-*C*H-N), 123.0 (N-*C*H-CH-N), 65.5 (CH$_2$-*C*H$_2$-O), 45.2 (CH$_2$-*C*H$_2$-N), 36.4 (*C*H$_3$-N), 34.6 (CO-*C*H$_2$-CH$_2$), 32.0 (*C*H$_2$-CH$_2$-O), 30 − 22 (CH$_3$-(*C*H$_2$)$_{15}$), 21.3 (*C*H$_3$-CAr), 14.2 (*C*H$_3$-CH$_2$). HRMS (ESI), m/z calculated for C$_{25}$H$_{47}$N$_2$O$_2$ [C$_{18:0}$E$_{(2)}$ImMe]$^+$: 407.36430, found 407.36255, m/z calculated for C$_7$H$_7$O$_3$S pTsO$^-$: 171.01214, found 171.01168.
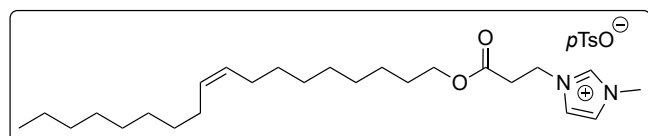


[C$_{18:1}$E$_{(2)}$ImMe]pTsO 1-octadec-9-enylpropionate)-3-methylimidazolium *p-toluenesulfonate*. 97% yield. $^1$H-NMR (CDCl$_3$, 400 MHz) δ (ppm): 9.76 (s, N-C*H*-N, 1 H), 7.76 (d, CH-Ar, 2 H, *J* = 8.4 Hz), 7.48 (s, N-CH-C*H*-N, 1 H), 7.34 (s, N-C*H*-CH-N, 1 H), 7.14 (d, CH-Ar, 2 H, *J* = 8.0 Hz), 5.34 (m, C*H*=C*H*, 2 H), 4.52 (t, CH$_2$-C*H$_2$*-N, 2 H, *J* = 6.0 Hz), 4.03 (t, CH$_2$-C*H$_2$*-O, 2 H, *J* = 6.8 Hz), 3.94 (s, C*H$_3$*-N, 3 H), 2.93 (t, CO-C*H$_2$*-CH$_2$, 2 H, *J* = 6.4 Hz), 2.33 (s, C*H$_3$*-CAr, 3 H), 2.00 (m, C*H$_2$*-CH=CH, 4 H), 1.57 (m, C*H$_2$*-CH$_2$-O, 2 H), 1.4-1.1 (m, CH$_3$-(C*H$_2$*)$_{11}$, 22 H), 0.88 (t, C*H$_3$*-CH$_2$, 3 H, *J* = 6.8 Hz). $^{13}$C-NMR (CDCl$_3$, 100 MHz) δ (ppm): 170.9 (C=O), 143.7 (*C*Ar), 139.4 (*C*Ar), 138.5 (N-*C*H-N), 130.1 (*C*H=CH), 129.8 (CH=*C*H), 128.8 (*C*HAr x 2), 125.9 (*C*HAr x 2), 123.1 (N-*C*H-*C*H-N x 2), 65.6 (CH$_2$-*C*H$_2$-O), 45.3 (CH$_2$-*C*H$_2$-N), 36.5 (*C*H$_3$-N), 34.7 (CO-*C*H$_2$-CH$_2$), 31.98 (*C*H$_2$-CH$_2$-O), 30 − 22 (CH$_3$-(*C*H$_2$)$_{13}$), 21.4 (*C*H$_3$-CAr), 14.2 (*C*H$_3$-CH$_2$). HRMS (ESI), m/z calculated for C$_{25}$H$_{45}$N$_2$O$_2$ [C$_{18:1}$E$_{(2)}$ImMe]$^+$: 405.34756, found 405.34712, m/z calculated for C$_7$H$_7$O$_3$S pTsO$^-$: 171.01214, found 171.01175.

### 3.4. General procedure for the quaternization of C$_{x:y}$E$_{(2)}$Im with MeI, synthesis of 1-alkylpropionate-3-methylimidazolium iodide, [C$_{x:y}$E$_{(2)}$ImMe]I
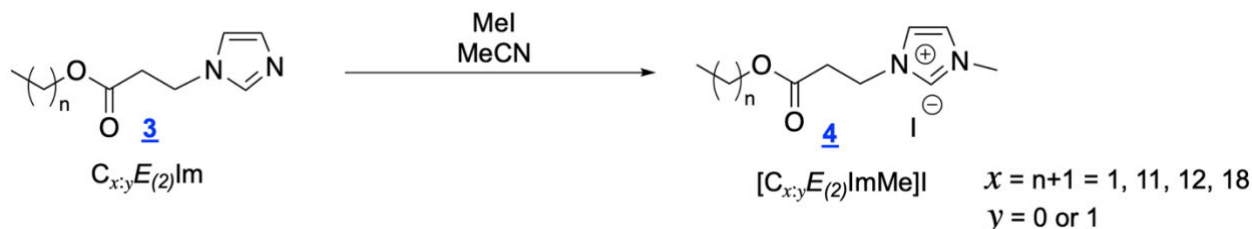


**Scheme S4**: Quaternization with methyl iodade

1-alkylpropionate-imidazole (2.09 mmol), 2.5 mL of anhydrous acetonitrile and 1.25 equivalent of MeI (2.5 mmol) were introduced in a Schlenk flask equipped with a magnetic bar under nitrogen atmosphere. The reaction was heated at 40 °C for 15 hours. Once the reaction was completed, the solvent and excess of MeI were evaporated under reduce pressure and the product was washed with diethylether (3 x 10 mL). Typical yield: quantitative, 100%
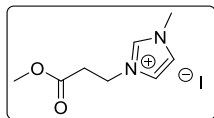
 [C$_{1:0}$E$_{(2)}$ImMe]I *1-methylpropionate-3-methylimidazolium iodide*. 96% yield. $^1$H-NMR (CDCl$_3$, 400 MHz) δ (ppm): 9.51 (s, N-C*H*-N, 1 H), 7.64 (s, N-CH-C*H*-N, 1 H), 7.53 (s, N-C*H*-CH-N, 1 H), 4.53 (t, CH$_2$-C*H$_2$*-N, 2 H, *J* = 6.4 Hz), 3.95 (s, C*H$_3$*-N, 3 H), 3.54 (s, C*H$_3$*-O, 3 H), 2.96 (t, CO-C*H$_2$*-CH$_2$, *J* = 6.4 Hz). $^{13}$C-NMR (CDCl$_3$, 100 MHz) δ (ppm): 170.7 (C=O), 136.9 (N-*C*H-N) 123.7 (N-*C*H-CH-N), 123.1 (N-CH-*C*H-N), 52.3 (*C*H$_3$-O), 45.4 (CH$_2$-*C*H$_2$-N), 37.2 (*C*H$_3$-N), 34.6 (CO-*C*H$_2$-CH$_2$).
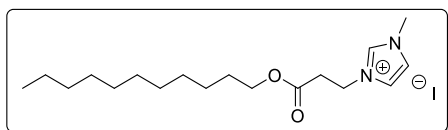
 [C$_{11:0}$E$_{(2)}$ImMe]I     *1-undecanylpropionate-3-methylimidazolium iodide*. 95% yield. $^1$H-NMR (CDCl$_3$, 400 MHz) δ (ppm): 9.84 (s, N-C*H*-N, 1 H), 7.65 (s, N-CH-C*H*-N, 1 H), 7.51 (s, N-C*H*-CH-N, 1 H), 4.65 (t, CH$_2$-C*H$_2$*-N, 2 H, *J* = 6.0 Hz), 4.06 (s, C*H$_3$*-N, 3 H), 4.02 (t, CH$_2$-C*H$_2$*-O, 2 H, *J* = 6.8 Hz), 3.04 (t, CO-C*H$_2$*-CH$_2$, 2 H, *J* = 6.0 Hz), 1.57 (m, C*H$_2$*-CH$_2$-O, 2 H), 1.25 (m, CH$_3$-(C*H$_2$*)$_8$, 16 H), 0.85 (t, C*H$_3$*-CH$_2$, 3 H, *J* = 6.8 Hz). $^{13}$C-NMR (CDCl$_3$, 100 MHz) δ (ppm): 170.6 (C=O), 137.3 (N-*C*H-N), 123.4 (N-*C*H-CH-N), 123.2 (N-CH-*C*H-N), 65.7 (CH$_2$-*C*H$_2$-O), 45.6 (CH$_2$-*C*H$_2$-N), 37.3 (*C*H$_3$-N), 34.8 (CO-*C*H$_2$-CH$_2$), 31.9 (*C*H$_2$-CH$_2$-O), 30 – 22 (CH$_3$-(*C*H$_2$)$_8$), 14.1 (*C*H$_3$-CH$_2$). HRMS (ESI), m/z calculated for C$_{18}$H$_{33}$N$_2$O$_2$ [C$_{11:0}$E$_{(2)}$ImMe]$^+$: 309.25365, found 309.25296, m/z calculated for I$^-$: 126.90502, found 126.90469.
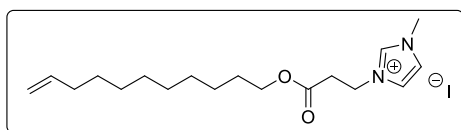
 [C$_{11:1}$E$_{(2)}$ImMe]I *1-undec-10-enylpropionate-3-imidazolium iodide.* 95% yield. $^1$H-NMR (CDCl$_3$, 400 MHz) δ (ppm): 9.88 (s, N-C*H*-N, 1 H), 7.64 (s, N-CH-C*H*-N, 1 H), 7.48 (s, N-C*H*-CH-N, 1 H), 5.78 (m, CH2=C*H*, 1 H), 4.94 (d, C*H$_2$*=CH, 1 H, *J* = 17.2 Hz), 4.89 (d, C*H$_2$*=CH, 1 H, *J* = 10.0 Hz), 4.66 (t, CH$_2$-C*H$_2$*-N, 2 H, *J* = 6.0 Hz), 4.08 (s, C*H$_3$*-N, 3 H), 4.04 (t, CH$_2$-C*H$_2$*-O, 2 H, *J* = 6.8 Hz), 3.06 (t, CO-C*H$_2$*-CH$_2$, 2 H, *J* = 6.4 Hz), 1.99 (m, CH$_2$=CH-C*H$_2$*, 2 H) 1.56 (m, C*H$_2$*-CH$_2$-O, 2 H), 1.3-1.1 (m, (C*H$_2$*)$_6$, 12 H). $^{13}$C-NMR (CDCl$_3$, 100 MHz) δ (ppm): 170.6 (C=O), 139.2 (CH$_2$=*C*H), 137.4 (N-*C*H-N), 123.3 (N-CH-*C*H-N), 123.3 (N-*C*H-CH-N), 114.2 (*C*H$_2$=CH), 65.8 (CH$_2$-*C*H$_2$-O), 45.6 (CH$_2$-*C*H$_2$-N), 37.3 (*C*H$_3$-N), 34.8 (CO-*C*H$_2$-CH$_2$), 33.8 (*C*H$_2$-CH$_2$-O), 30 – 25 ((*C*H$_2$)$_7$). HRMS (ESI), m/z calculated for C$_{18}$H$_{31}$N$_2$O$_2$ [C$_{11:1}$E$_{(2)}$ImMe]$^+$: 307.23800, found 307.23728, m/z calculated for I$^-$: 126.90502, found 126.90473.
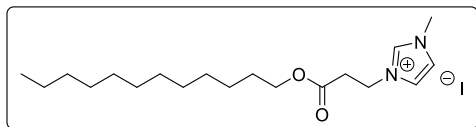
 [C$_{12:0}$E$_{(2)}$ImMe]I    *1-dodecanylpropionate-3-methylimidazolium iodide.* 99% yield. $^1$H-NMR (CDCl$_3$, 400 MHz) δ (ppm): 9.93 (s, N-C*H*-N, 1 H), 7.63 (s, N-CH-C*H*-N, 1 H), 7.44 (s, N-C*H*-CH-N, 1 H), 4.67 (t, CH$_2$-C*H$_2$*-N, 2 H, *J* = 6.0 Hz), 4.08 (s, C*H$_3$*-N, 3 H),  4.05 (t, CH$_2$-C*H$_2$*-O, 2 H, *J* = 6.8 Hz), 3.07 (t, CO-C*H$_2$*-CH$_2$, 2 H, *J* = 6.0 Hz), 1.60 (m, C*H$_2$*-CH$_2$-O, 2 H), 1.3-1.1 (m, CH$_3$-(C*H$_2$*)$_9$, 16 H), 0.87 (t, C*H$_3$*-CH$_2$, 3 H, *J* = 6.8 Hz).  $^{13}$C-NMR (CDCl$_3$, 100 MHz) δ (ppm): 170.7 (C=O), 137.5 (N-*C*H-N), 123.3 (N-*C*H-CH-N), 123.2 (N-CH-*C*H-N), 65.8 (CH$_2$-*C*H$_2$-O), 45.7 (CH$_2$-*C*H$_2$-N), 37.3 (*C*H$_3$-N), 34.9 (CO-*C*H$_2$-CH$_2$), 32.0 (*C*H$_2$-CH$_2$-O), 30 − 22 (CH$_3$-(*C*H$_2$)$_9$), 14.2 (*C*H$_3$-CH$_2$). HRMS (ESI), m/z calculated for C$_{19}$H$_{35}$N$_2$O$_2$ [C$_{12:0}$E$_{(2)}$ImMe]$^+$: 323.26930, found 323.26876,  m/z calculated for I$^-$: 126.90502, found 126.90469.
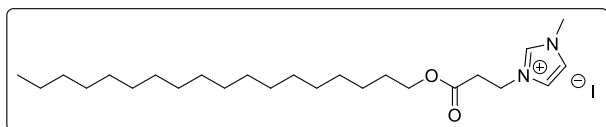
 [C$_{18:0}$E$_{(2)}$ImMe]I        *1-octadecanylpropionate-3-methylimidazolium iodide.* 99% yield. $^1$H-NMR (CDCl$_3$, 400 MHz) δ (ppm): 9.76 (s, N-C*H*-N, 1 H), 7.65 (s, N-CH-C*H*-N, 1 H), 7.53 (s, N-C*H*-CH-N, 1 H), 4.63 (t, CH$_2$-C*H$_2$*-N, 2 H, *J* = 6.0 Hz), 4.04 (s, C*H$_3$*-N, 3 H),  4.00 (t, CH$_2$-C*H$_2$*-O, 2 H, *J* = 6.8 Hz), 3.02 (t, CO-C*H$_2$*-CH$_2$, 2 H, *J* = 6.0 Hz), 1.55 (m, C*H$_2$*-CH$_2$-O, 2 H), 1.3-1.1 (m, CH$_3$-(C*H$_2$*)$_{15}$, 30 H), 0.82 (t, C*H$_3$*-CH$_2$, 3 H, *J* = 6.8 Hz).  $^{13}$C-NMR (CDCl$_3$, 100 MHz) δ (ppm): 170.5 (C=O), 137.2 (N-*C*H-N), 123.4 (N-*C*H-CH-N), 123.2 (N-CH-*C*H-N), 65.7 (CH$_2$-*C*H$_2$-O), 45.5 (CH$_2$-*C*H$_2$-N), 37.2 (*C*H$_3$-N), 34.7 (CO-*C*H$_2$-CH$_2$), 31.8 (*C*H$_2$-CH$_2$-O), 30 − 22 (CH$_3$-(CH$_2$)$_{15}$), 14.1 (*C*H$_3$-CH$_2$). HRMS (ESI), m/z calculated for C$_{25}$H$_{47}$N$_2$O$_2$ [C$_{18:0}$E$_{(2)}$ImMe]$^+$: 407.36321, found 407.36260,  m/z calculated for I$^-$: 126.90502, found 126.90472.
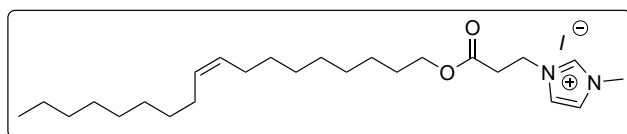
 [C$_{18:1}$E$_{(2)}$ImMe]I        *1-octadec-9-enylpropionate-3-methylimidazolium iodide.* 97% yield. $^1$H-NMR (CDCl$_3$, 400 MHz) δ (ppm): 9.88 (s, N-C*H*-N, 1 H), 7.58 (s, N-CH-C*H*-N, 1 H), 7.41 (s, N-C*H*-CH-N, 1 H), 5.27 (m, C*H*=C*H*, 2 H), 4.61 (t, CH$_2$-C*H$_2$*-N, 2 H, *J* = 6.0 Hz), 4.01 (s, C*H$_3$*-N, 3 H),  3.99 (t, CH$_2$-C*H$_2$*-O, 2 H, *J* = 6.8 Hz), 3.00 (t, CO-C*H$_2$*-CH$_2$, 2 H, *J* = 6.0 Hz), 1.94 (m, C*H$_2$*-CH=CH, 4 H), 1.53 (m, C*H$_2$*-CH$_2$-O, 2 H), 1.3-1.1 (m, CH$_3$-(C*H$_2$*)$_{11}$, 22 H), 0.81 (t, C*H$_3$*-CH$_2$, 3 H, *J* = 6.8 Hz).  $^{13}$C-NMR (CDCl$_3$, 100 MHz) δ (ppm): 170.7 (C=O), 137.5 (N-*C*H-N), 130.0 (*C*H=CH), 129.7 (CH=*C*H), 123.3 (N-*C*H-CH-N x 2), 65.8 (CH$_2$-*C*H$_2$-O), 45.6 (CH$_2$-*C*H$_2$-N), 37.2 (*C*H$_3$-N), 34.8 (CO-*C*H$_2$-CH$_2$), 31.9 (*C*H$_2$-CH$_2$-O), 30 − 22 (CH$_3$-(CH$_2$)$_{13}$), 14.2 (*C*H$_3$-CH$_2$). HRMS (ESI), m/z calculated for C$_{25}$H$_{45}$N$_2$O$_2$ [C$_{18:1}$E$_{(2)}$ImMe]$^+$: 405.34756, found 405.34683,  m/z calculated for I$^-$: 126.90502, found 126.90474.

### 3.5. General procedure for the metathesis reaction between [$C_{x:y}E_{(2)}$ImMe]I and AgBF$_4$, synthesis of 1-alkylpropionate-3-methylimidazolium tetrafuoroborate, [$C_{x:y}E_{(2)}$ImMe]BF$_4$
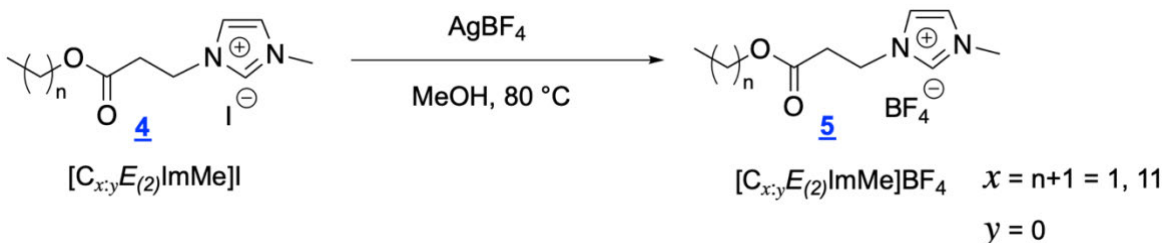


**Scheme S5**: Anion metathesis with silver tetrafluoroborate

A solution of AgBF$_4$ (1.5 mmol) in 2 mL of anhydrous MeOH was slowly added to a stirred solution of 1-alkylpropionate-3-methylimidazolium iodide in 2 mL of anhydrous MeOH, under inert atmosphere (N$_2$). The reaction mixture was heated at 70 °C for 15 hours. Finally, the reaction was allowed to cold down to room temperature and the AgI precipitated was filtered off over celite. The new ionic liquid was purified by recrystallization in MeOH at 0 °C.
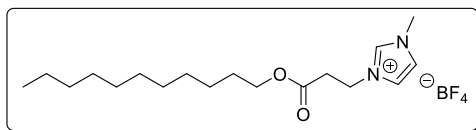
 [$C_{11:0}E_{(2)}$ImMe]BF$_4$ *1-undecanylpropionate-3-methylimidazolium tetrafuoroborate.* 89% yield. $^1$H-NMR (CDCl$_3$, 400 MHz) δ (ppm): 8.78 (s, N-C*H*-N, 1 H), 7.46 (s, N-CH-C*H*-N, 1 H), 7.29 (s, N-C*H*-CH-N, 1 H), 4.49 (t, CH$_2$-C*H$_2$*-N, 2 H, *J* = 6.0 Hz), 4.07 (t, CH$_2$-C*H$_2$*-O, 2 H, *J* = 6.8 Hz), 3.94 (s, C*H$_3$*-N, 3 H), 2.95 (t, CO-C*H$_2$*-CH$_2$, 2 H, *J* = 6.0 Hz), 1.60 (m, C*H$_2$*-CH$_2$-O, 2 H), 1.4-1.1 (m, CH$_3$-(C*H$_2$*)$_8$, 16 H), 0.89 (t, C*H$_3$*-CH$_2$, 3 H, *J* = 6.8 Hz). $^{13}$C-NMR (CDCl$_3$, 100 MHz) δ (ppm): 170.8 (C=O), 137.2 (N-*C*H-N), 123.3 (N-*C*H-CH-N), 123.0 (N-CH-*C*H-N), 65.6 (CH$_2$-*C*H$_2$-O), 45.4 (CH$_2$-*C*H$_2$-N), 36.5 (*C*H$_3$-N), 34.4 (CO-*C*H$_2$-CH$_2$), 32.0 (*C*H$_2$-CH$_2$-O), 30 − 22 (CH$_3$-(*C*H$_2$)$_8$), 14.2 (*C*H$_3$-CH$_2$). HRMS (ESI), m/z calculated for C$_{18}$H$_{33}$N$_2$O$_2$ [$C_{11:0}E_{(2)}$ImMe]$^+$: 309.25365, found 309.25294, m/z calculated for BF$_4^-$: 87.00347, found 87.00289.
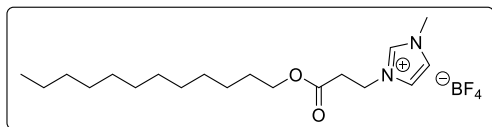
 [$C_{12:0}E_{(2)}$ImMe]BF$_4$ *1-dodecanylpropionate)-3-methylimidazolium tetrafuoroborate.* 91% yield. $^1$H-NMR (CDCl$_3$, 400 MHz) δ (ppm): 8.67 (s, N-C*H*-N, 1 H), 7.38 (s, N-CH-C*H*-N, 1 H), 7.24 (s, N-C*H*-CH-N, 1 H), 4.41 (t, CH$_2$-C*H$_2$*-N, 2 H, *J* = 6.0 Hz), 3.99 (t, CH$_2$-C*H$_2$*-O, 2 H, *J* = 6.8 Hz), 3.85 (s, C*H$_3$*-N, 3 H), 2.87 (t, CO-C*H$_2$*-CH$_2$, 2 H, *J* = 6.0 Hz), 1.53 (m, C*H$_2$*-CH$_2$-O, 2 H), 1.4-1.1 (m, CH$_3$-(C*H$_2$*)$_9$, 16 H), 0.81 (t, C*H$_3$*-CH$_2$, 3 H, *J* = 6.8 Hz). $^{13}$C-NMR (CDCl$_3$, 100 MHz) δ (ppm): 170.8 (C=O), 137.0 (N-*C*H-N), 123.3 (N-*C*H-CH-N), 122.9 (N-CH-*C*H-N), 65.6 (CH$_2$-*C*H$_2$-O), 45.2 (CH$_2$-*C*H$_2$-N), 36.4 (*C*H$_3$-N), 34.3 (CO-*C*H$_2$-CH$_2$), 32.0 (*C*H$_2$-CH$_2$-O), 30 − 22 (CH$_3$-(*C*H$_2$)$_9$), 14.2 (*C*H$_3$-CH$_2$). HRMS (ESI), m/z calculated for C$_{19}$H$_{35}$N$_2$O$_2$ [$C_{12:0}E_{(2)}$ImMe]$^+$: 323.26930, found 323.26869, m/z calculated for BF$_4^-$: 87.00347, found 87.00286

# 4. $^1$H and $^{13}$C NMR spectra of synthetized products
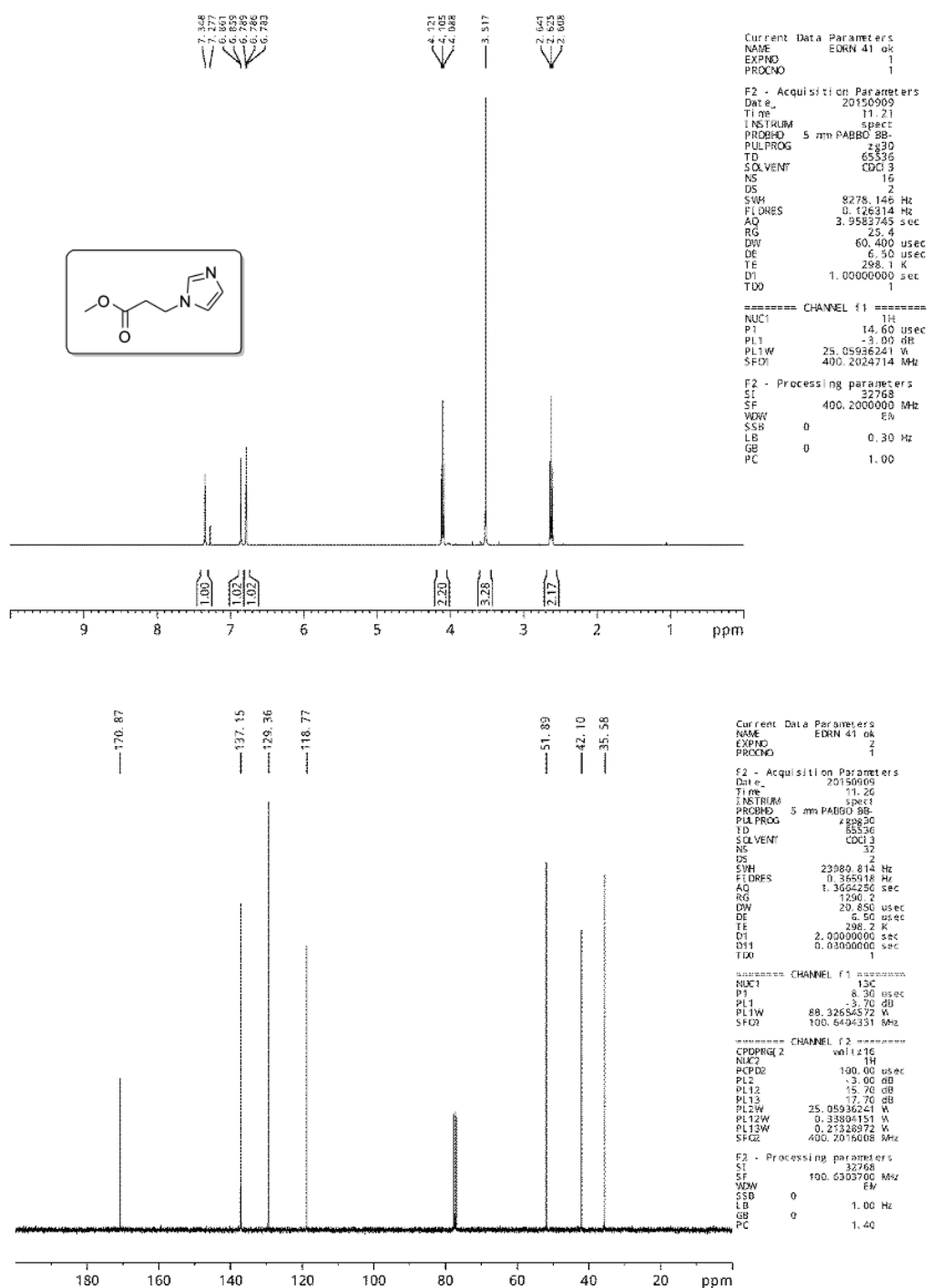


**Figure S1**: $^1$H NMR spectrum (up) and $^{13}$C NMR spectrum (down) in CDCl$_3$ of C$_{1:0}$E$_{(2)}$Im
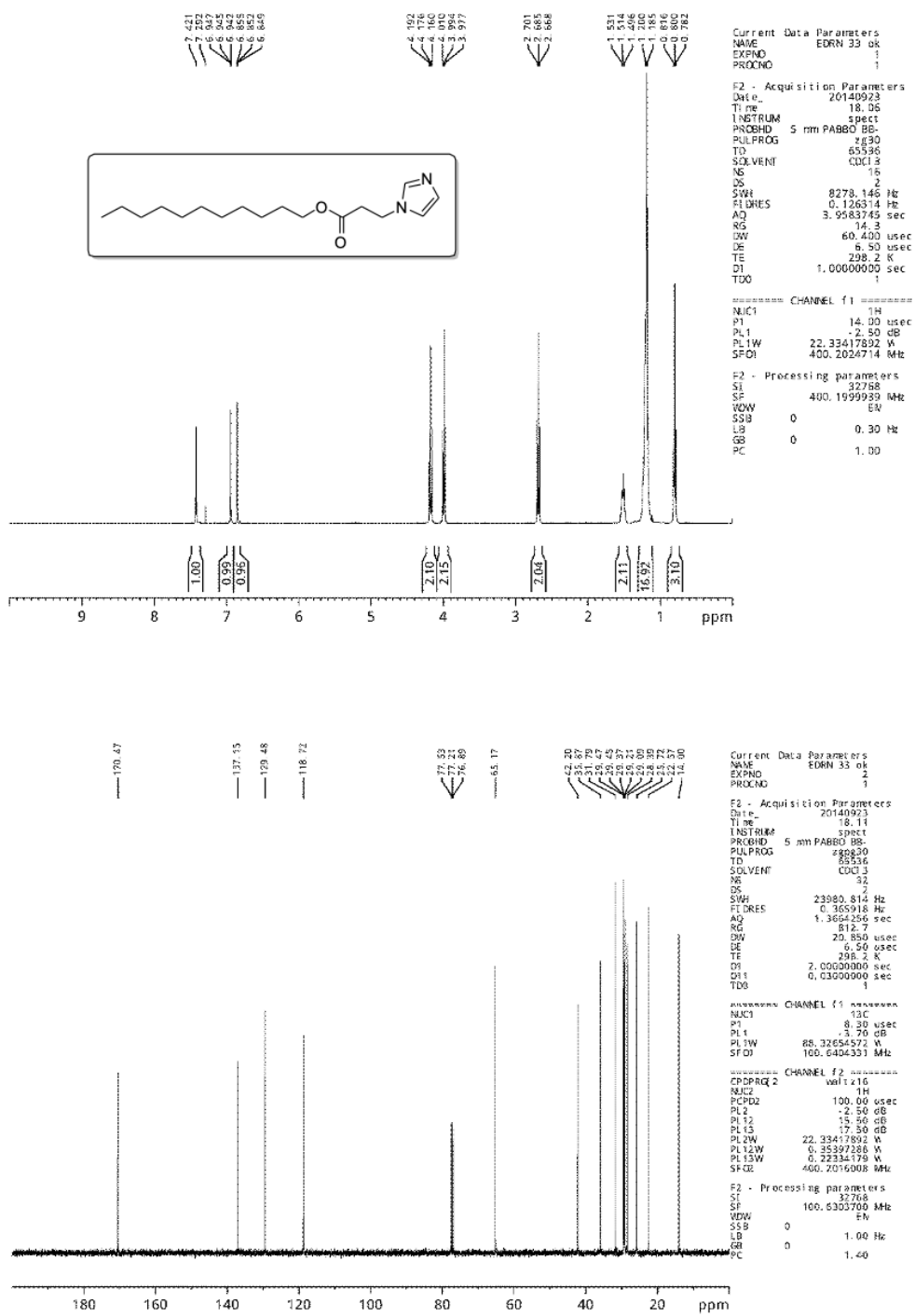
**Figure S2**: $^{1}$H NMR spectrum (up) and $^{13}$C NMR spectrum (down) in CDCl$_3$ of C$_{11:0}$*E$_{(2)}$*Im
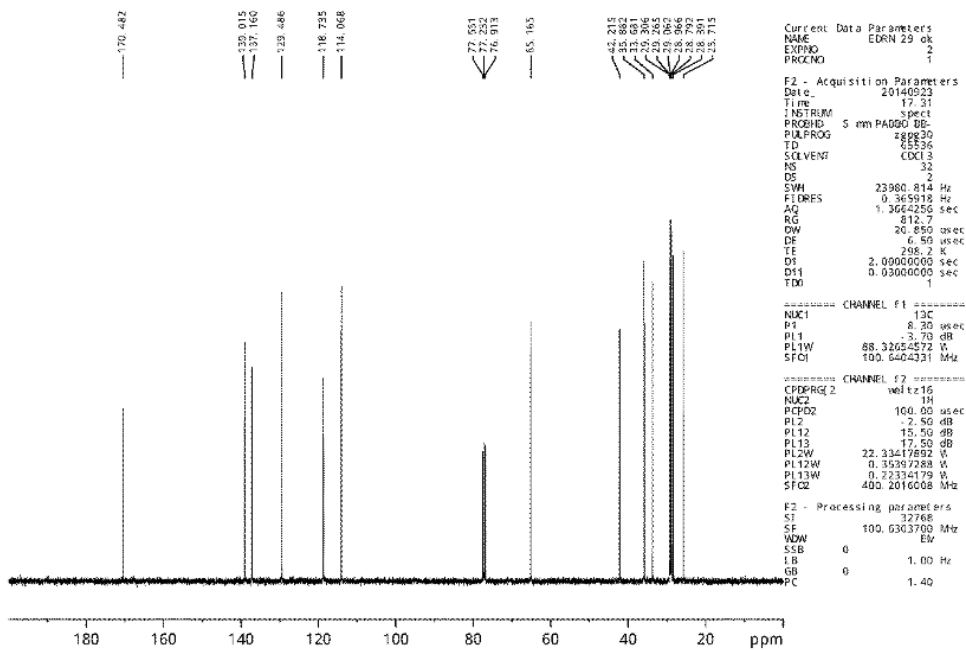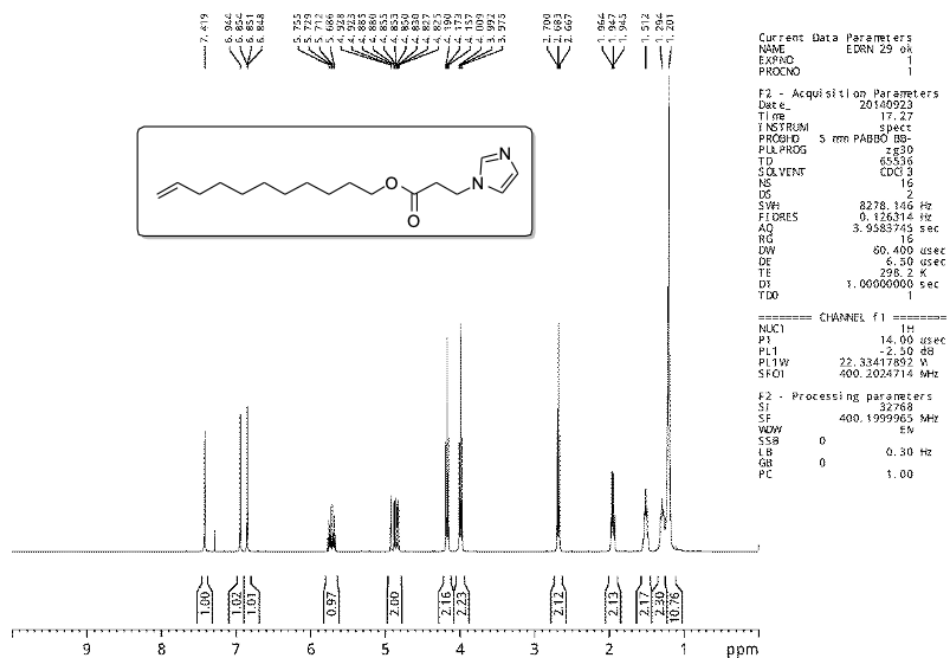
**Figure S3**: $^1$H NMR spectrum (up) and $^{13}$C NMR spectrum (down) in CDCl$_3$ of C$_{11:1}$$E_{(2)}$Im

**Figure S4**: $^1$H NMR spectrum (up) and $^{13}$C NMR spectrum (down) in CDCl$_3$ of C$_{12:0}$$E_{(2)}$Im
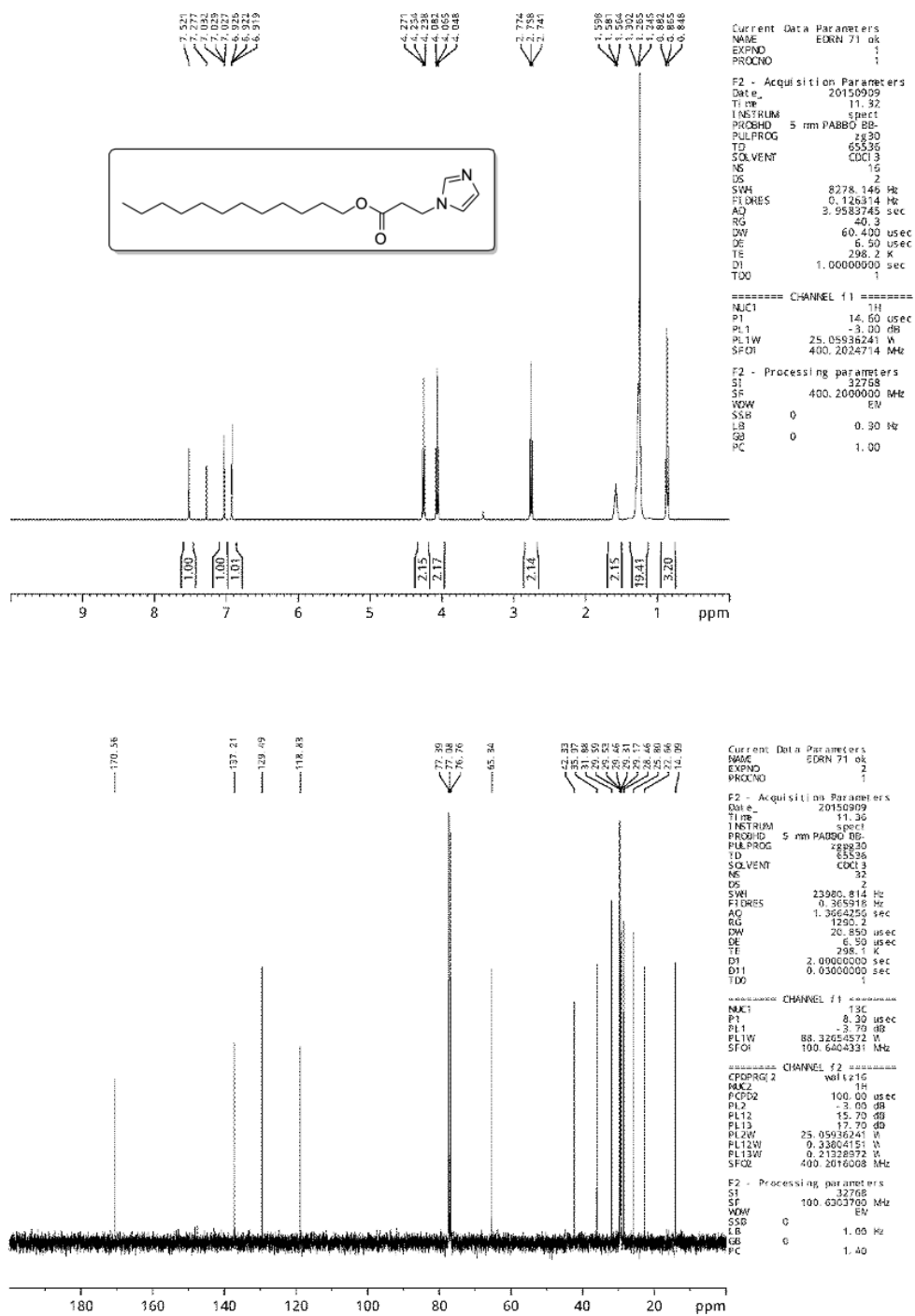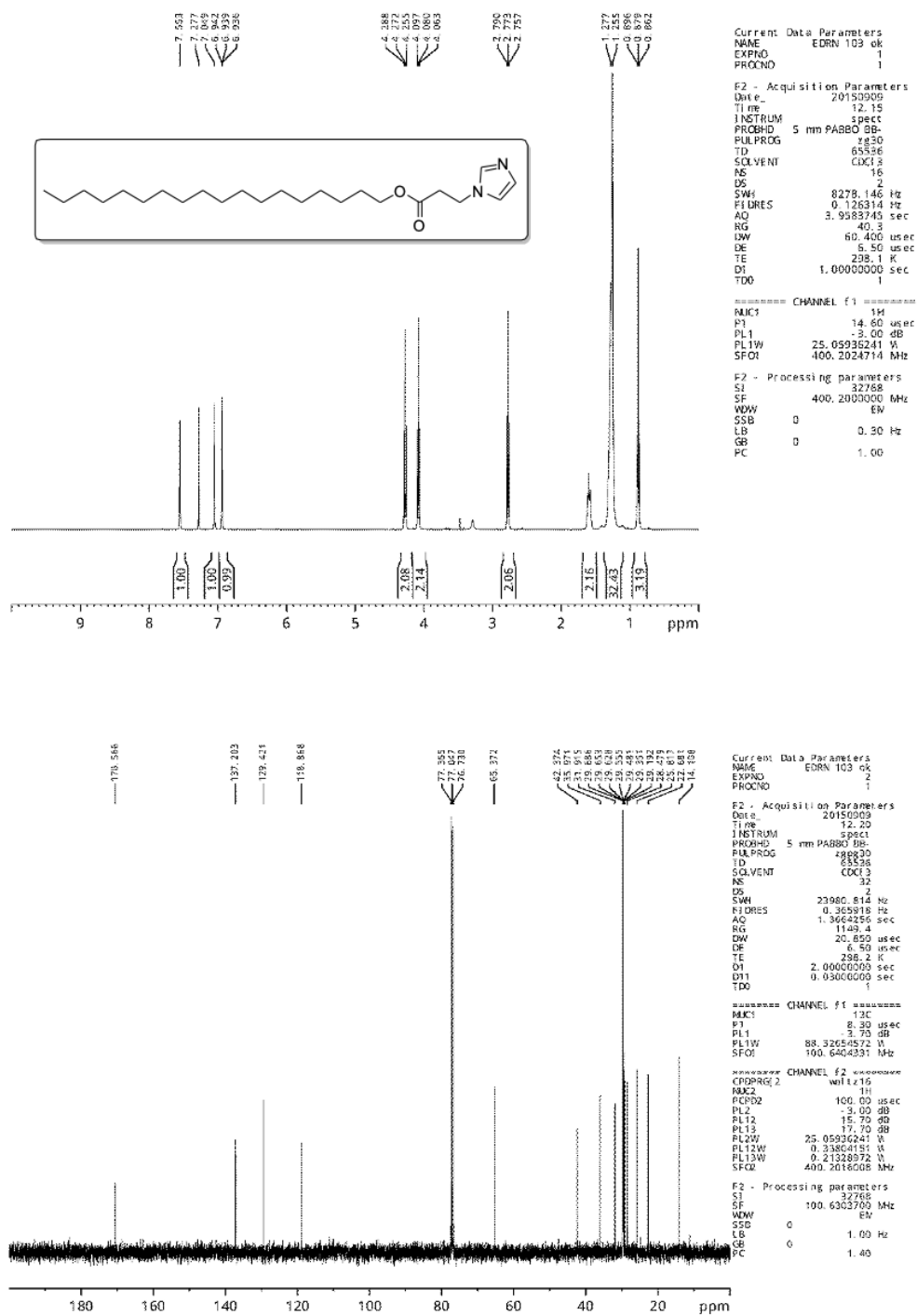
**Figure S5**: $^1$H NMR spectrum (up) and $^{13}$C NMR spectrum (down) in CDCl$_3$ of C$_{18:0}$$E_{(2)}$Im

**Figure S6**: $^1$H NMR spectrum (up) and $^{13}$C NMR spectrum (down) in CDCl$_3$ of C$_{18:1}$$E_{(2)}$Im
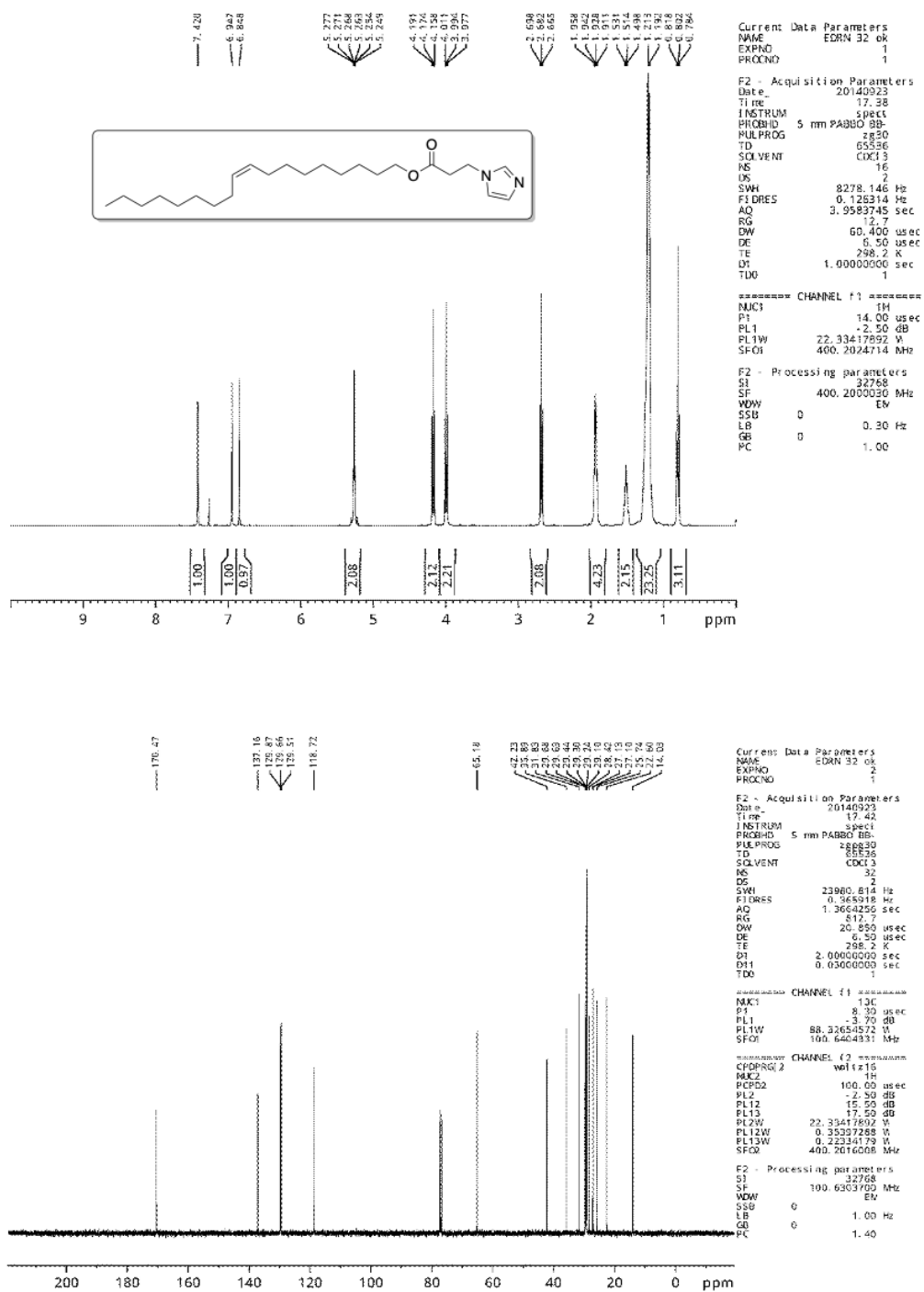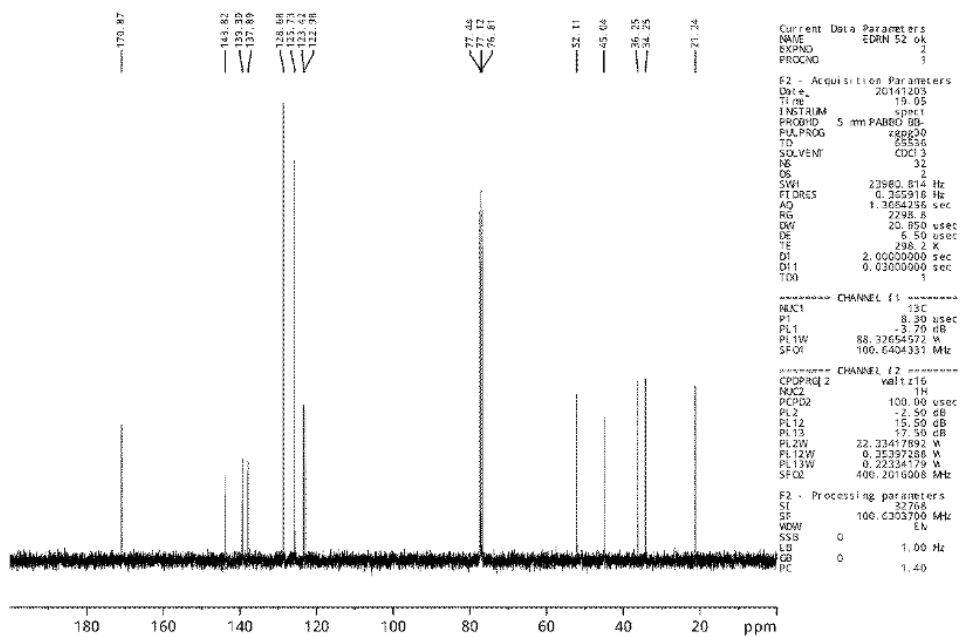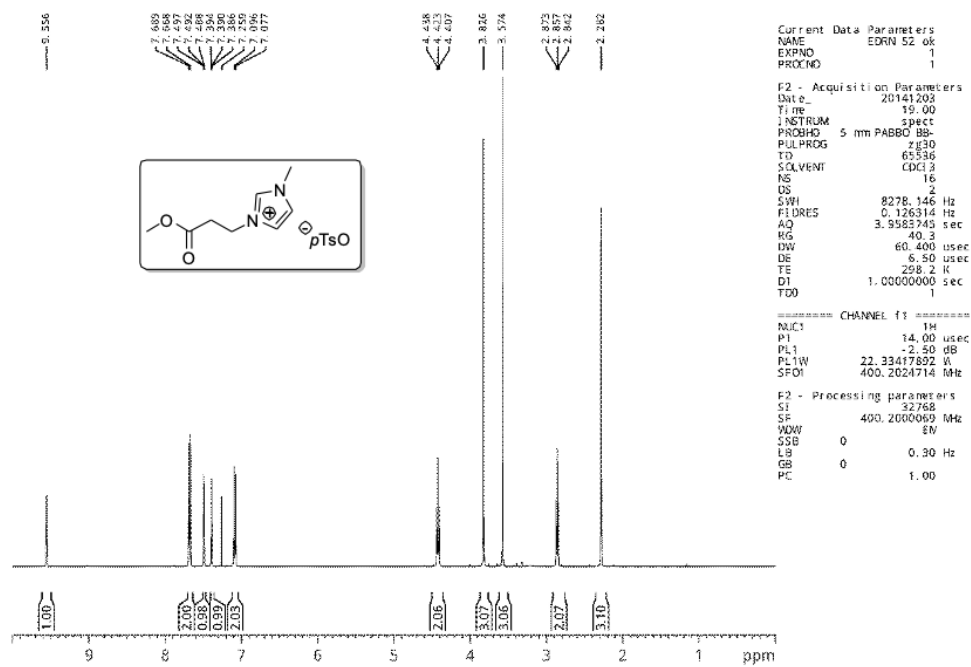
**Figure S7**: $^1$H NMR spectrum (up) and $^{13}$C NMR spectrum (down) in CDCl$_3$ of [C$_{1:0}$E$_{(2)}$Im]$p$TsO
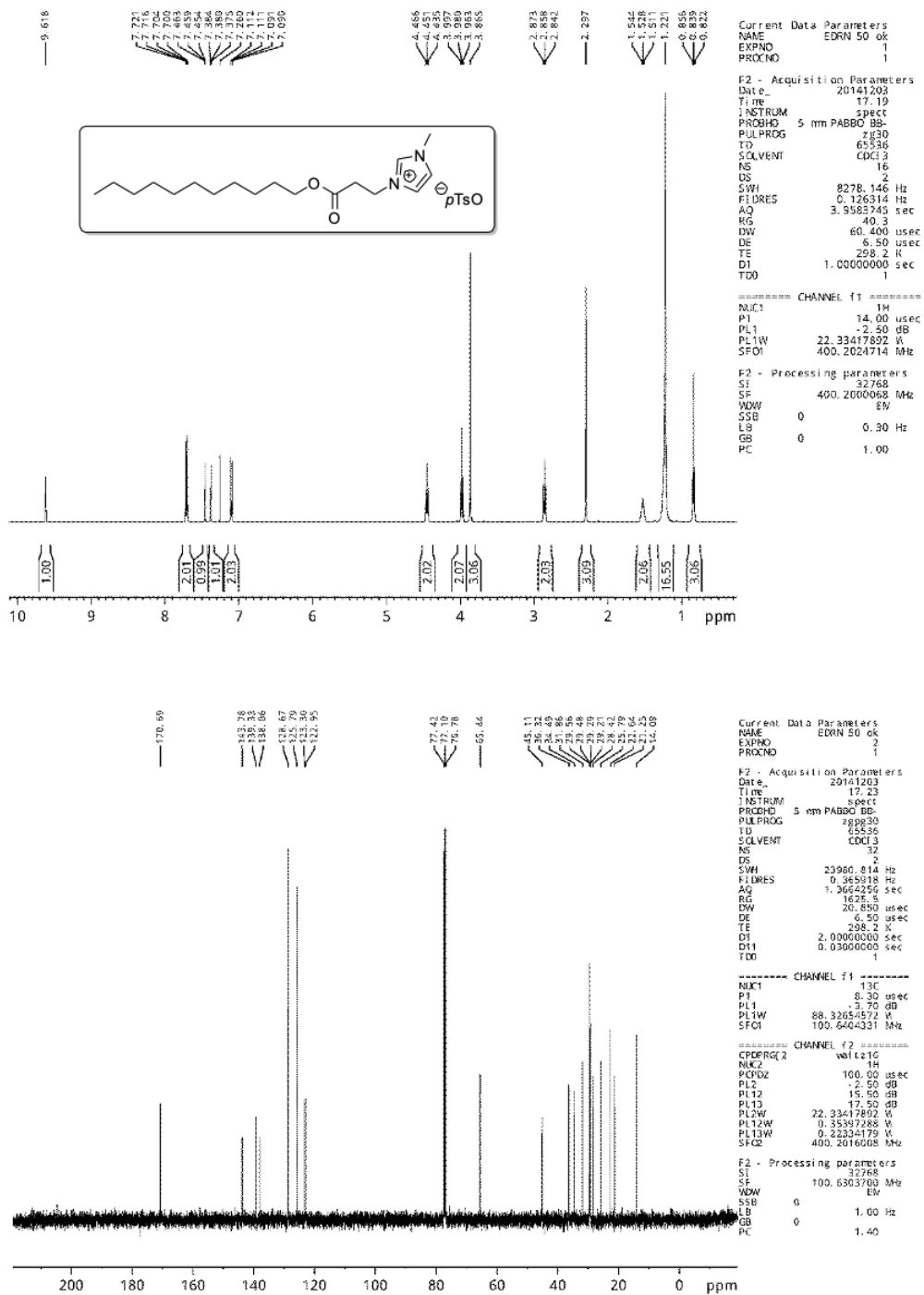
**Figure S8**: $^1$H NMR spectrum (up) and $^{13}$C NMR spectrum (down) in CDCl$_3$ of [C$_{11:0}$$E_{(2)}$Im]$p$TsO

**Figure S9**: $^1H$ NMR spectrum (up) and $^{13}C$ NMR spectrum (down) in $CDCl_3$ of $[C_{11:1}E_{(2)}Im]pTsO$

**Figure S10**: $^1$H NMR spectrum (up) and $^{13}$C NMR spectrum (down) in CDCl$_3$ of [C$_{12:0}$$E_{(2)}$Im]$p$TsO
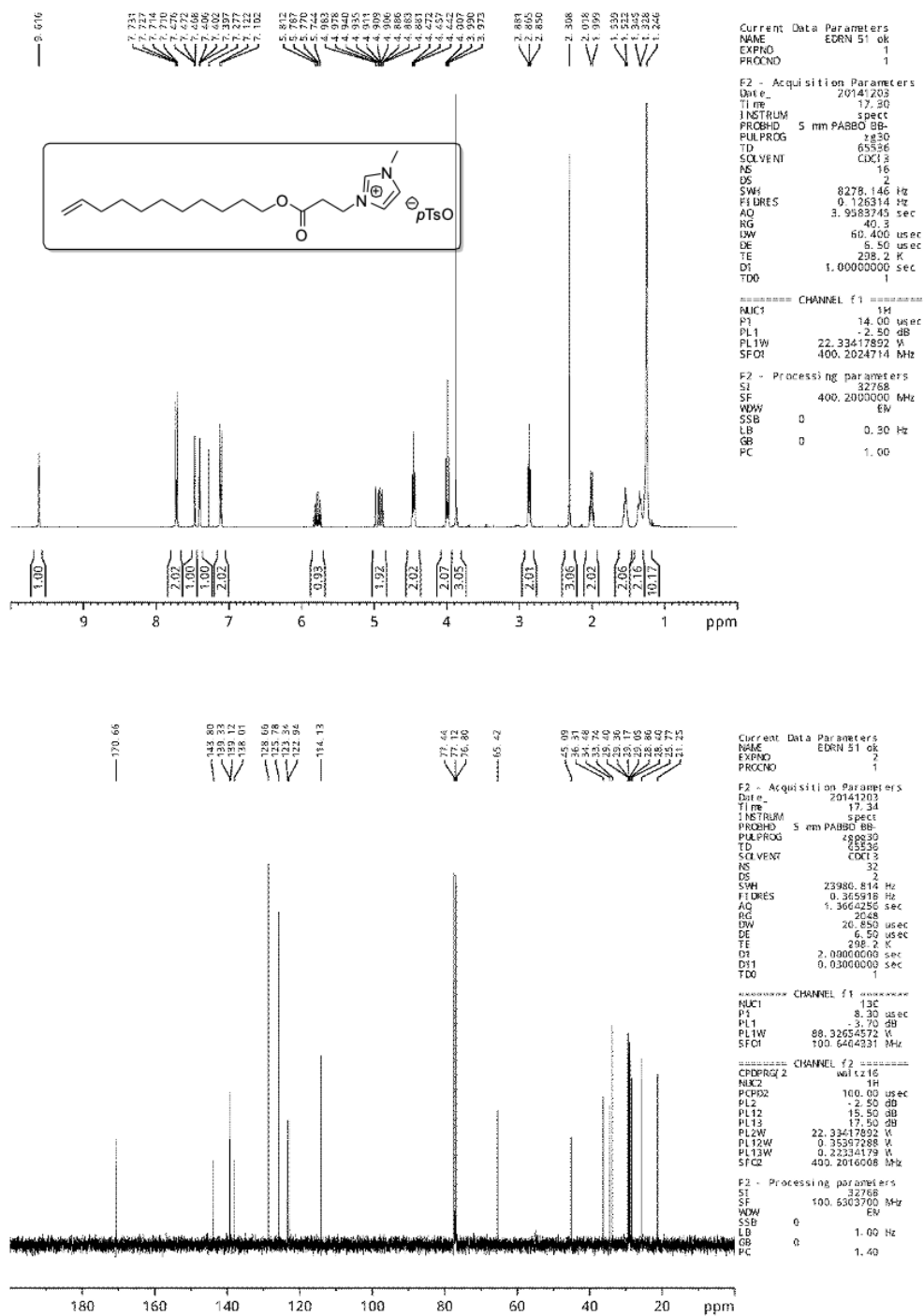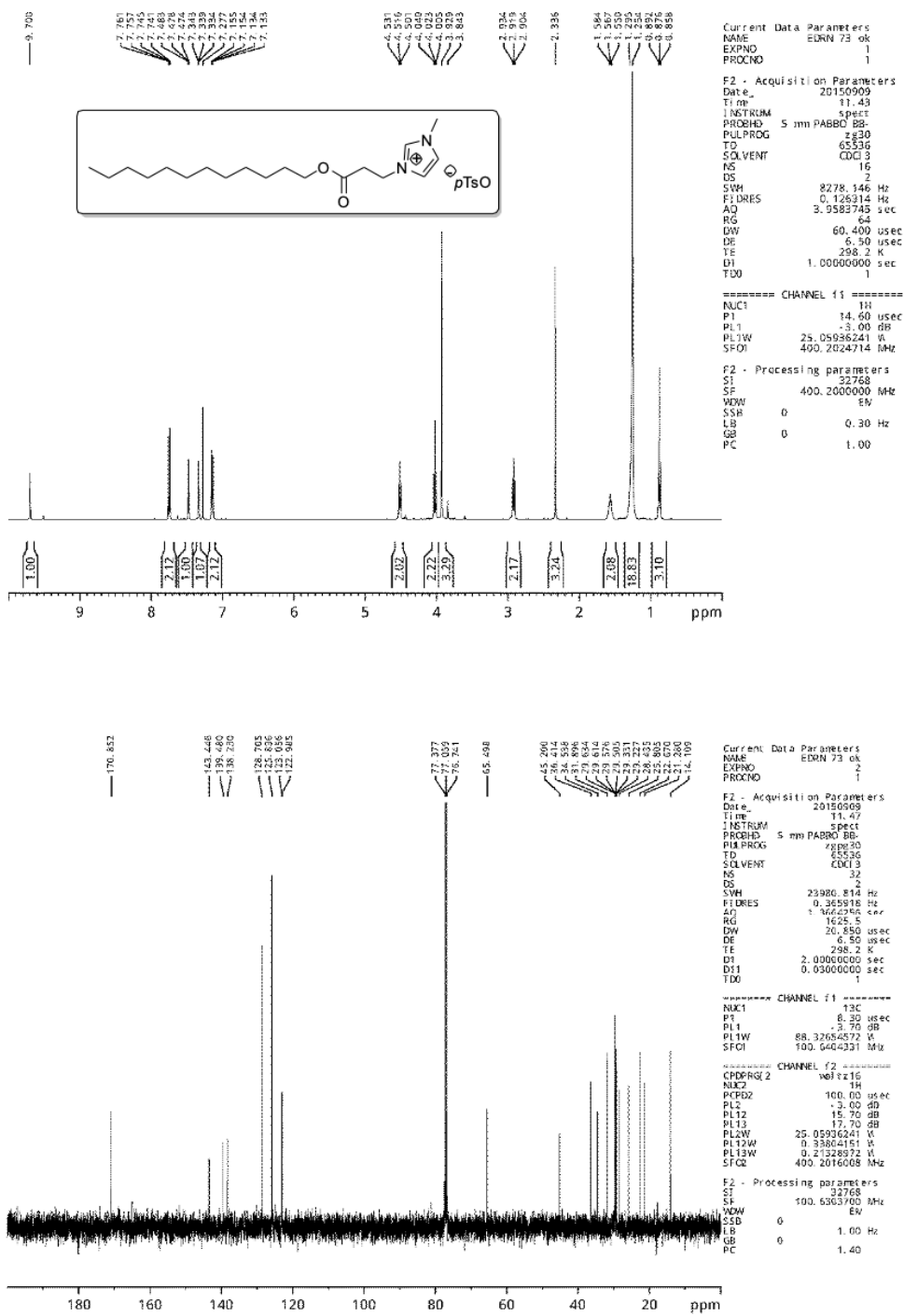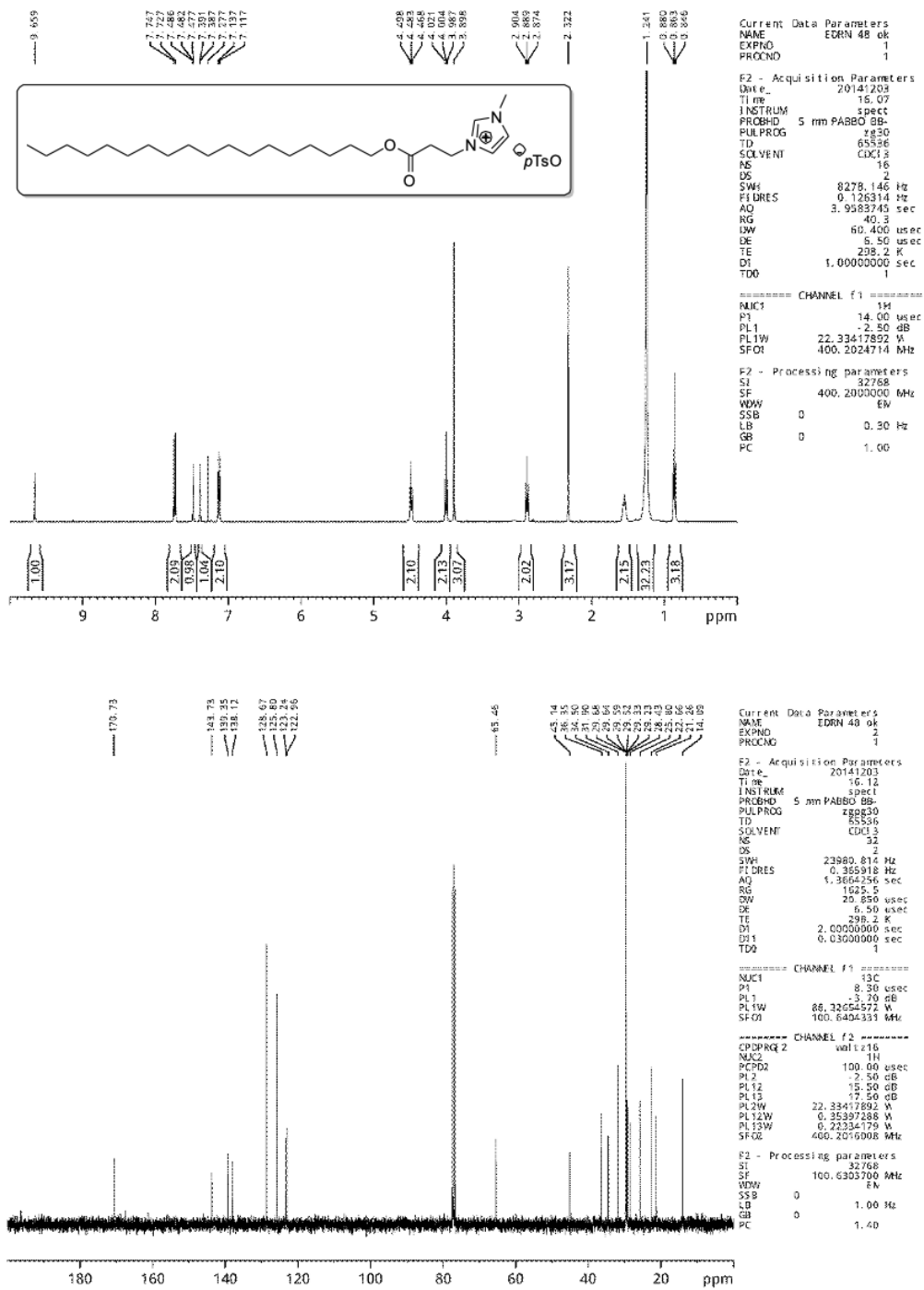
**Figure S11**: $^1H$ NMR spectrum (up) and $^{13}C$ NMR spectrum (down) in CDCl$_3$ of [C$_{18:0}$E$_{(2)}$Im]$p$TsO
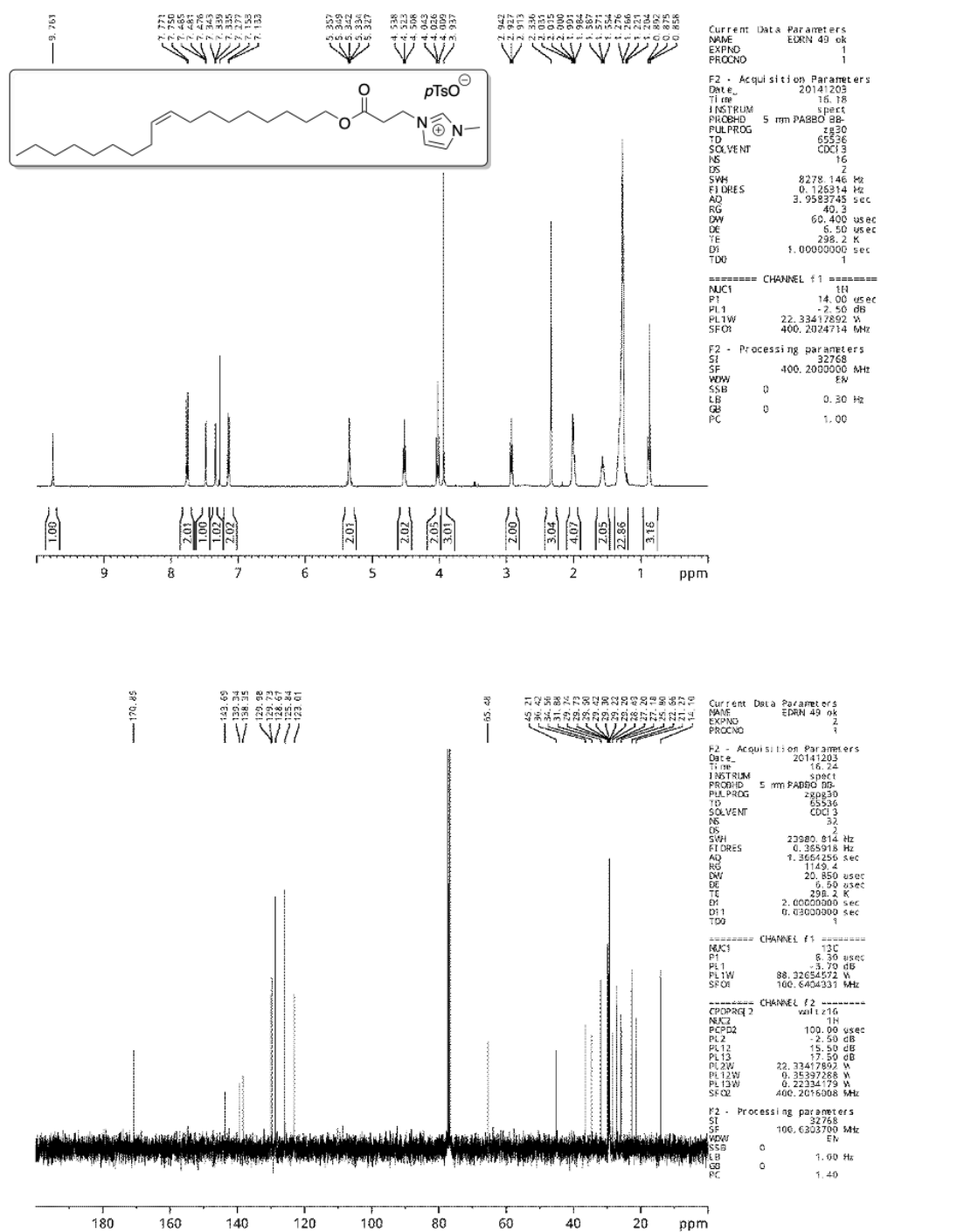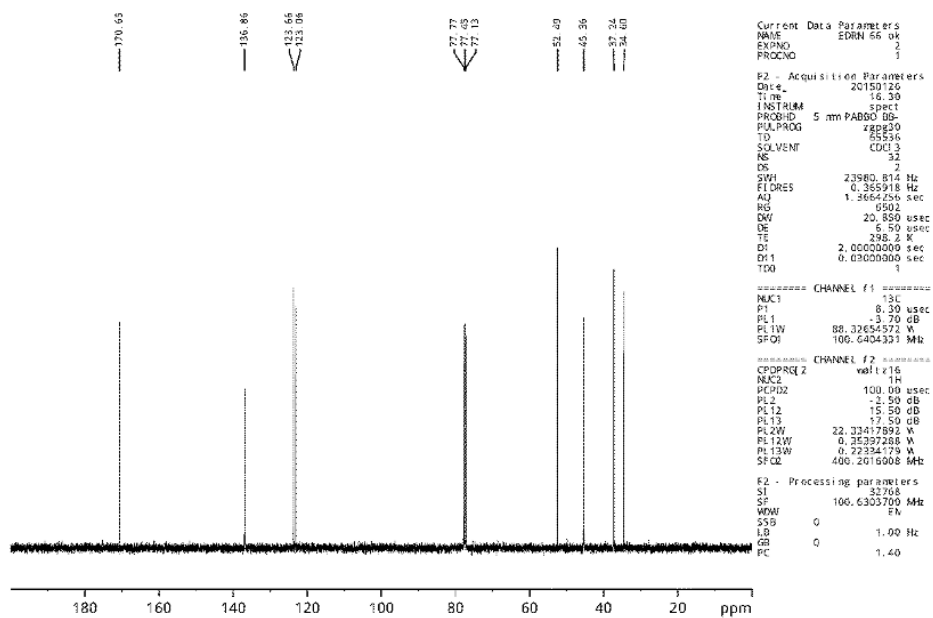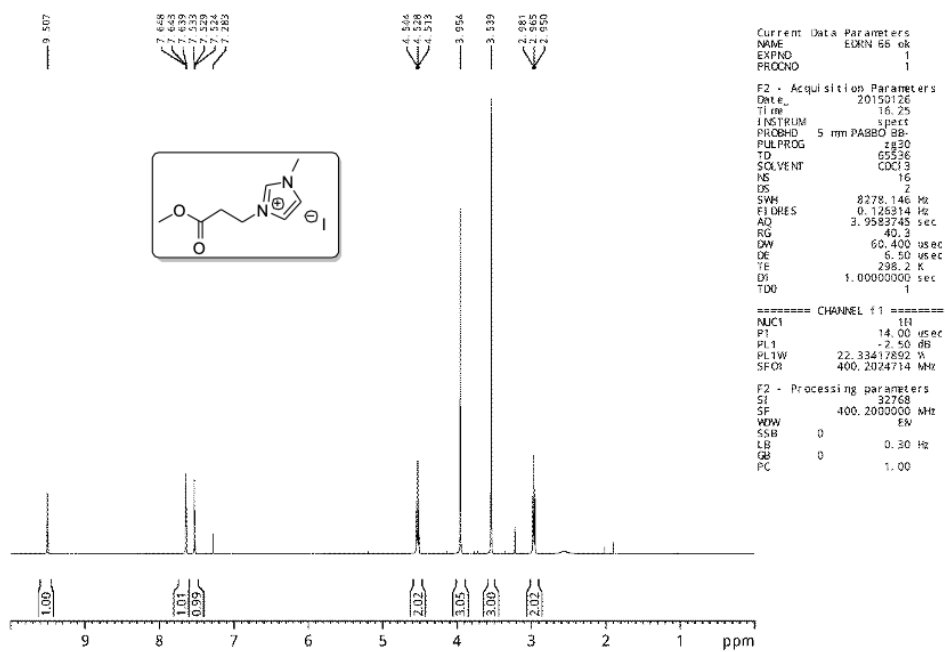
**Figure S12**: $^1$H NMR spectrum (up) and $^{13}$C NMR spectrum (down) in CDCl$_3$ of [C$_{18:1}$$E_{(2)}$Im]$p$TsO

**Figure S13**: $^1$H NMR spectrum (up) and $^{13}$C NMR spectrum (down) in CDCl$_3$ of [C$_{1:0}$*E$_{(2)}$*Im]I

**Figure S14**: $^1$H NMR spectrum (up) and $^{13}$C NMR spectrum (down) in CDCl$_3$ of [C$_{11:0}$E$_{(2)}$Im]I

**Figure S15**: $^1$H NMR spectrum (up) and $^{13}$C NMR spectrum (down) in CDCl$_3$ of [C$_{11:1}$$E_{(2)}$Im]I
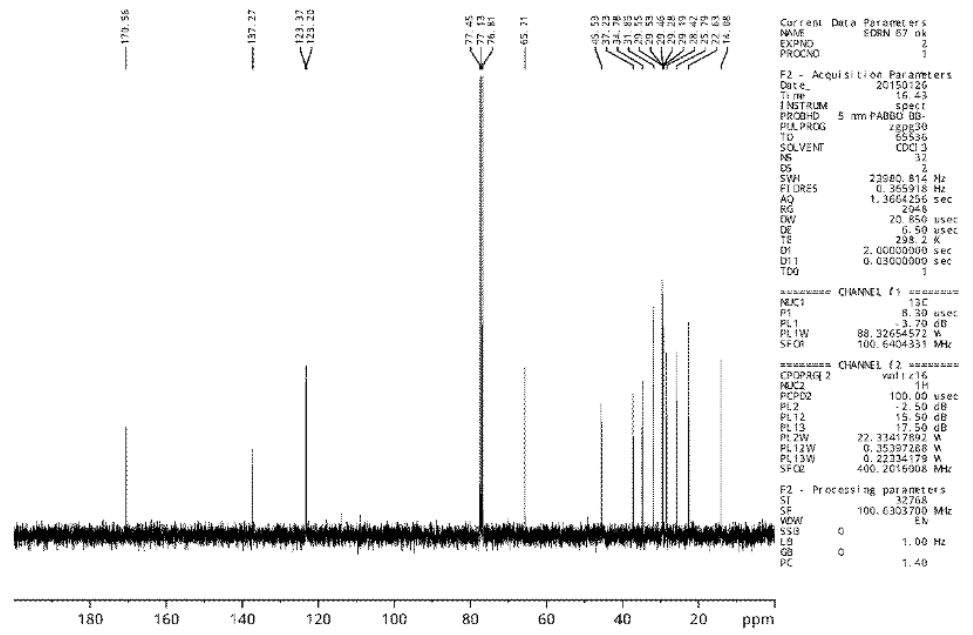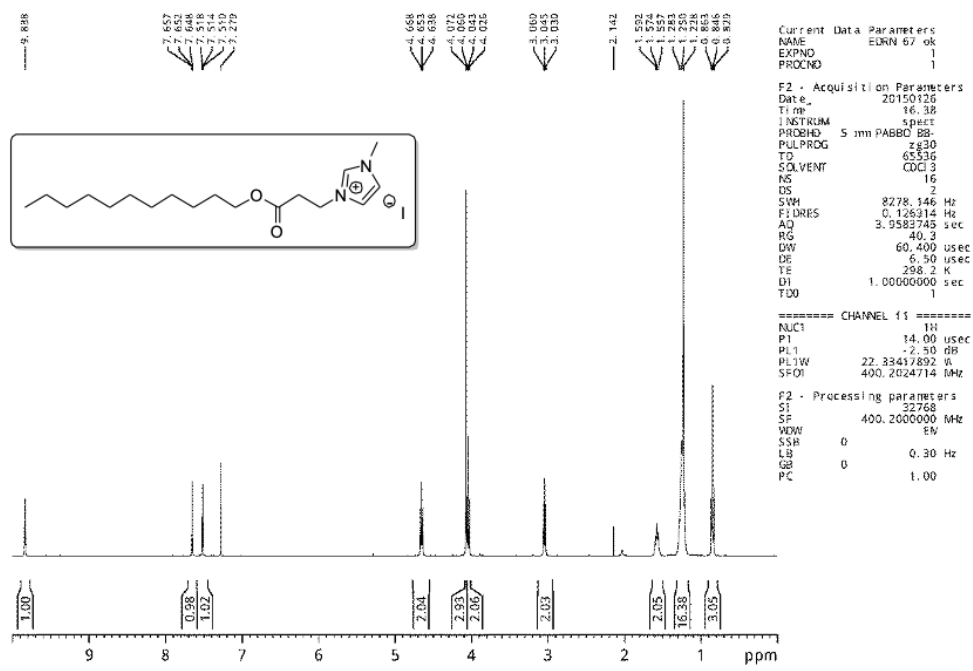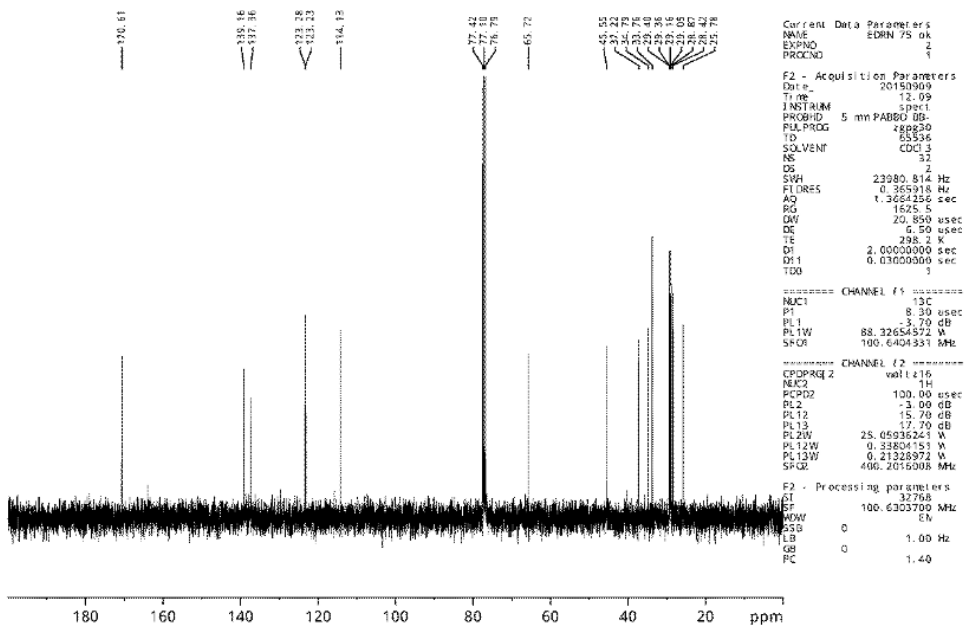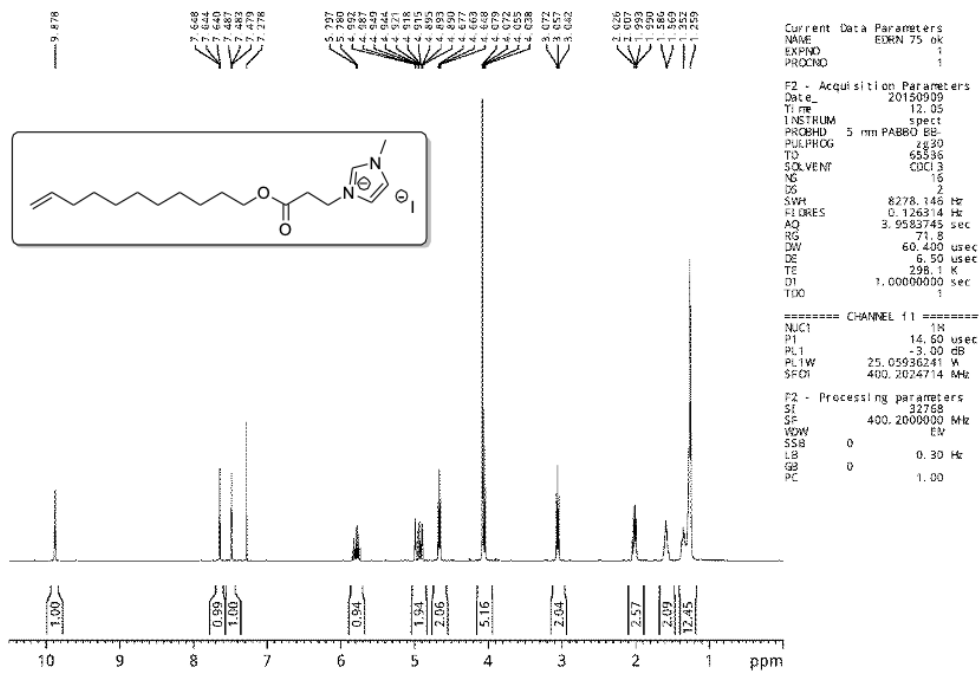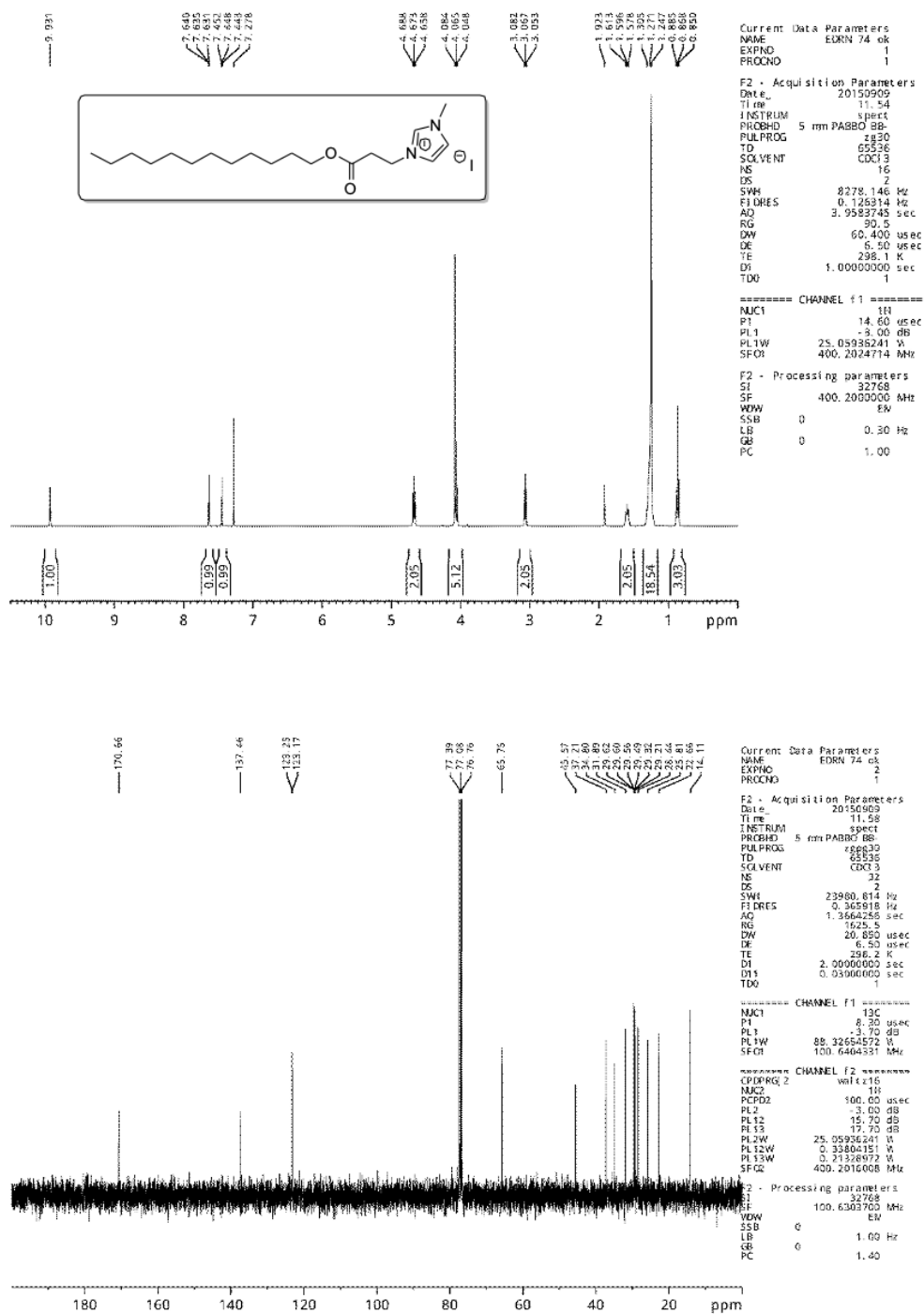
**Figure S16**: $^1H$ NMR spectrum (up) and $^{13}C$ NMR spectrum (down) in $CDCl_3$ of $[C_{12:0}E_{(2)}Im]I$
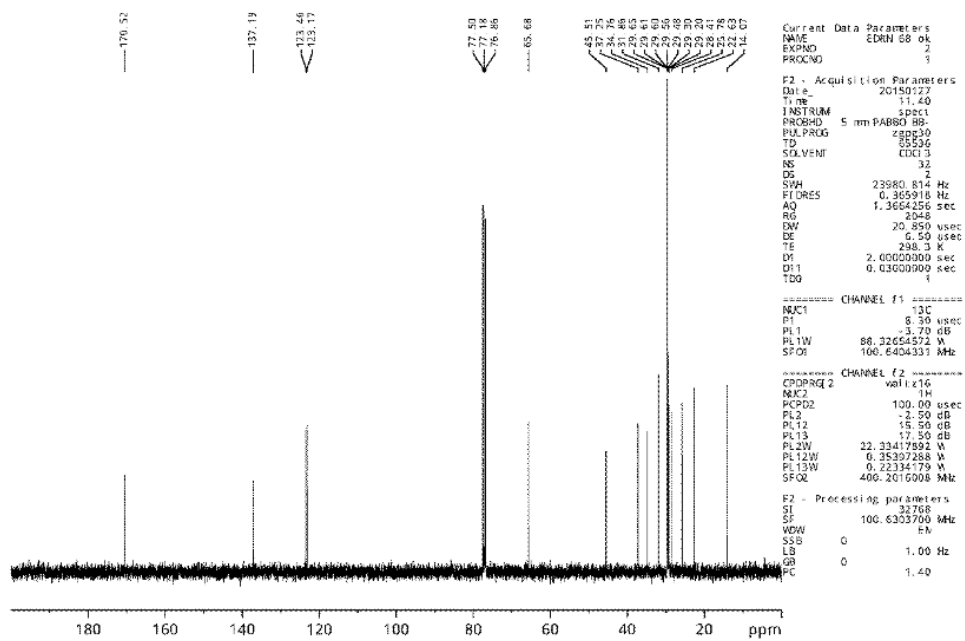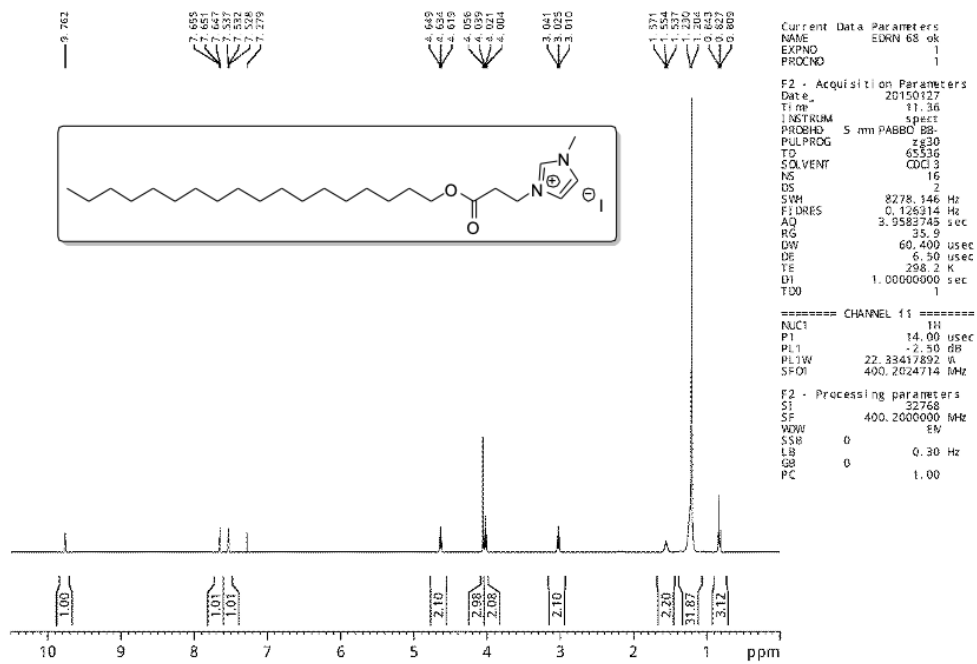
**Figure S17**: $^1H$ NMR spectrum (up) and $^{13}C$ NMR spectrum (down) in CDCl$_3$ of [C$_{18:0}$$E_{(2)}$Im]I

**Figure S18**: $^1$H NMR spectrum (up) and $^{13}$C NMR spectrum (down) in CDCl$_3$ of [C$_{18:1}$$E_{(2)}$Im]I
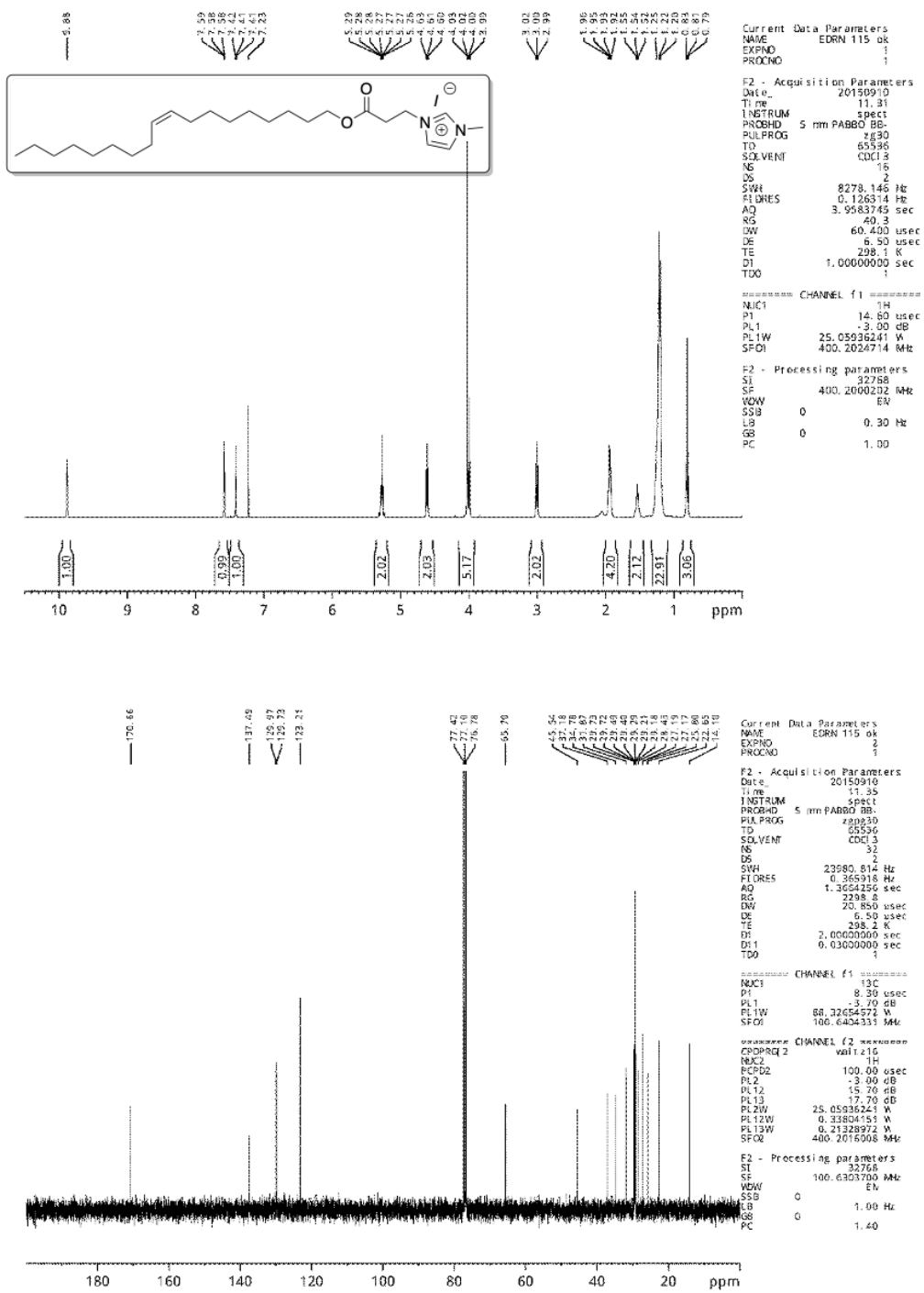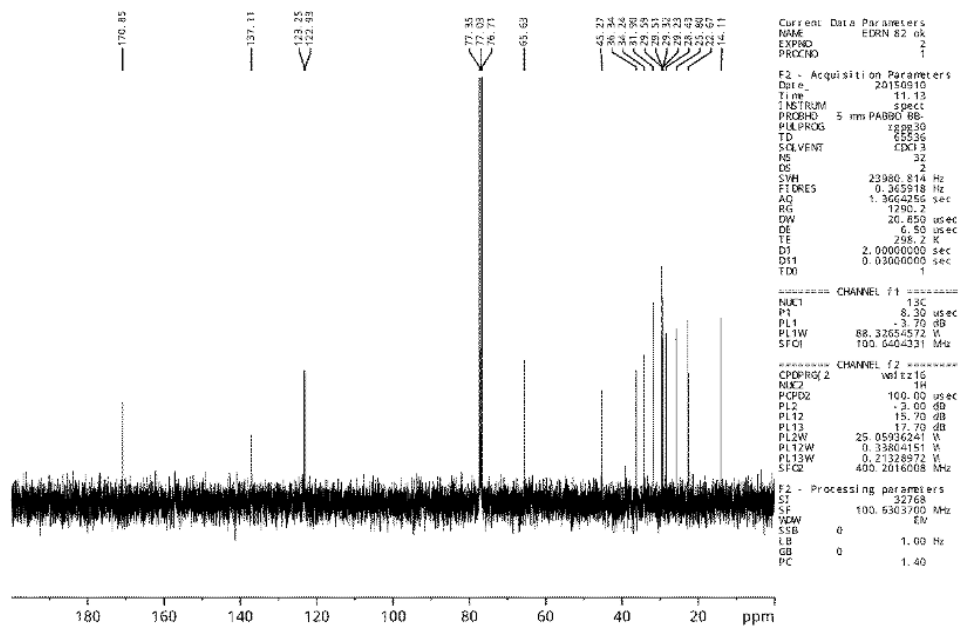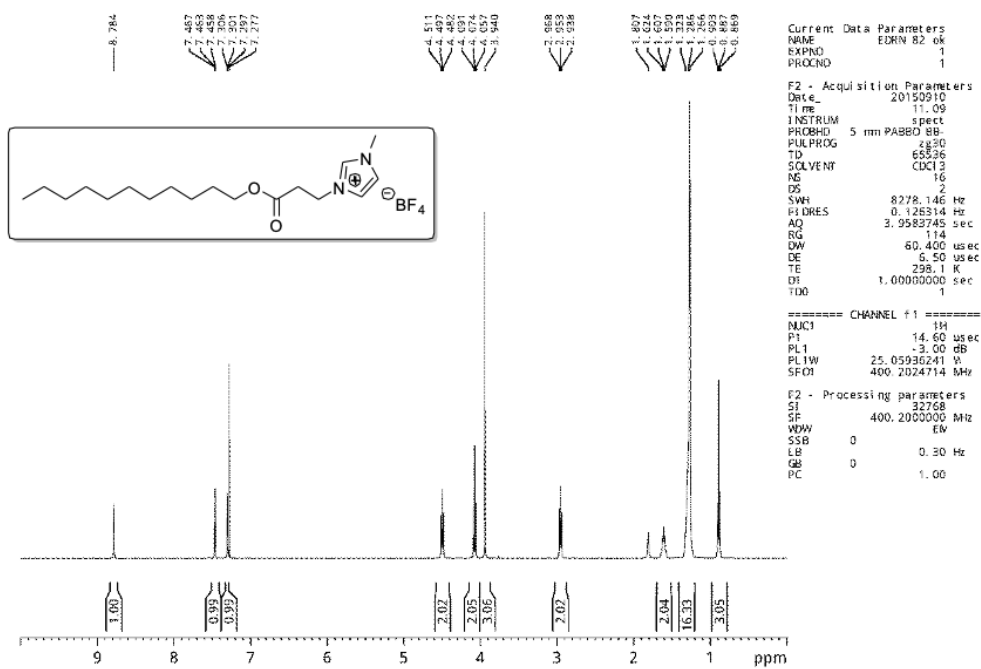
**Figure S19**: $^1H$ NMR spectrum (up) and $^{13}C$ NMR spectrum (down) in CDCl$_3$ of [C$_{11:0}E_{(2)}$Im]BF$_4$
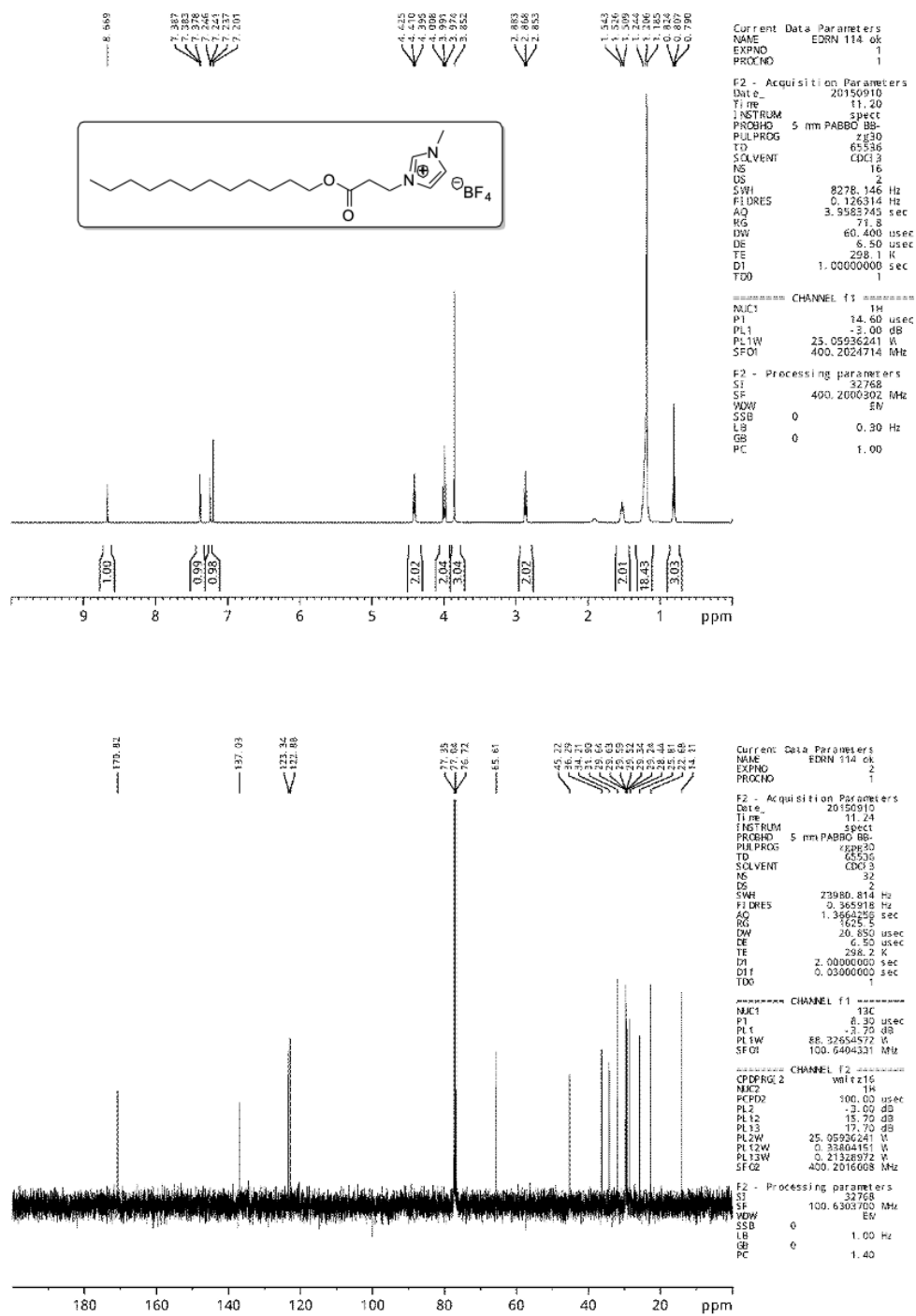
**Figure S20**: $^1H$ NMR spectrum (up) and $^{13}C$ NMR spectrum (down) in CDCl$_3$ of [C$_{12:0}E_{(2)}$Im]BF$_4$

# 5. High Resolution Mass Spectra of IL(C)s
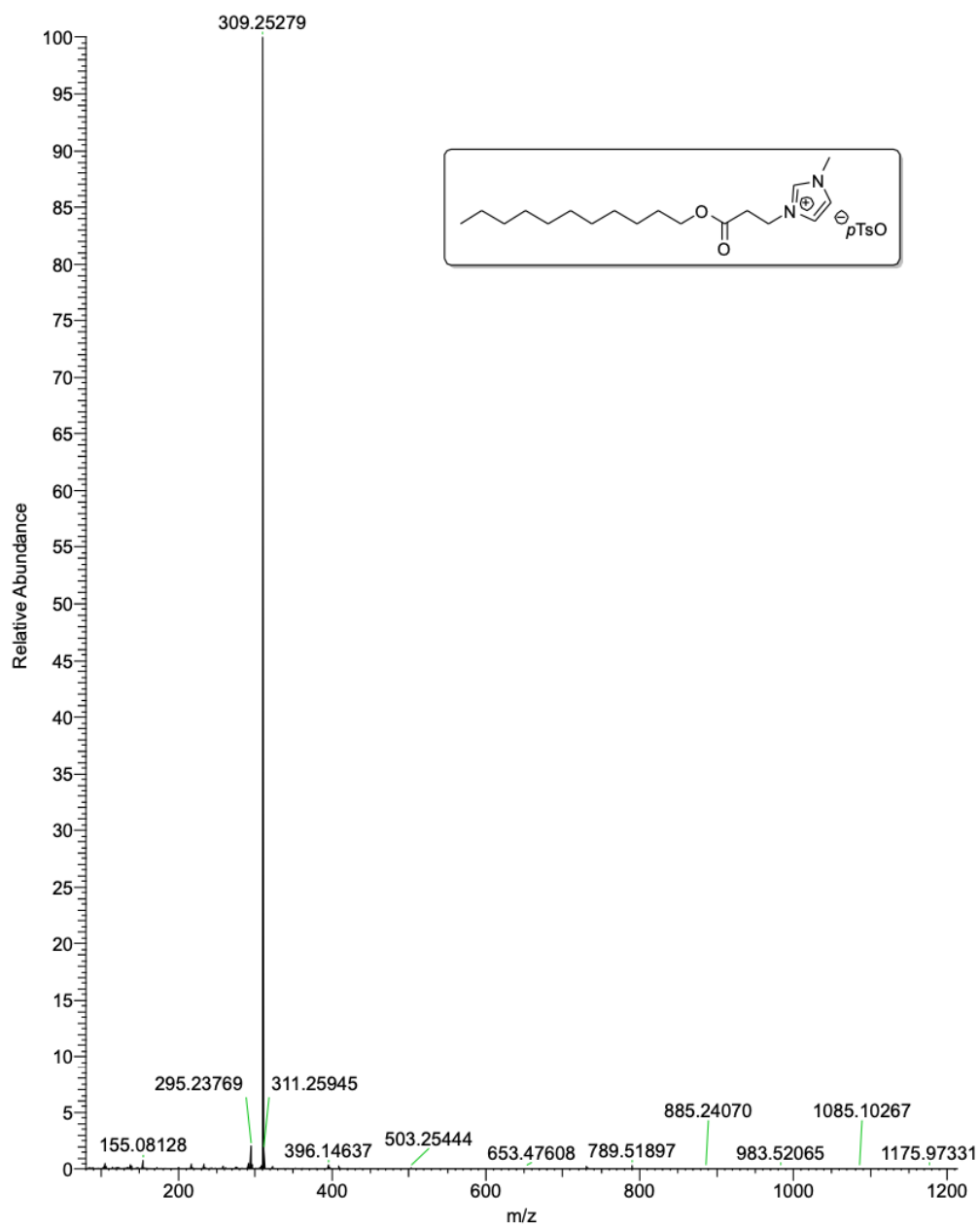


**Figure S21**: High resolution mass spectrum of [C$_{11:0}$E$_{(2)}$Im]pTsO (positive ion mode)
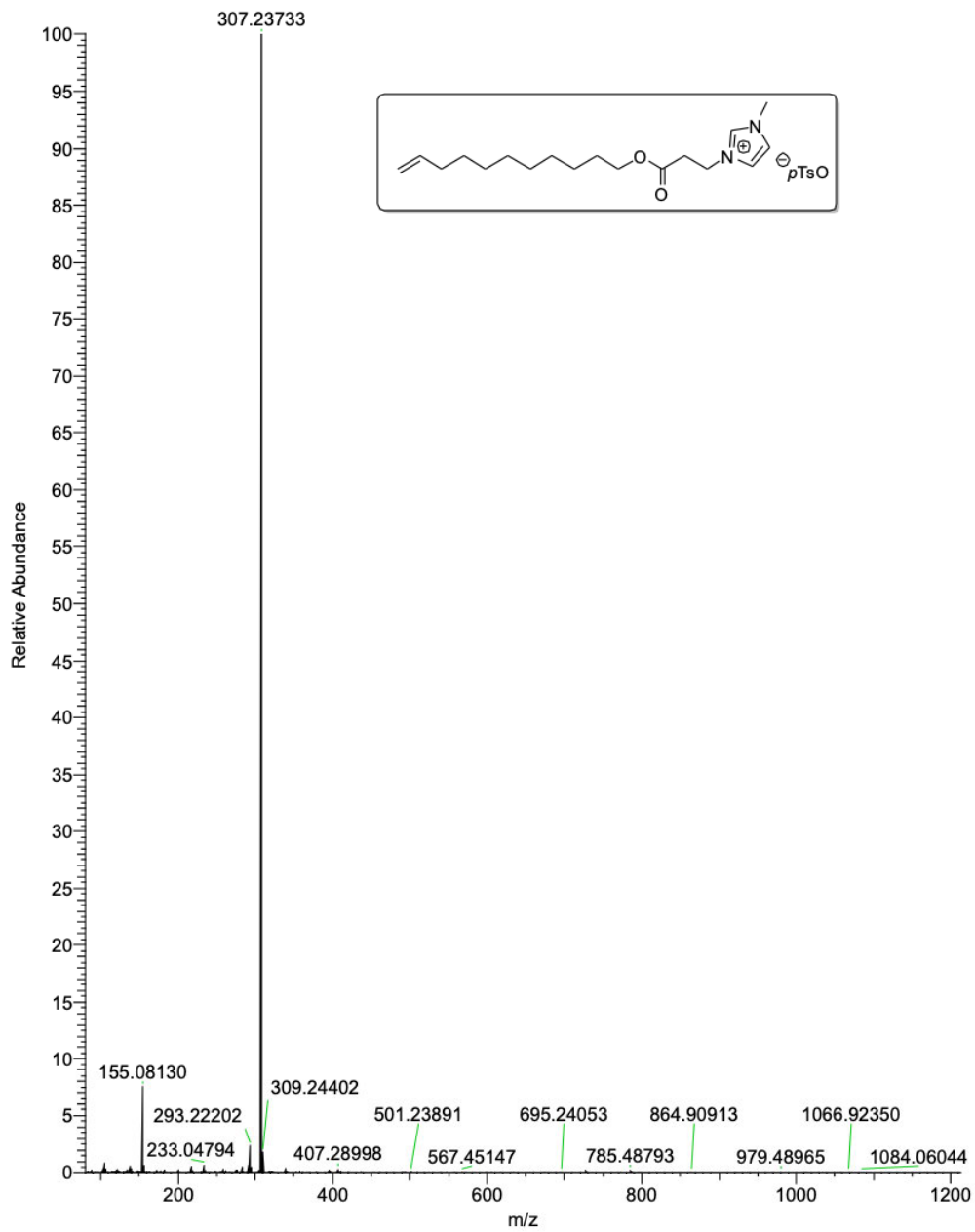
**Figure S22**: High resolution mass spectrum of [C$_{11:1}$E$_{(2)}$Im]$p$TsO (positive ion mode)
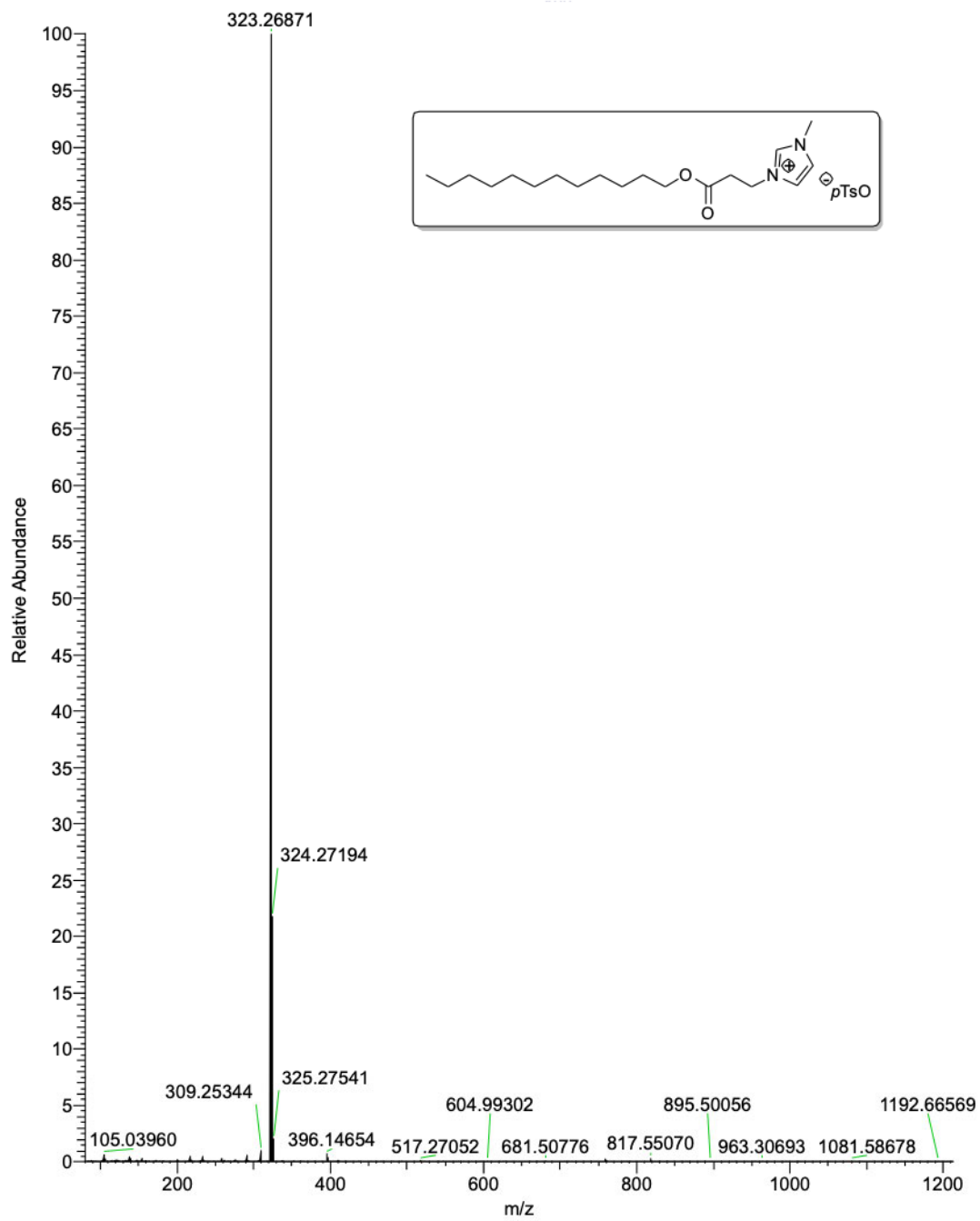
**Figure S23**: High resolution mass spectrum of [$C_{12:0}E_{(2)}$Im]$p$TsO (positive ion mode)
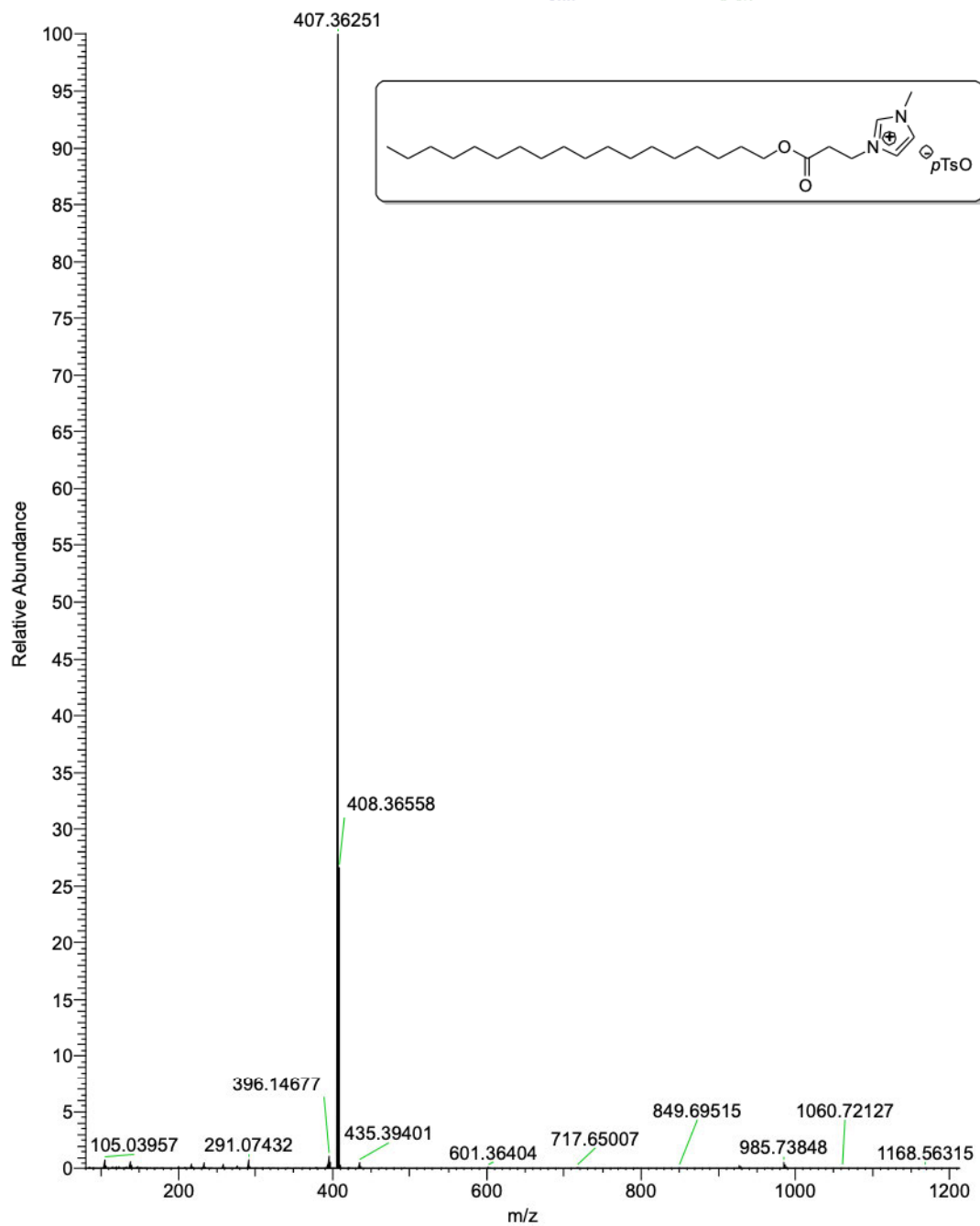
**Figure S24**: High resolution mass spectrum of [C$_{18:0}$E$_{(2)}$Im]$p$TsO (positive ion mode)
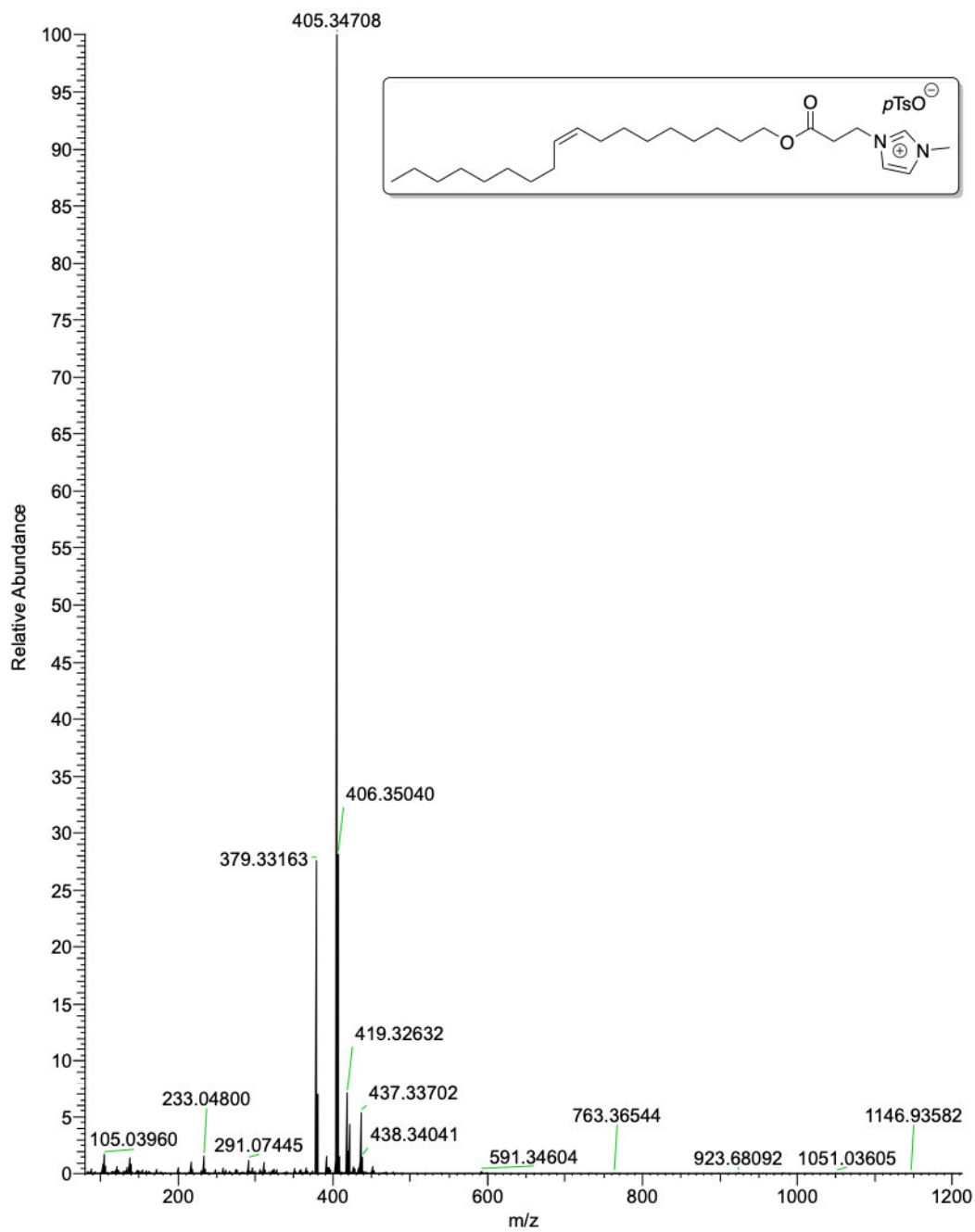
**Figure S25**: High resolution mass spectrum of [C$_{18:1}$E$_{(2)}$Im]$p$TsO (positive ion mode)
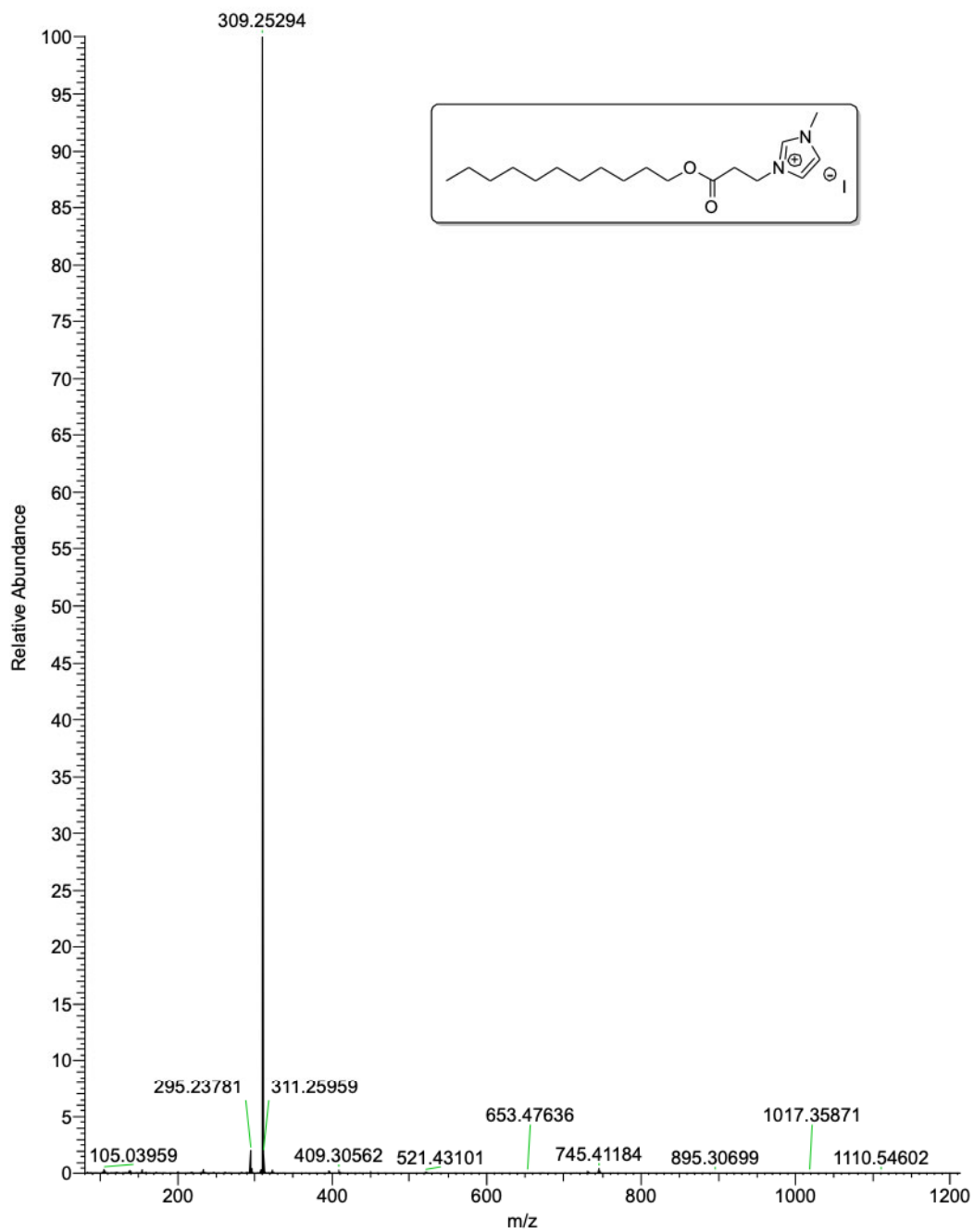
**Figure S26**: High resolution mass spectrum of [C$_{11:0}$E$_{(2)}$Im]I (positive ion mode)
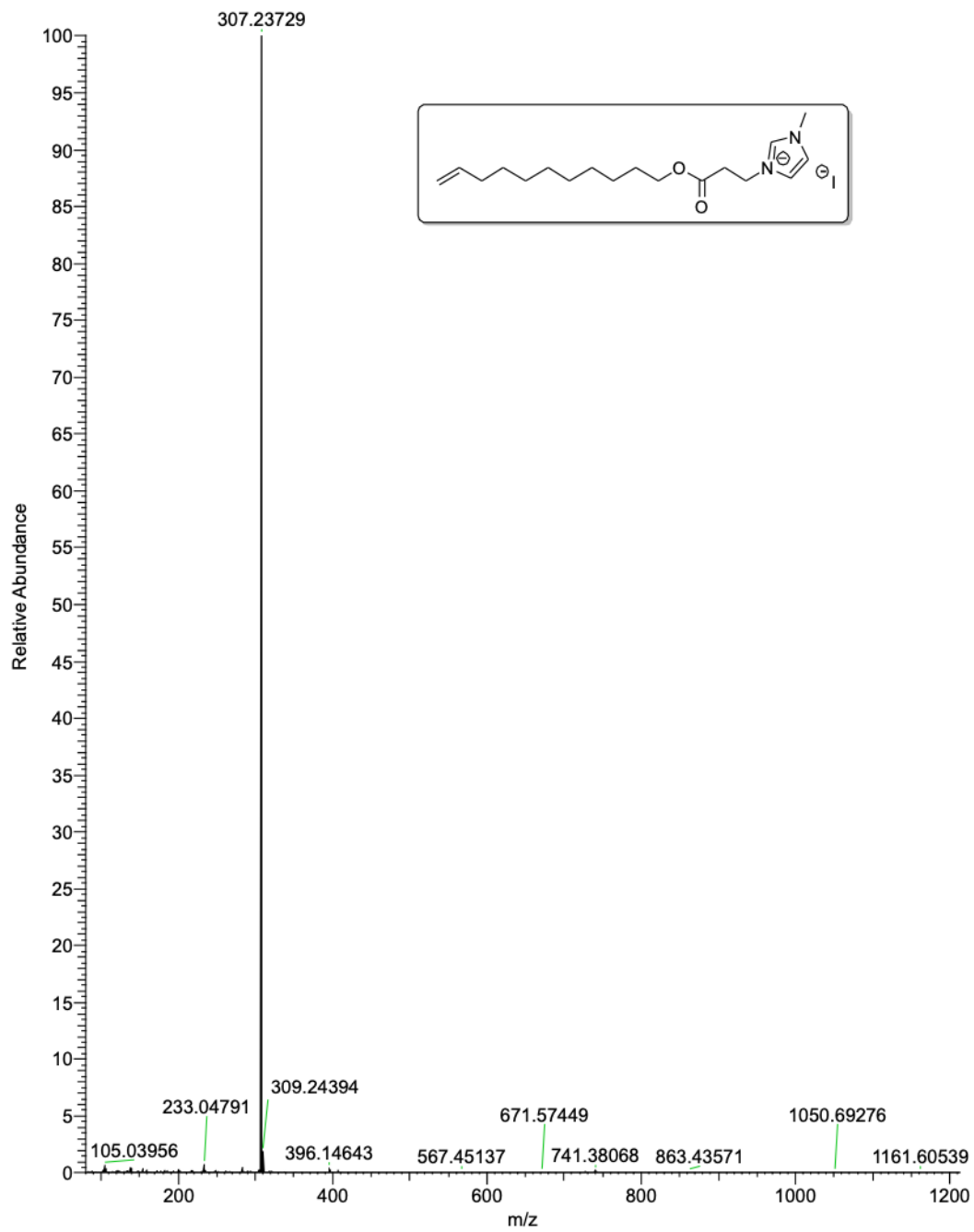
**Figure S27**: High resolution mass spectrum of [$C_{11:1}E_{(2)}$Im]I (positive ion mode)
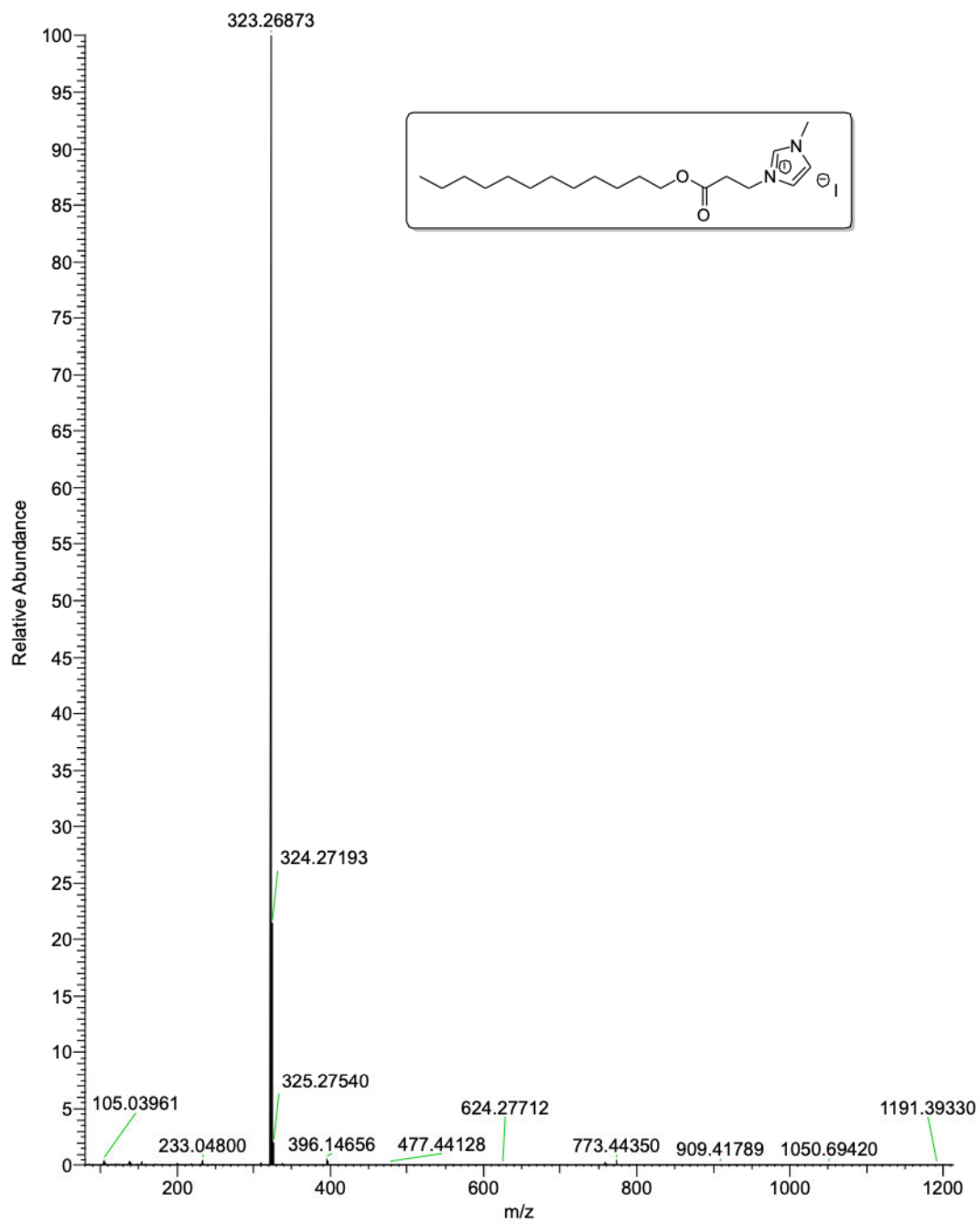
**Figure S28**: High resolution mass spectrum of [C$_{12:0}$E$_{(2)}$Im]I (positive ion mode)
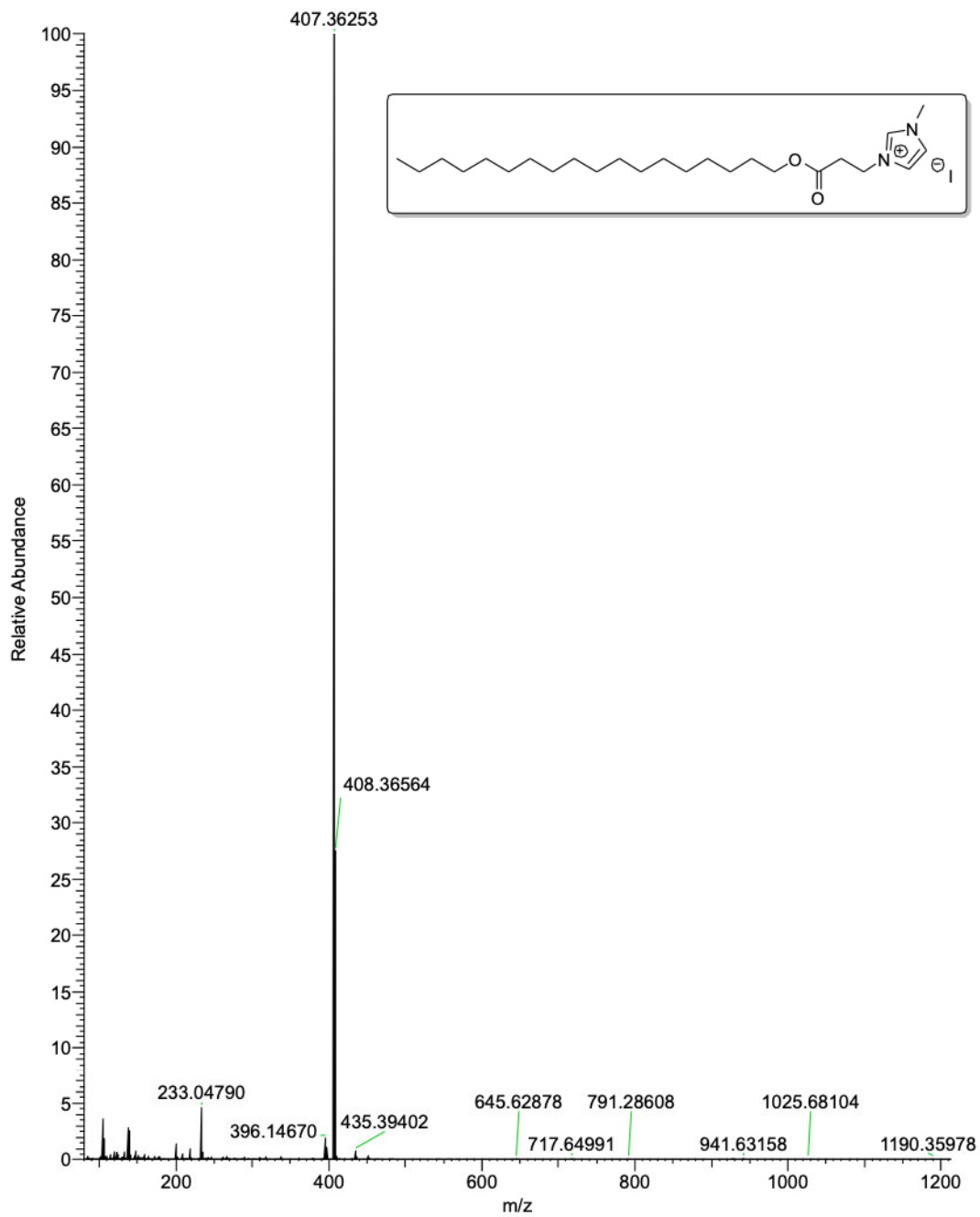
**Figure S29**: High resolution mass spectrum of [$C_{18:0}E_{(2)}$Im]I (positive ion mode)
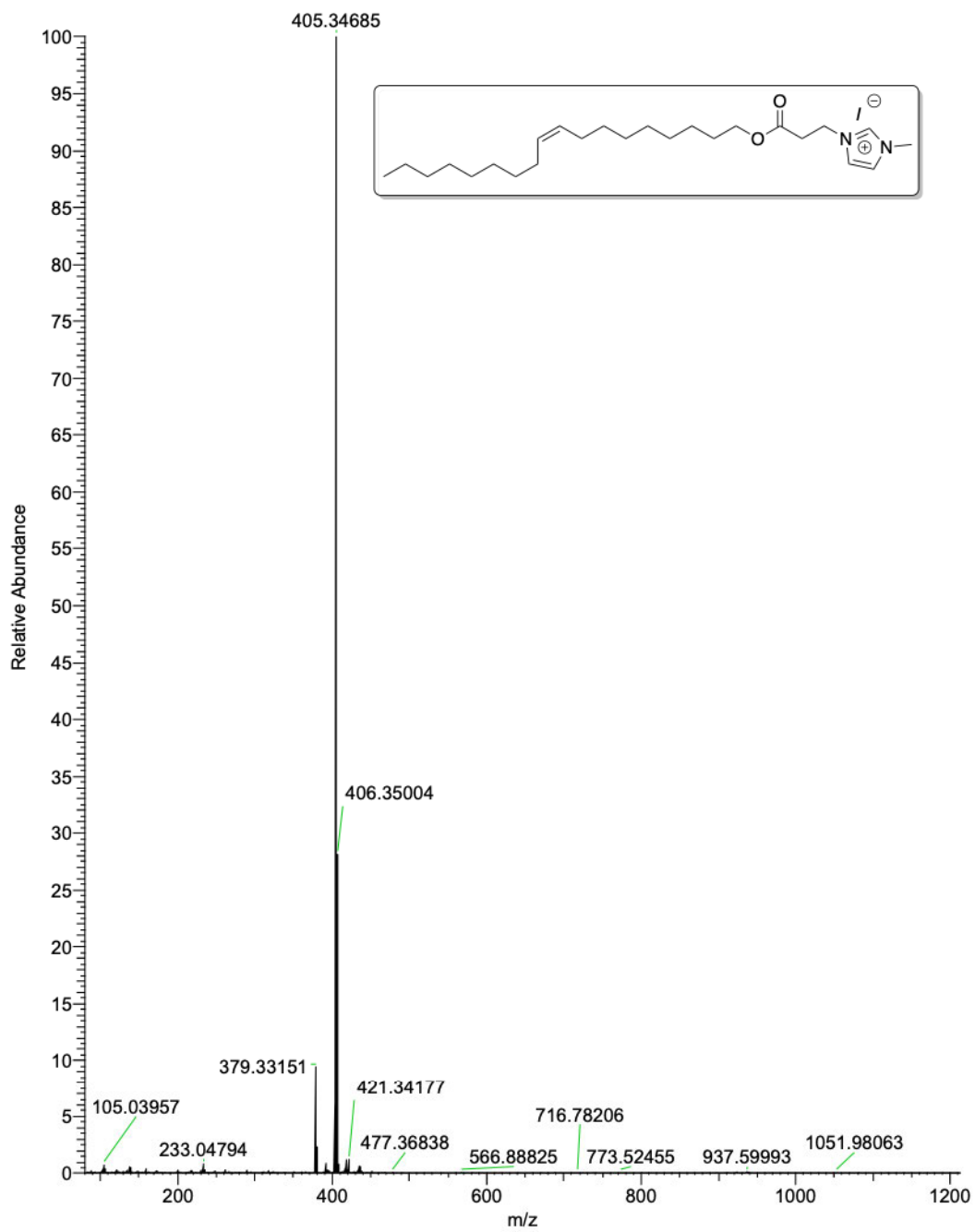
**Figure S30**: High resolution mass spectrum of [C$_{18:1}$$E_{(2)}$Im]I (positive ion mode)

**Figure S31**: High resolution mass spectrum of [C$_{11:0}$E$_{(2)}$Im]BF$_4$ (positive ion mode)

**Figure S32**: High resolution mass spectrum of [C$_{12:0}$E$_{(2)}$Im]BF$_4$ (positive ion mode)

# 6. TGA thermograms of IL(C)s

| Anion, [X] | (x:y) | TGA, *air* | | TGA, *N₂* | |
|---|---|---|---|---|---|
| | | $T_{onset}$, °C | $T_{DTGmax}$, °C | $T_{onset}$, °C | $T_{DTGmax}$, °C |
| [*p*TsO] | (1:0) | 251 | 276/300 | 246 | 270/324 |
| | (11:0) | 245 | 274/302 | 245 | 269/304 |
| | (11:1)[a] | 242 | 280 | 247 | 267/321 |
| | (12:0) | 242 | 274/303 | 243 | 277/308 |
| | (18:0) | 245 | 268/302 | 245 | 268/308 |
| | (18:1)[b] | 242 | 274 | 245 | 265/300 |
| [I] | (1:0) | 176 | 196 | 165 | 192/243 |
| | (11:0) | 206 | 233/320 | 197 | 230 |
| | (11:1) | 203 | 231 | 207 | 235/266 |
| | (12:0) | 204 | 232/330 | 209 | 235/270 |
| | (18:0) | 220 | 234/361 | 213 | 235/278 |
| | (18:1) | 210 | 235 | 211 | 237/281 |
| [BF₄] | (11:0) | 258 | 299 | 267 | 293/308 |
| | (12:0) | 245 | 286 | 262 | 304 |

**Table S1**: Thermal decomposition temperatures, $T_{onset}$, and temperature corresponding to the maxima of the differential thermogravimetry (DTG, the first derivative of the mass loss), $T_{DTGmax}$, obtained from thermogravimetric analysis (TGA) under Air and nitrogen (*N₂*) atmosphere (10 °C min⁻¹, Pt pans) for all the ILs synthesized in this study.

All the [C$_{x:y}$E$_{(2)}$ImMe]X salts are stable under ambient conditions and may be handled under normal laboratory conditions. Their stability as a function of temperature was investigated under both nitrogen and air atmosphere by thermogravimetric analysis (TGA). Representative degradation profiles of the ILs are depicted in Figure S21. The temperatures of the onset of the degradation, $T_{onset}$, are reported in Table 1 for all the lipidic ILs (all the degradation profiles are available below, Figure S22 to S35). Note that the onset of the degradation is conventionally considered as the intersection of the baseline weight and the tangent of the weight *versus* temperature curve as decomposition occurs. The temperature corresponding to the maxima of the differential thermogravimetry (DTG, the first derivative of the mass loss), $T_{DTGmax}$, are also reported in Table S1. For the whole series, it is clear that $T_{onset}$ as well as $T_{DTGmax}$ obtained under air and N₂ atmospheres are very close to each other. The steadiness of the degradation process under different gas atmospheres was already reported into the literature for classical 1-alkyl-3-methylimidazolium, [C$_{x:y}$ImMe]X, ILs.[3] It suggests that the onset of the thermal degradation is not mediated by oxidative process for both [C$_{x:y}$ImMe]X and [C$_{x:y}$E$_{(2)}$ImMe]X ILs. Thus, the ester moiety of [C$_{x:y}$E$_{(2)}$ImMe]X does not result into further susceptibility to thermal oxidation.

When compared to data reported by others for classical [C$_{x:y}$ImMe]X ILs, the values of $T_{onset}$ measured for the [C$_{x:y}$E$_{(2)}$ImMe]X series are substantially smaller. For instance, Seddon et al. reported values of $T_{onset}$ of about 300 °C for [C$_{x:0}$ImMe]BF₄. In comparison, we measured $T_{onset}$ ~ 250 °C for [C$_{12:0}$E$_{(2)}$ImMe]BF₄ and

[$C_{11:0}E_{(2)}$ImMe]BF$_4$, suggesting that the introduction of the ester bond results in a decrease of the onset of the decomposition temperature of the ILs of approximately 50 °C. This observation is consistent with results published by Garcia et al. for [$C_{x:y}E_{(1)}$ImMe]Cl. They reported that the temperature corresponding to the onset of the decomposition were 50-70 °C smaller than those of the corresponding [$C_{x:y}$ImMe]Cl ILs.[4] The degradability of [$C_{x:y}E_{(1)}$ImMe]X and [$C_{x:y}E_{(2)}$ImMe]X ILs is thus expected to be comparable, suggesting that the position of the ester bonds within the lipidic chain ($E_{(1)}$ or $E_{(2)}$) has very little effect on the stability of the corresponding ILs.



**Figure S33**: Ramped temperature TGA ($N_2$ atmosphere, 10 °C min$^{-1}$, Pt pans) for (a) [$C_{x:0}E_{(2)}$ImMe]pTsO salts with $x$ = 1, 12 and 18, and for (b) [$C_{11:0}E_{(2)}$ImMe]X salts with X = pTsO, I and BF$_4$.

As for the evolution of the degradation profiles within the series of [$C_{x:y}E_{(2)}$ImMe]X ILs as a function of $x$, $y$ and X, the expected tendencies are observed. First of all, $T_{onset}$ is independent of $x$ and $y$ as suggested by Figure S21a. The same behavior was reported by others for classical [$C_{x:y}$ImMe]X ILs. When considering the influence of the counter-anion, X, it appears that the thermal stability of [$C_{x:y}E_{(2)}$ImMe]X ILs varies according to the following order: [pTsO] ~ [BF$_4$] > [I], with iodide ILs exhibiting $T_{onset}$ approximately 40 °C smaller than those of tosylate and tetrafluoroborate equivalents. Again, the same trend is reported in the literature for classical [$C_{x:y}$ImMe]X ILs. It is well known that halide anions (X = Cl, Br, I) significantly reduce the thermal stability of ILs due to their relatively high nucleophilic and basic character.[5] In particular, it was proposed that the degradation of halide imidazolium ILs proceeds *via* the dealkylation of the imidazolium core according to a Sn2 mechanism, also known as the reverse Menshutkin reaction. Moreover, due to the higher steric hindrance of the longer alkyl chain, $C_{x:y}$, it was observed that the

nucleophilic attack preferentially occurs on the methyl group, Me, providing the neutral $C_{x:y}Im$ species as the first degradation byproduct of the thermal decomposition of [$C_{x:y}ImMe$]X ILs.[6]

In the case of [$C_{x:y}E_{(2)}ImMe$]X, the TGA results suggest a different scenario. First of all, the significant decrease of $T_{onset}$ for [$C_{x:y}E_{(2)}ImMe$]X as compared to [$C_{x:y}ImMe$]X suggests that the decomposition process of [$C_{x:y}E_{(2)}ImMe$]X occurs through a fundamentally different mechanism, noticeably through a reaction of lower activation energy than the reverse Menshutkin reaction. Moreover, for most of the tested ILs, the DTG profiles (first derivative) exhibit two maxima (see Table S1) suggesting that the degradation takes place in two steps. By taking a closer look at the degradation profiles, the weight percentage left after the first step suggests that the larger substituent of the imidazolium core, i.e. $C_{x:y}$, is involved in the early stage of the thermal decomposition. This can be the indication of a dealkylation through an elimination instead of a substitution.[5] In particular, it is highly suspected that the degradation process takes place *via* a *retro*-Michael reaction as suggested in Scheme S6. Further investigations would be necessary to confirm this hypothesis.

Overall, the TGA results demonstrate the higher susceptibility to thermal degradation for this new series of [$C_{x:y}E_{(2)}ImMe$]X ILs. If this feature is undesirable for high-temperature applications, it is however advantageous when considering the disposal of the ILs at the end of their life cycle. Moreover, it has already been proven that a higher susceptibility to thermal degradation coincides with a higher biodegradability in the case of [$C_{x:y}E_{(1)}ImMe$]X.[7] A similar result is expected in the case of [$C_{x:y}E_{(2)}ImMe$]X. This will be the object of future investigations.



**Scheme S6**: Proposed mechanism for the early stage of the thermal degradation of [$C_{x:y}E_{(2)}ImMe$]X ILs *via* a *retro*-Michael reaction. Representation for (*x:y*) = (18:1), X = *p*TsO.

**Figure S34**: TGA thermogram of [$C_{1:0}E_{(2)}$ImMe]$p$TsO under $N_2$



**Figure S35**: TGA thermogram of [$C_{11:0}E_{(2)}$ImMe]$p$TsO under $N_2$

**Figure S36**: TGA thermogram of [C$_{11:1}$$E_{(2)}$ImMe]]$p$TsO under N$_2$
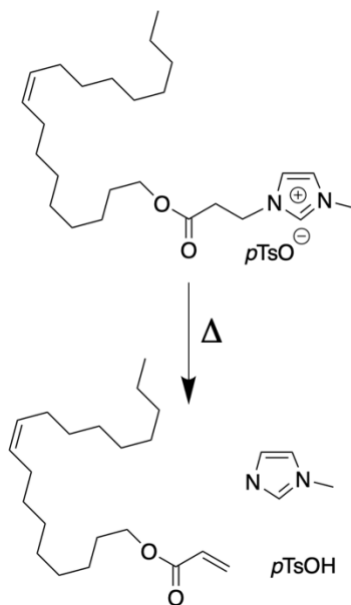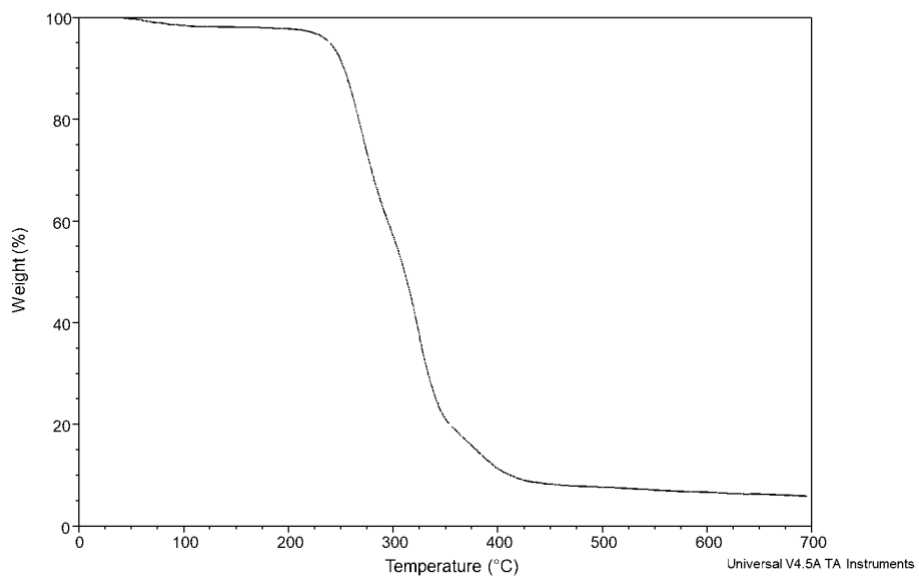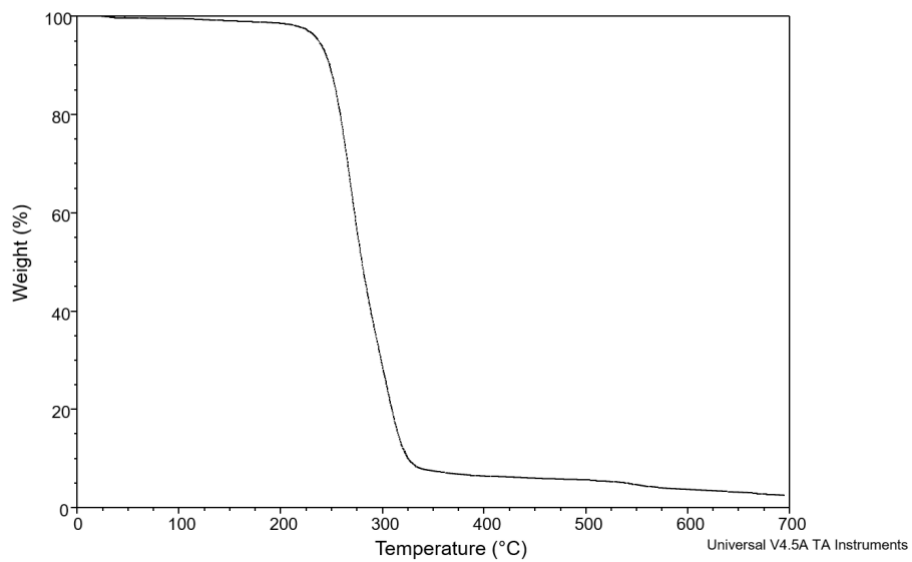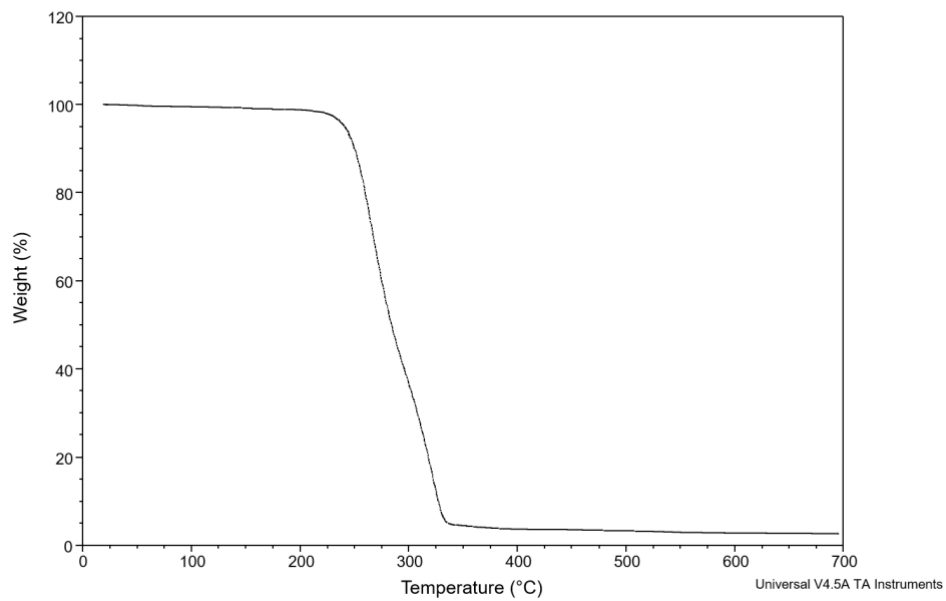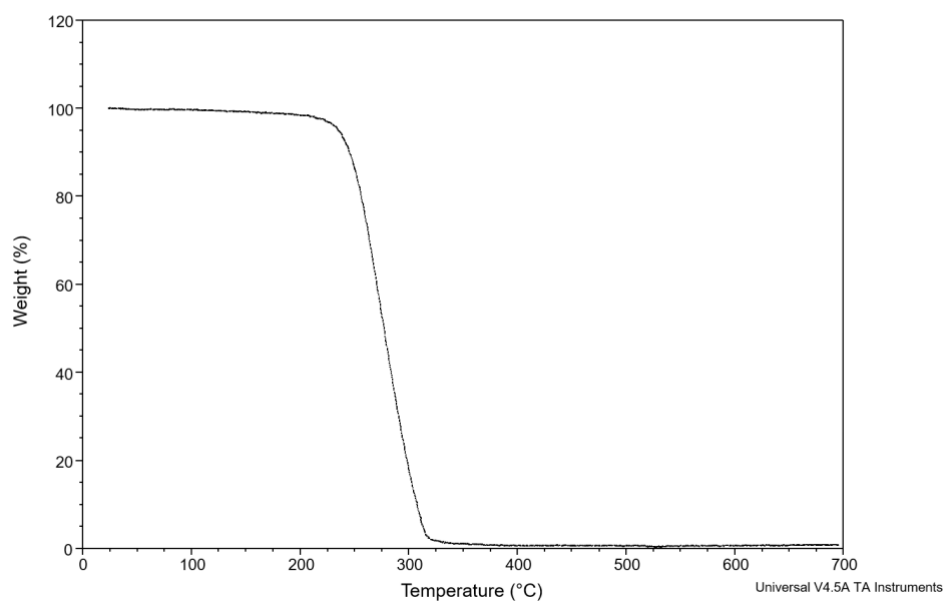


**Figure S37**: TGA thermogram of [C$_{12:0}$$E_{(2)}$ImMe]$p$TsO under N$_2$

**Figure S38**: TGA thermogram of [$C_{18:0}E_{(2)}$ImMe]$p$TsO under $N_2$



**Figure S39**: TGA thermogram of [$C_{18:1}E_{(2)}$ImMe]$p$TsO under $N_2$

**Figure S40**: TGA thermogram of $[C_{1:0}E_{(2)}ImMe]I$ under $N_2$



**Figure S41**: TGA thermogram of $[C_{11:0}E_{(2)}ImMe]I$ under $N_2$

**Figure S42**: TGA thermogram of [$C_{11:1}E_{(2)}$ImMe]I under $N_2$



**Figure S43**: TGA thermogram of [$C_{12:0}E_{(2)}$ImMe]I under $N_2$

**Figure S44**: TGA thermogram of [C$_{18:0}$E$_{(2)}$ImMe]I under N$_2$



**Figure S45**: TGA thermogram of [C$_{18:1}$E$_{(2)}$ImMe]I under N$_2$

**Figure S46**: TGA thermogram of [C$_{11:0}$$E_{(2)}$ImMe]BF$_4$ under N$_2$
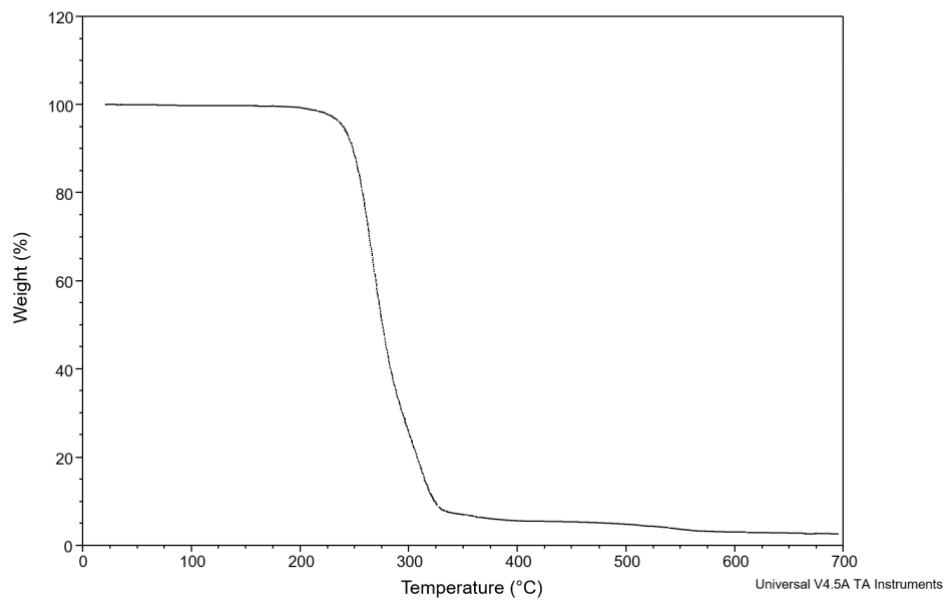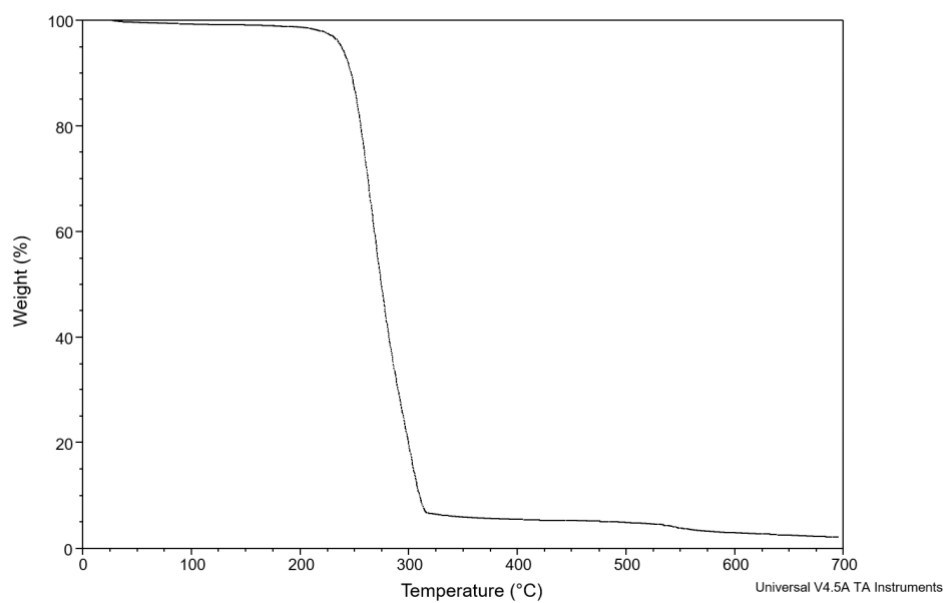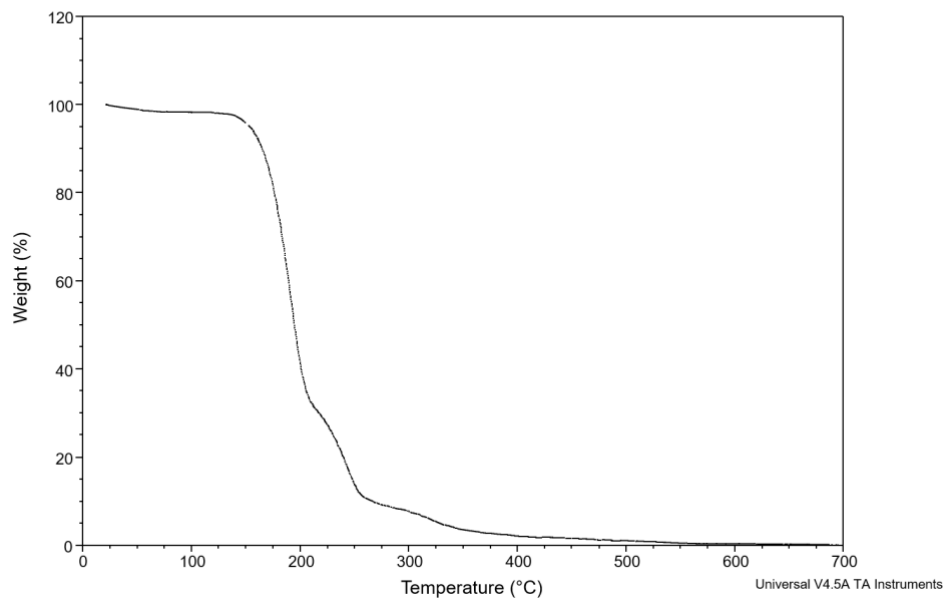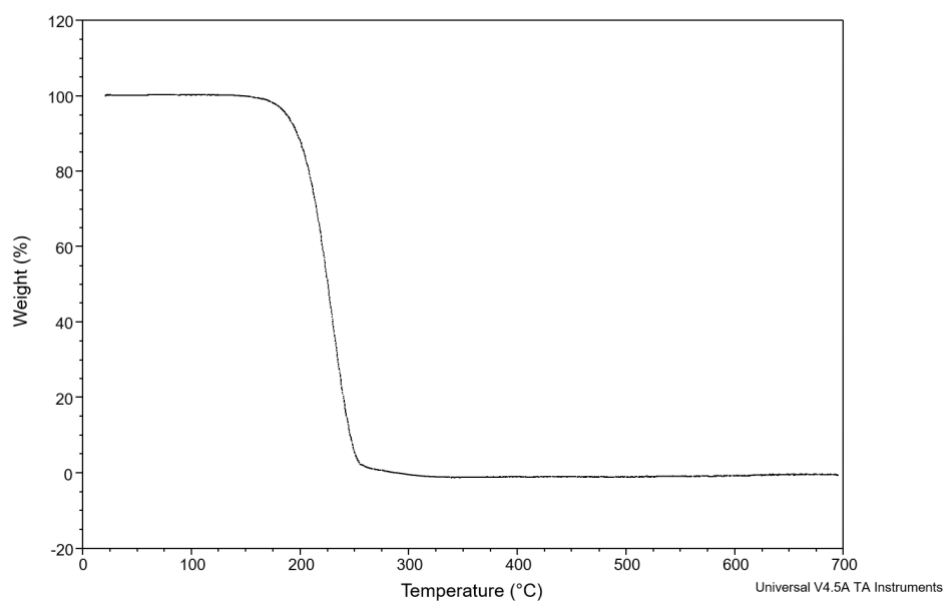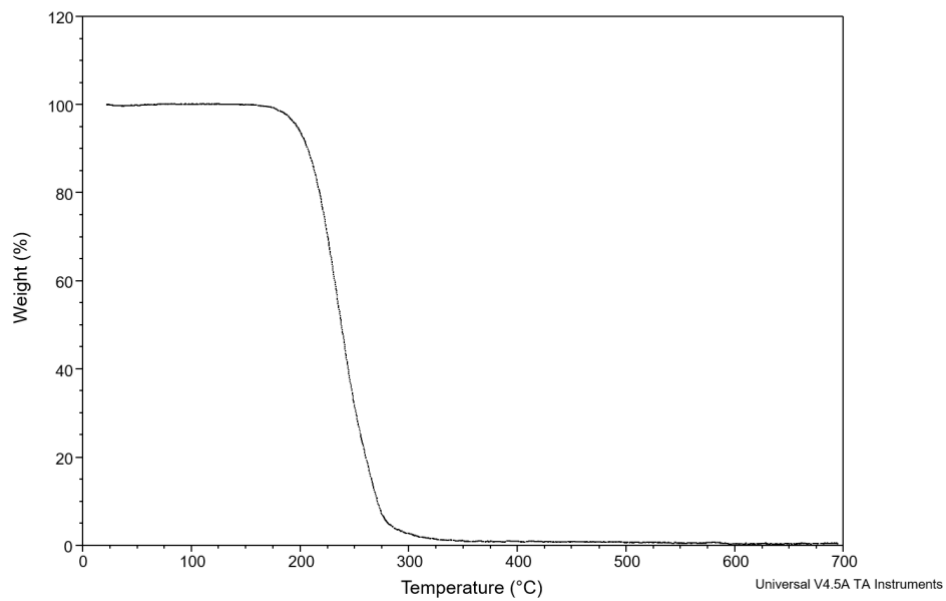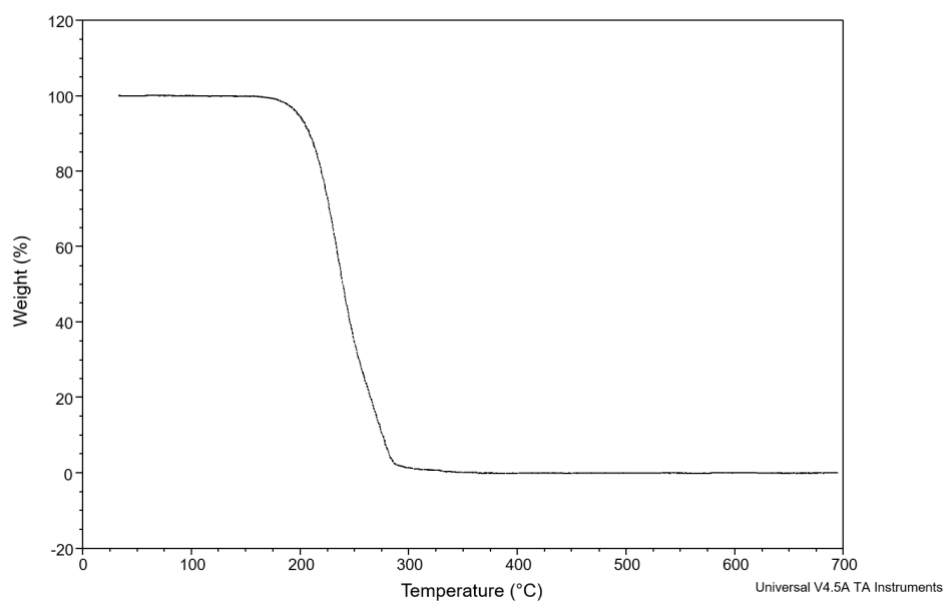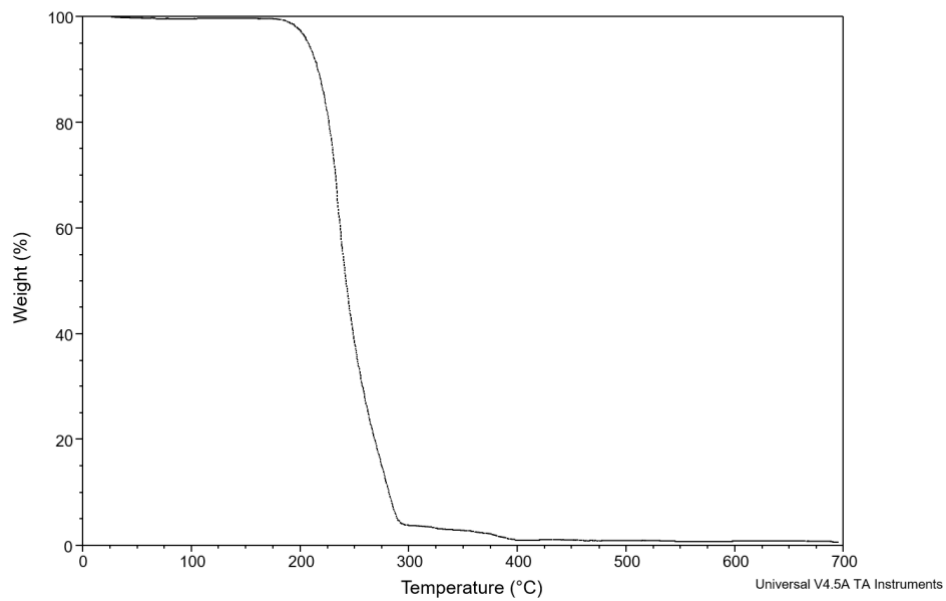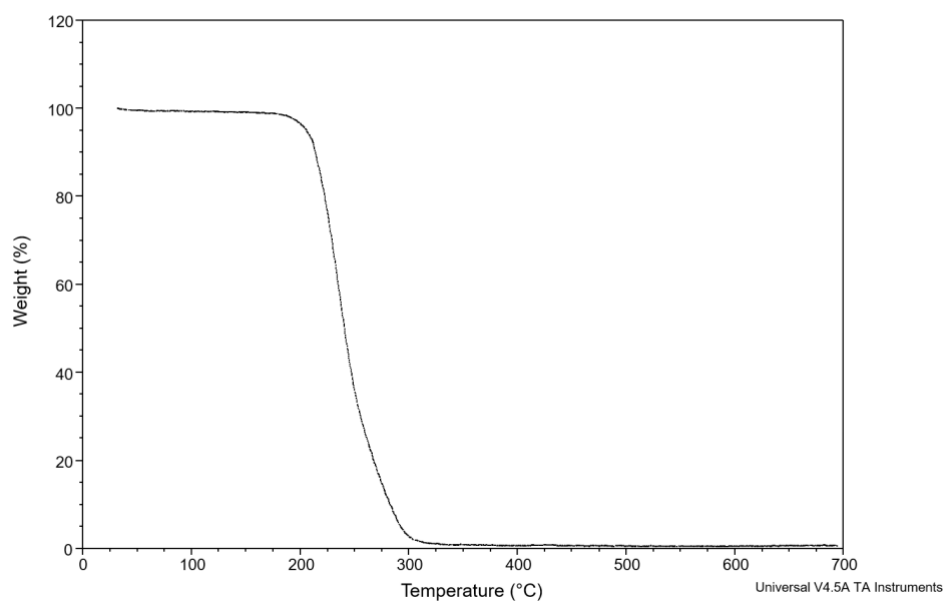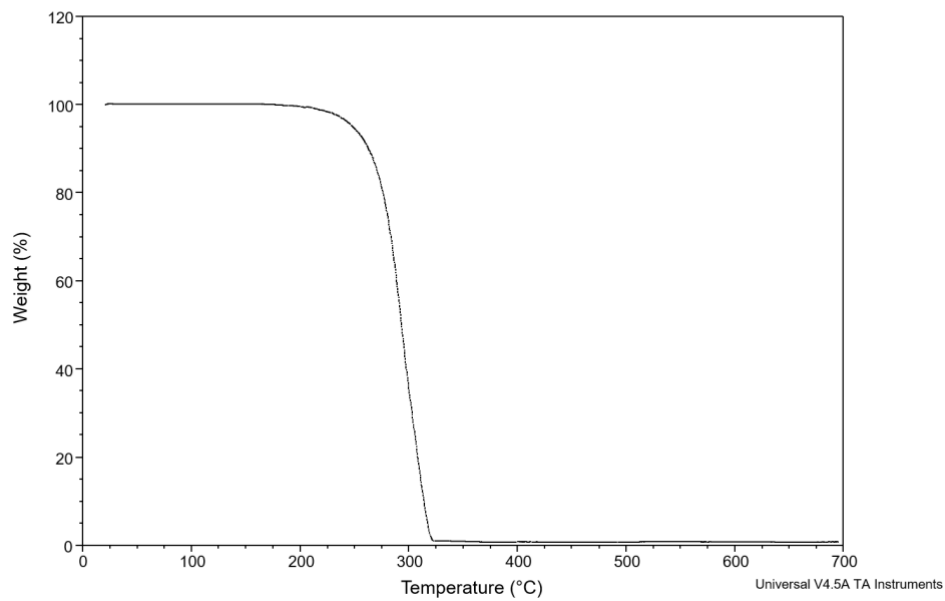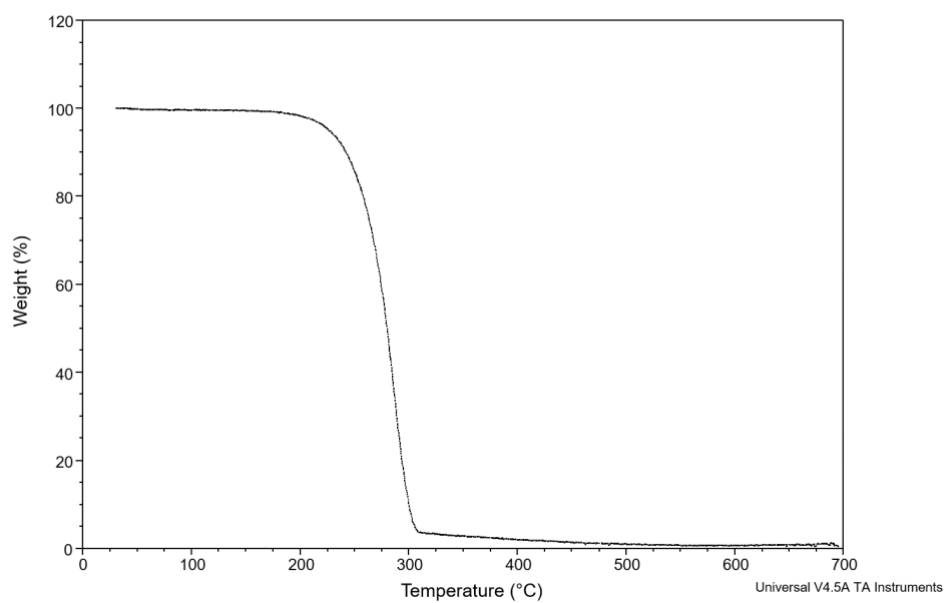


**Figure S47**: TGA thermogram of [C$_{12:0}$$E_{(2)}$ImMe]BF$_4$ under N$_2$

# 7. DSC thermograms of IL(C)s
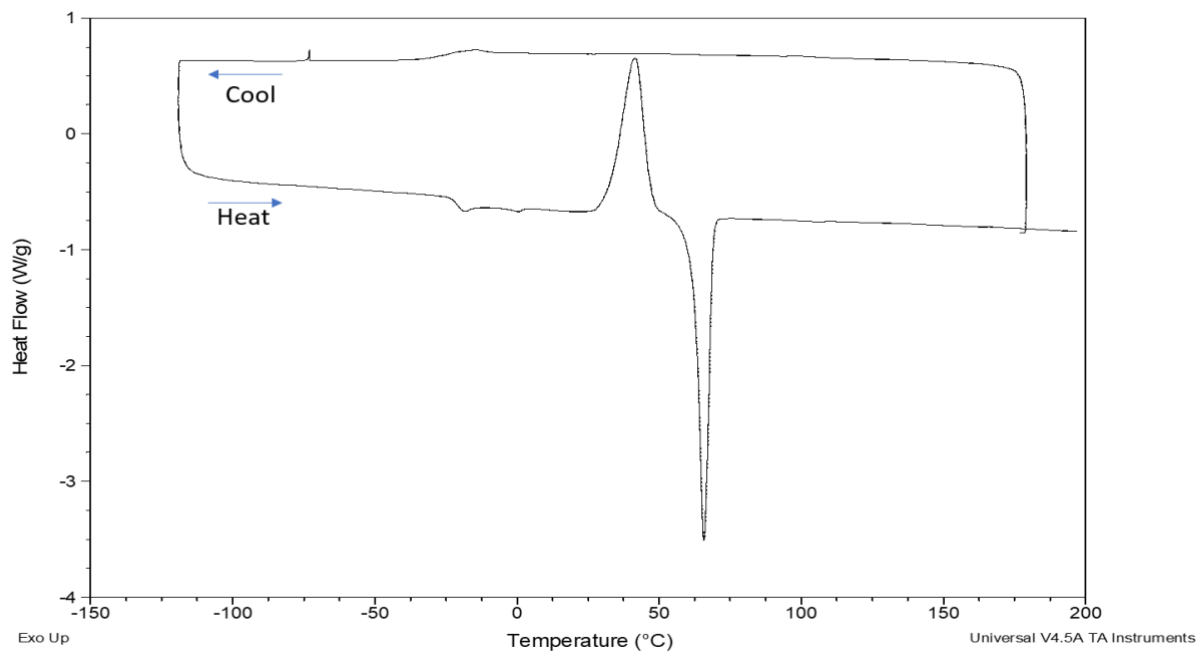


**Figure S48**: DSC thermogram of [C$_{1:0}$E$_{(2)}$ImMe]pTsO under N$_2$ (cycle 2: cool, cycle 3: heat)
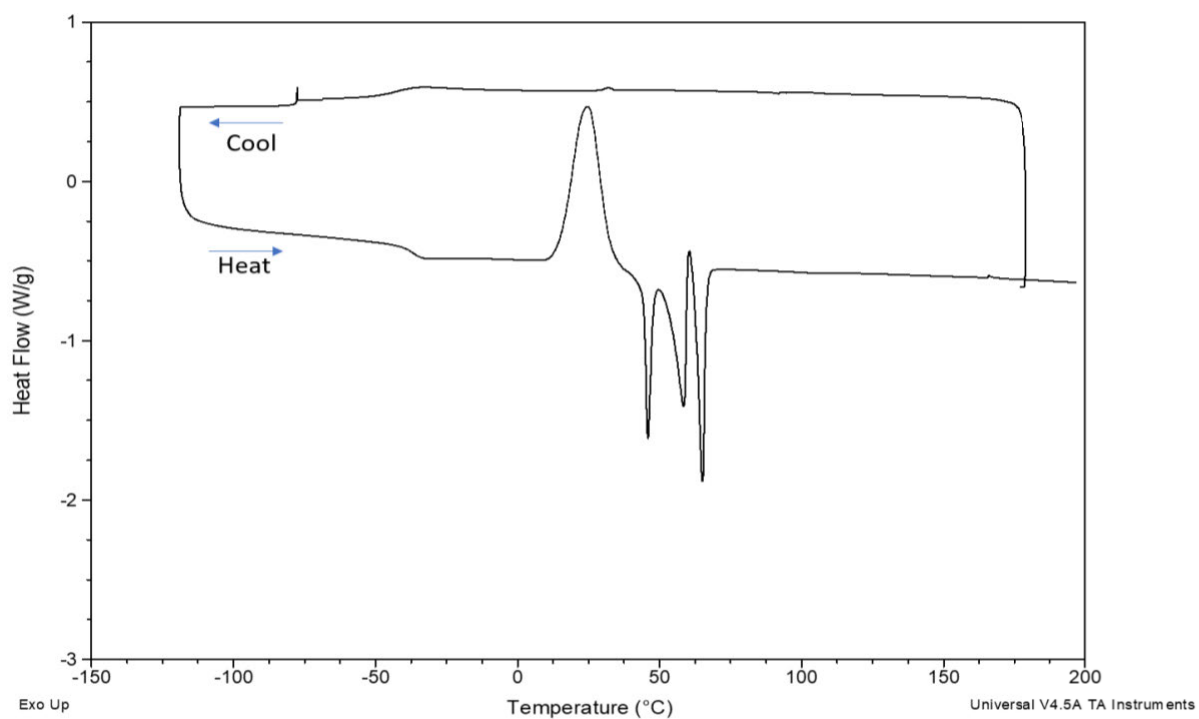


**Figure S49**: DSC thermogram of [C$_{11:0}$E$_{(2)}$ImMe]pTsO under N$_2$ (cycle 2: cool, cycle 3: heat)
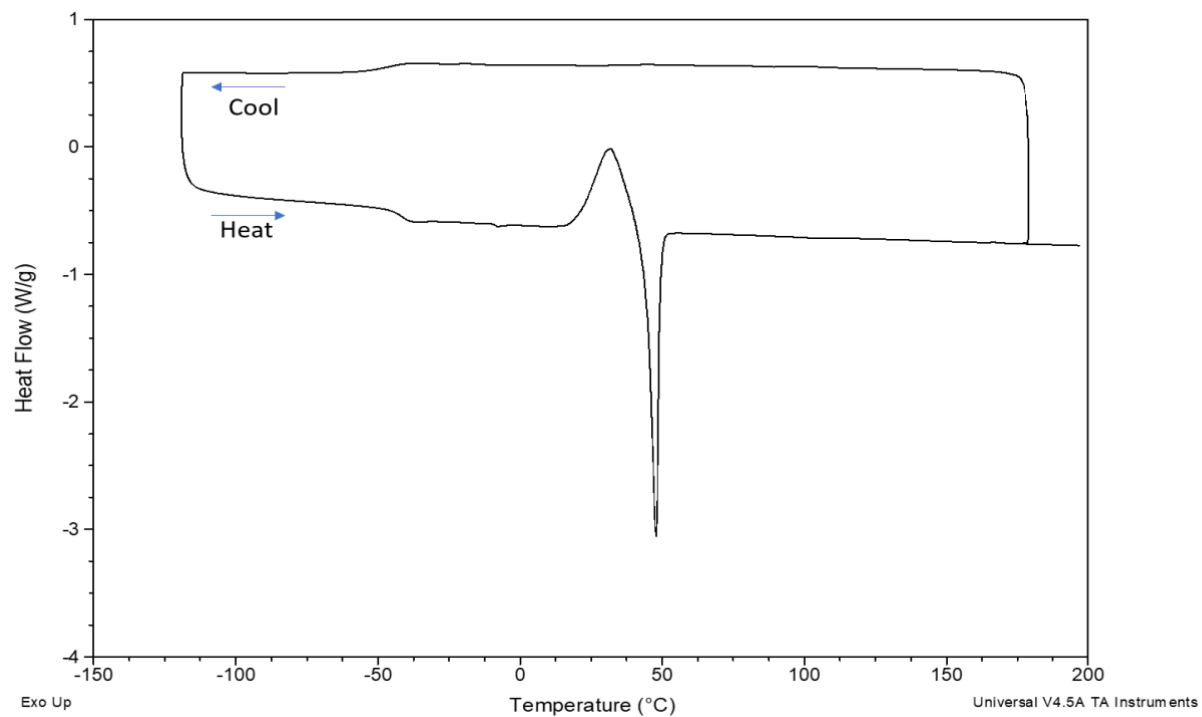
**Figure S50**: DSC thermogram of [C$_{11:1}$E$_{(2)}$ImMe]$p$TsO under N$_2$ (cycle 2: cool, cycle 3: heat)
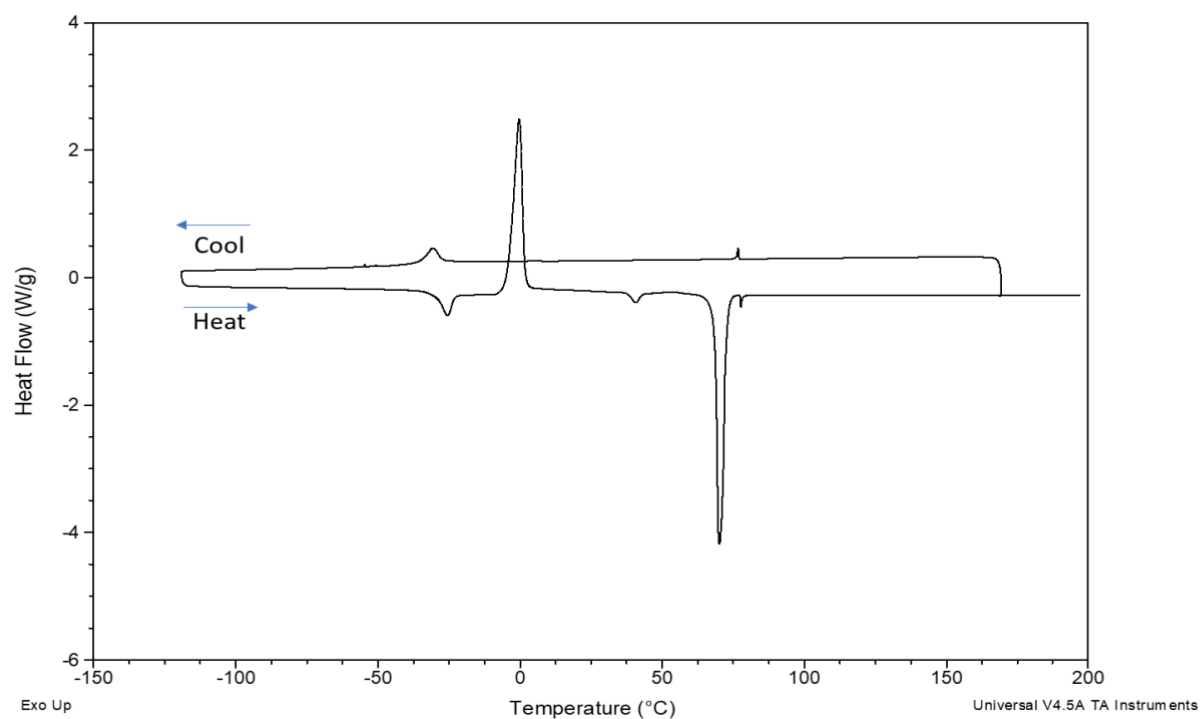


**Figure S51**: DSC thermogram of [C$_{12:0}$E$_{(2)}$ImMe]$p$TsO under N$_2$ (cycle 2: cool, cycle 3: heat)
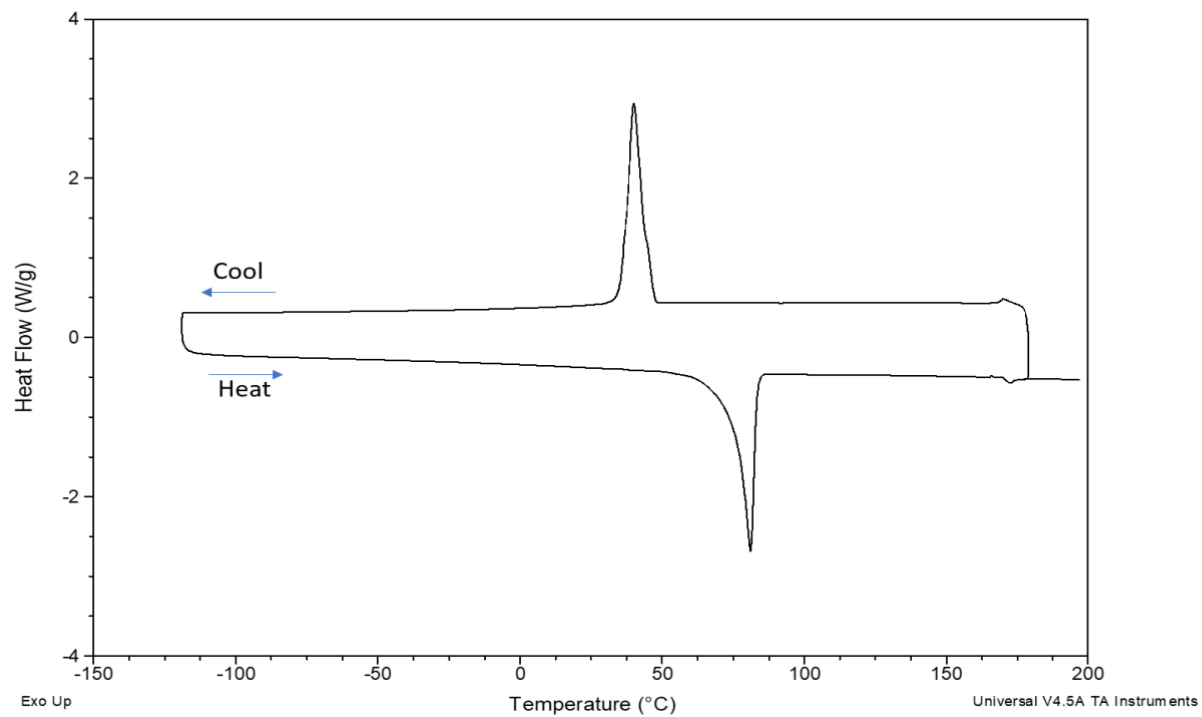
**Figure S52**: DSC thermogram of [C$_{18:0}$E$_{(2)}$ImMe]$p$TsO under N$_2$ (cycle 2: cool, cycle 3: heat)
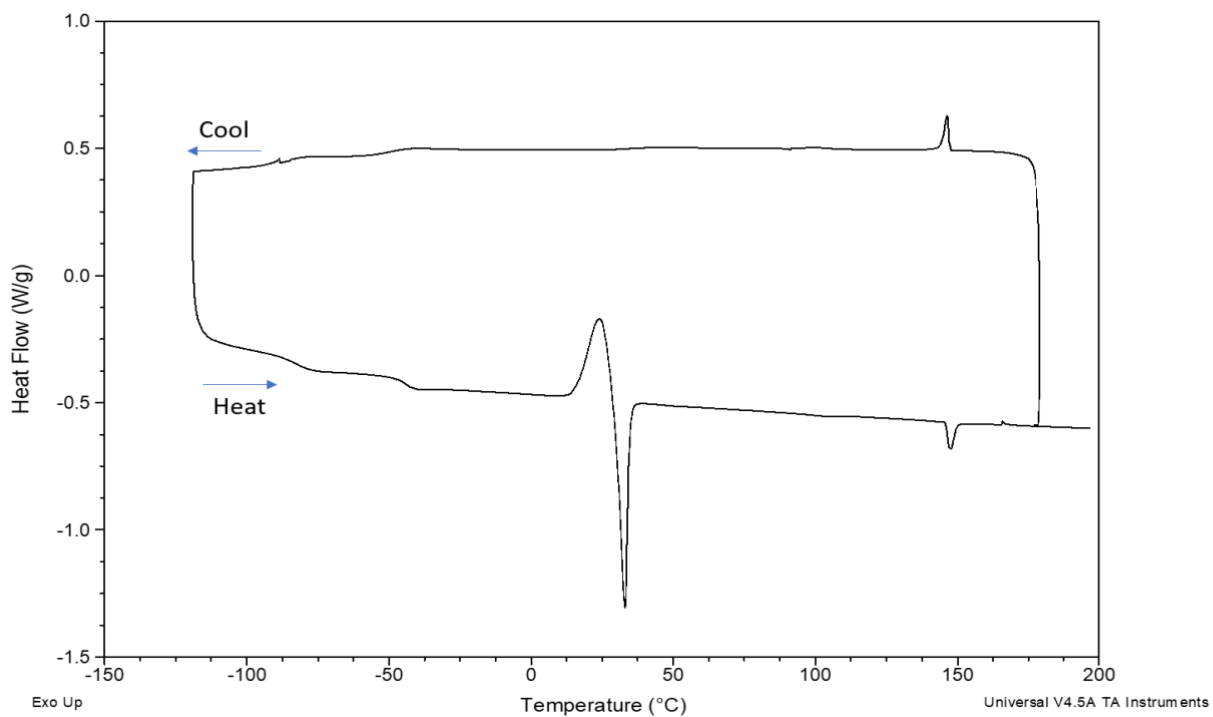


**Figure S53**: DSC thermogram of [C$_{18:1}$E$_{(2)}$ImMe]$p$TsO under N$_2$ (cycle 2: cool, cycle 3: heat)
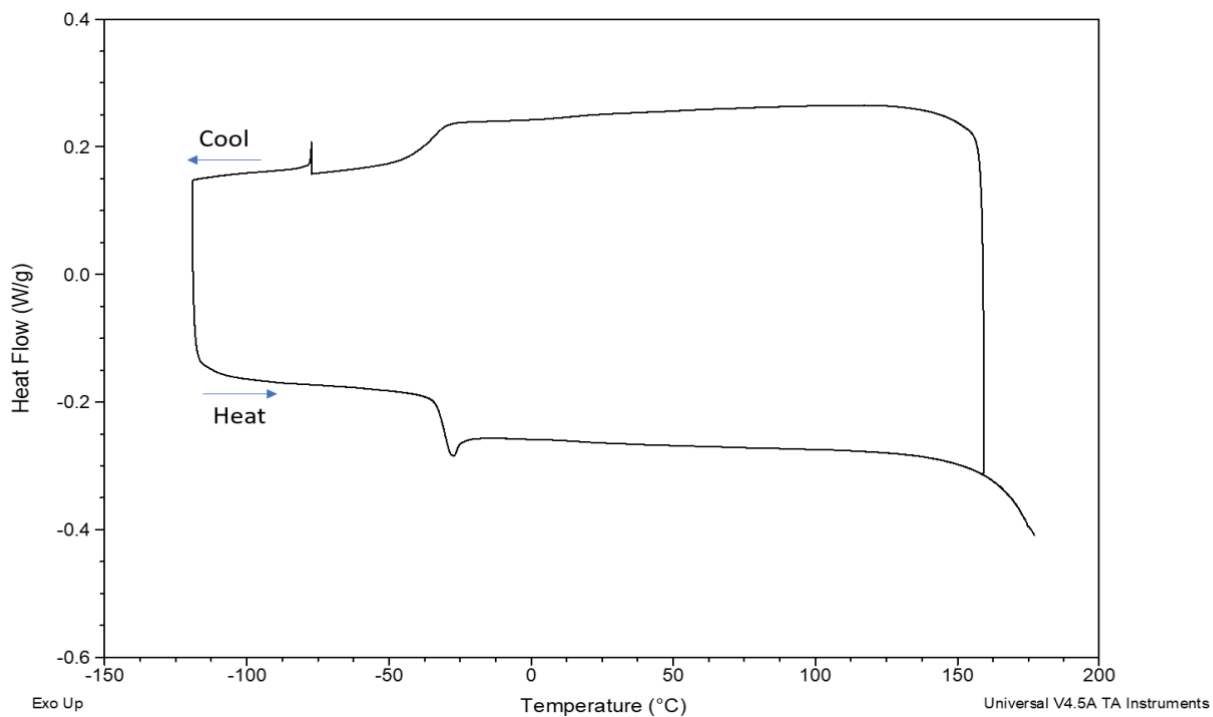
**Figure S54**: DSC thermogram of [C$_{1:0}$E$_{(2)}$ImMe]I under N$_2$ (cycle 2: cool, cycle 3: heat)
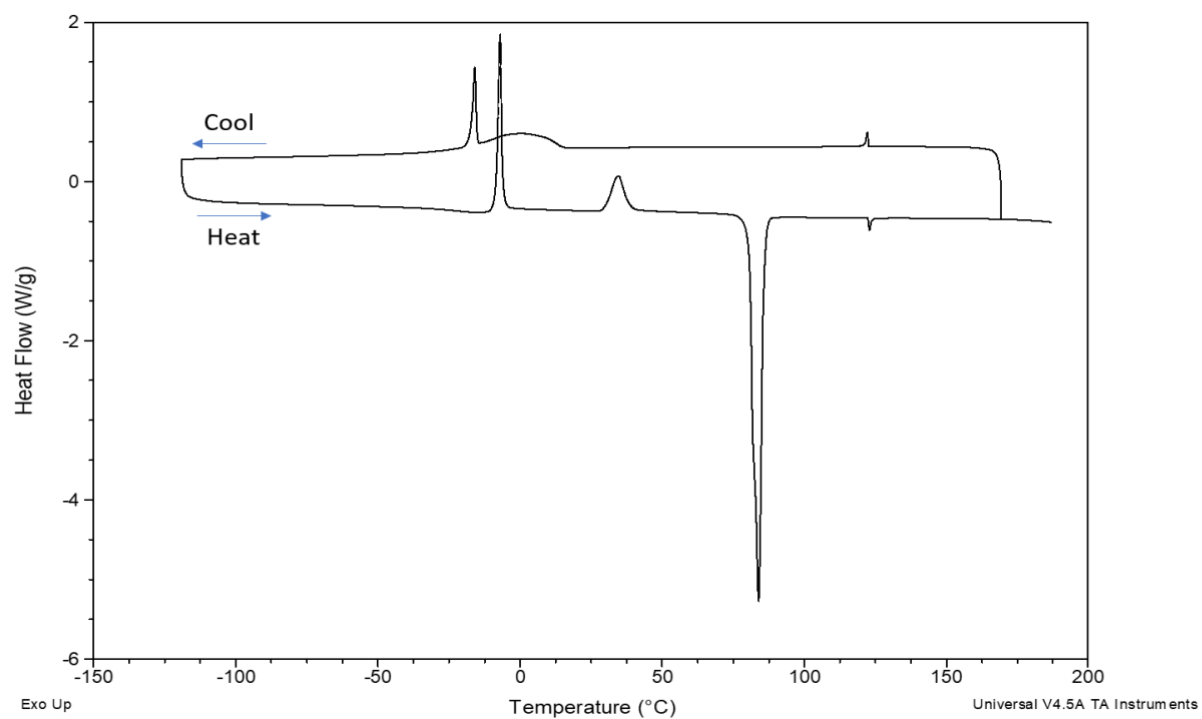


**Figure S55**: DSC thermogram of [C$_{11:0}$E$_{(2)}$ImMe]I under N$_2$ (cycle 2: cool, cycle 3: heat)
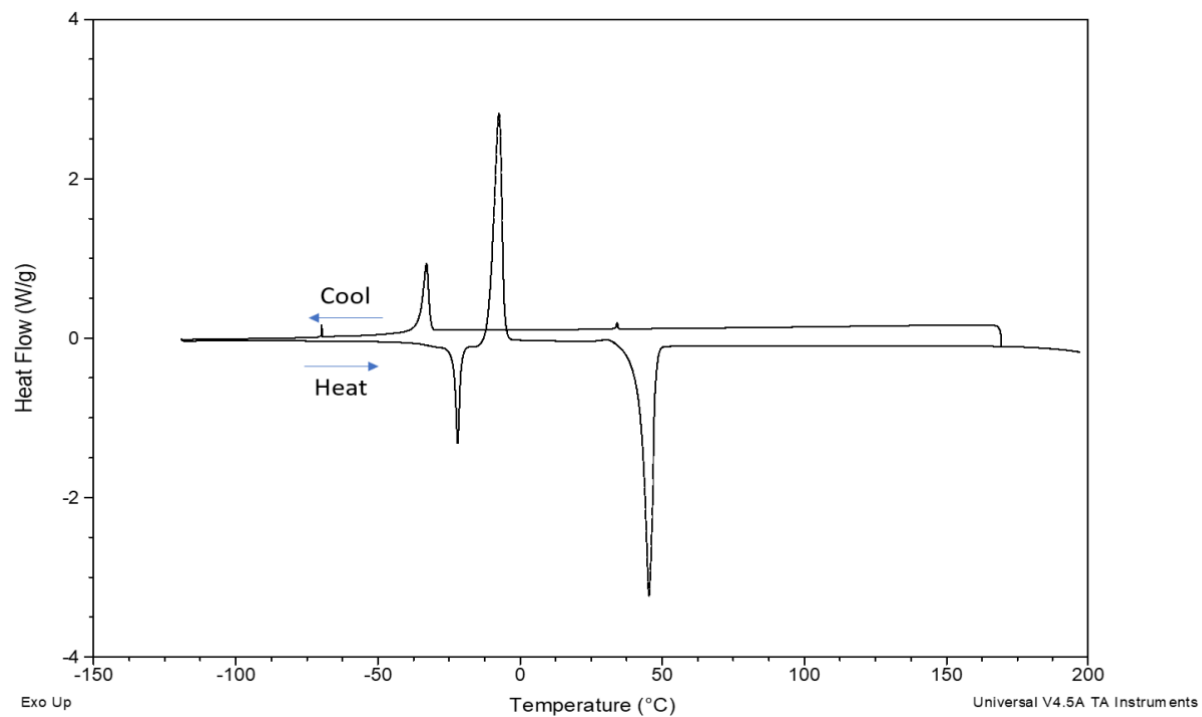
**Figure S56**: DSC thermogram of [C$_{11:1}$E$_{(2)}$ImMe]I under N$_2$ (cycle 2: cool, cycle 3: heat)
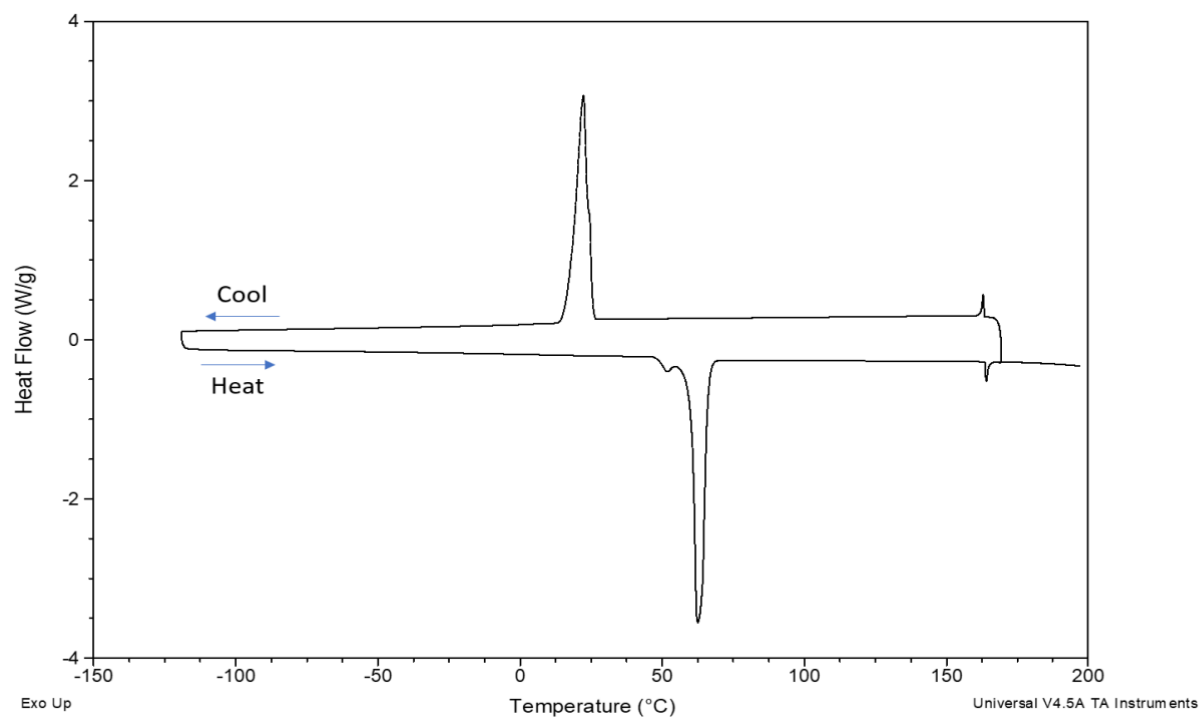


**Figure S57**: DSC thermogram of [C$_{12:0}$E$_{(2)}$ImMe]I under N$_2$ (cycle 2: cool, cycle 3: heat)
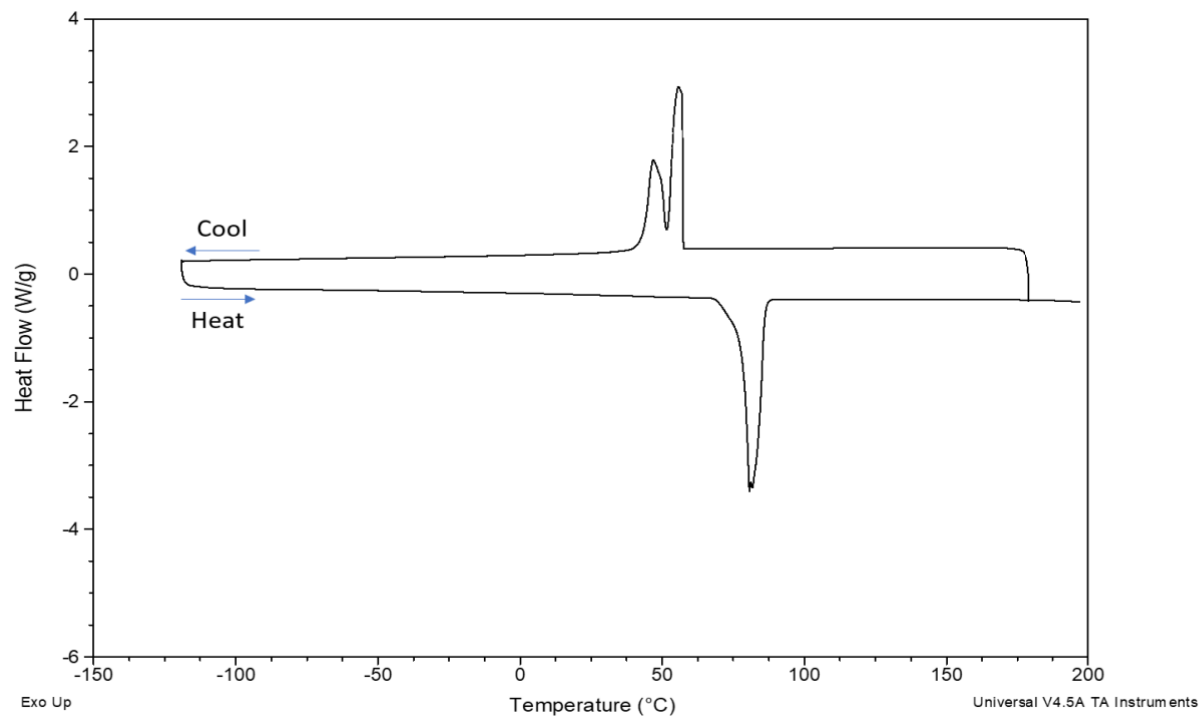
**Figure S58**: DSC thermogram of [C$_{18:0}$E$_{(2)}$ImMe]I under N$_2$ (cycle 2: cool, cycle 3: heat)
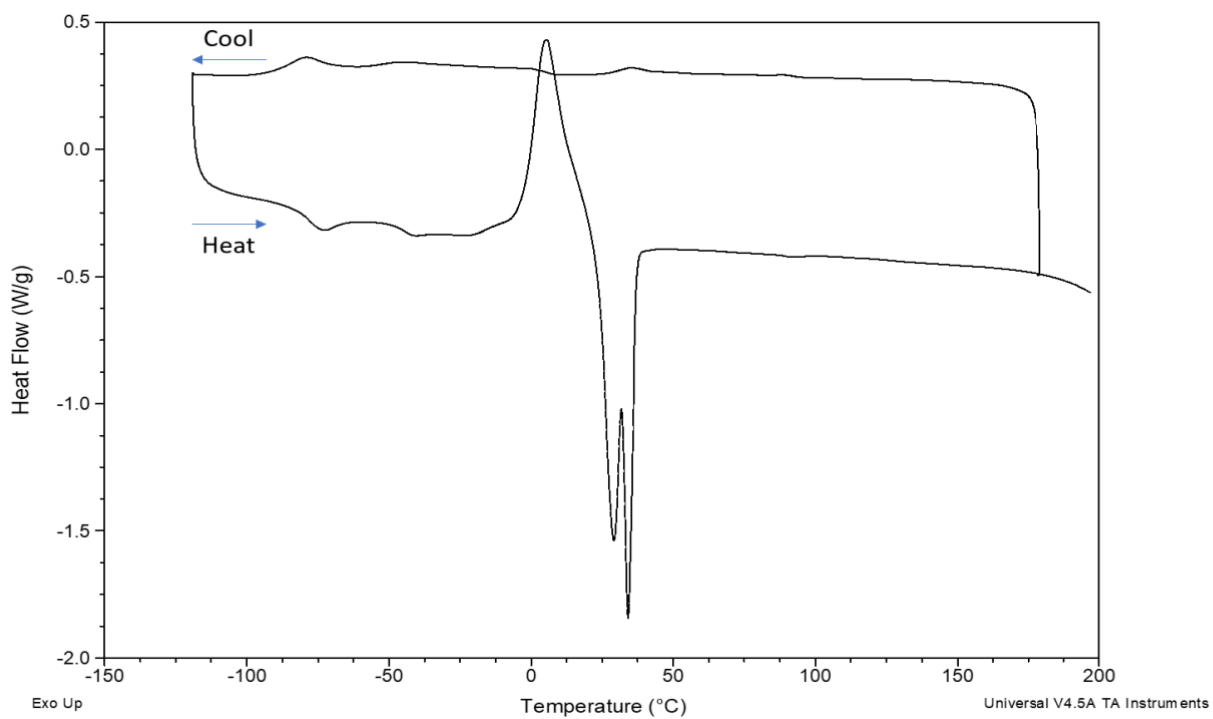


**Figure S59**: DSC thermogram of [C$_{18:1}$E$_{(2)}$ImMe]I under N$_2$ (cycle 2: cool, cycle 3: heat)
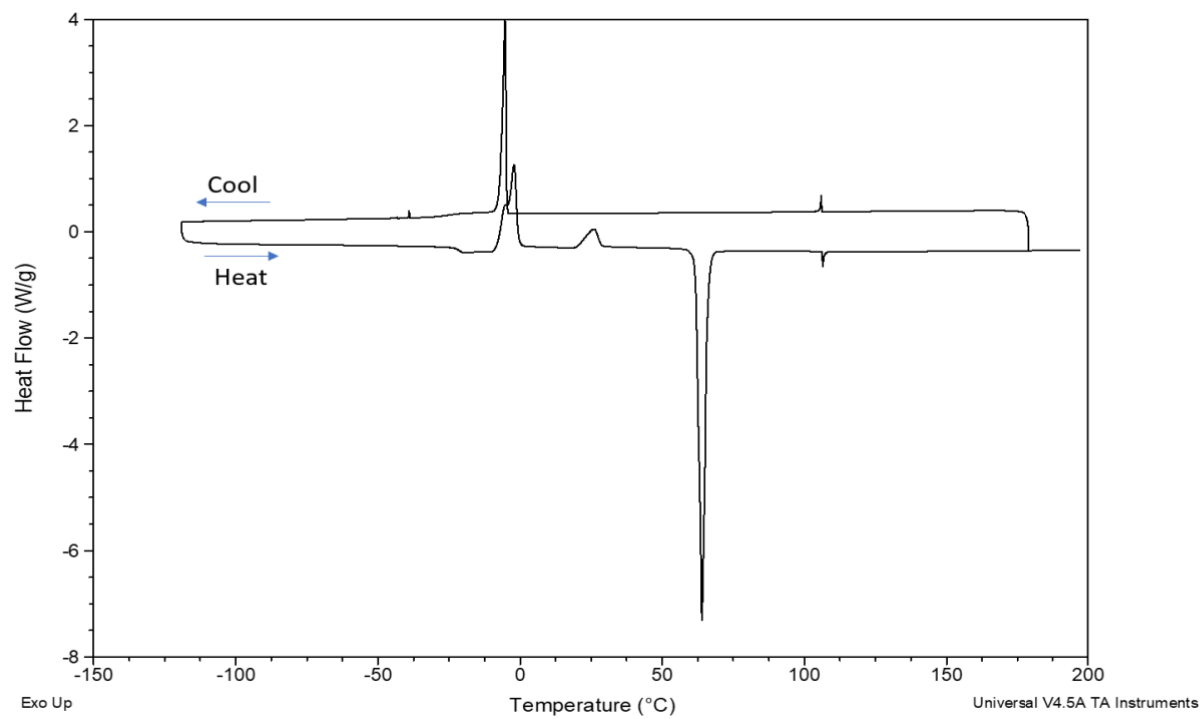
**Figure S60**: DSC thermogram of $[C_{11:0}E_{(2)}ImMe]BF_4$ under $N_2$ (cycle 2: cool, cycle 3: heat)
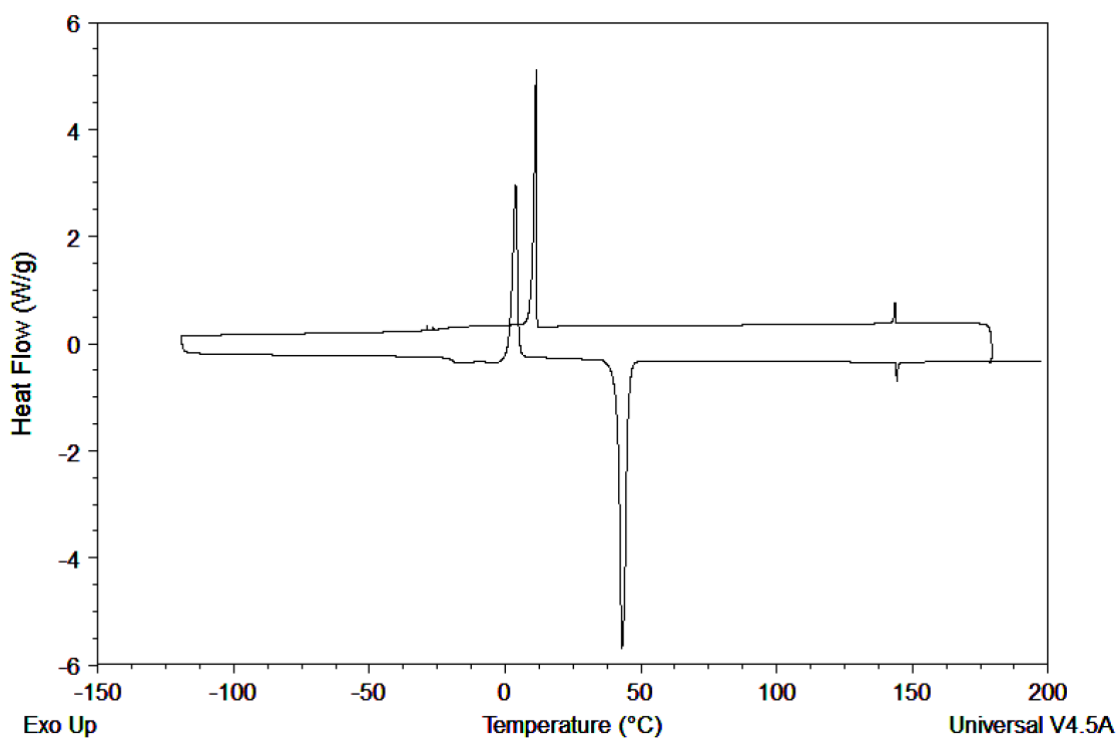


**Figure S61**: DSC thermogram of $[C_{12:0}E_{(2)}ImMe]BF_4$ under $N_2$ (cycle 2: cool, cycle 3: heat)
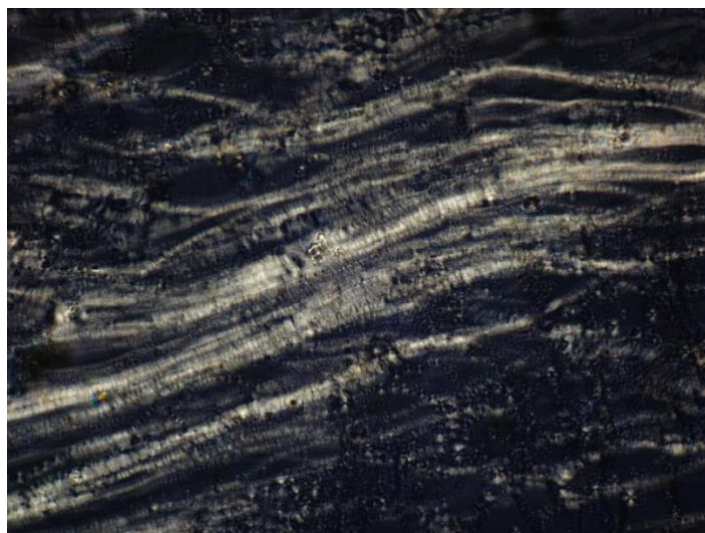
# 8. Polarized optical microscopy (POM) of IL(C)s
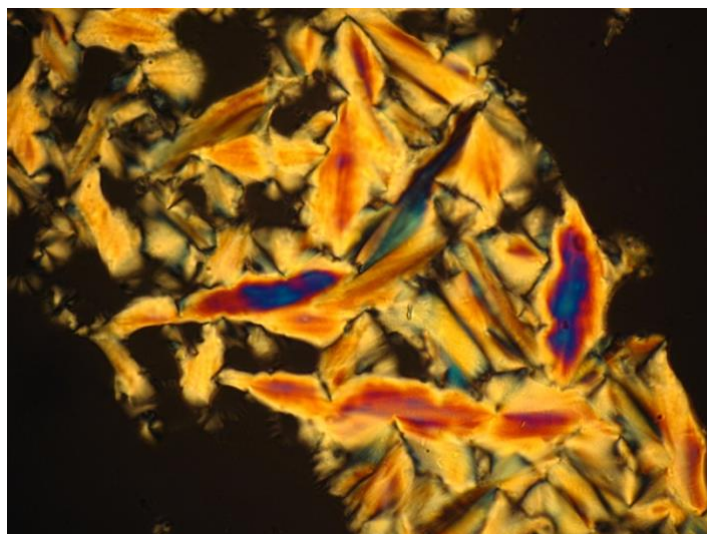


**Figure S62**: Optical microscopic texture of the mesophase (Smectic A) observed under crossed polarizers at elevated temperature for [$C_{12:0}E_{(2)}$ImMe]$p$TsO ($T_m$ = 70 °C, $T_{LC}$ = 78 °C), T = 75 °C (fan-like texture with birefringence).
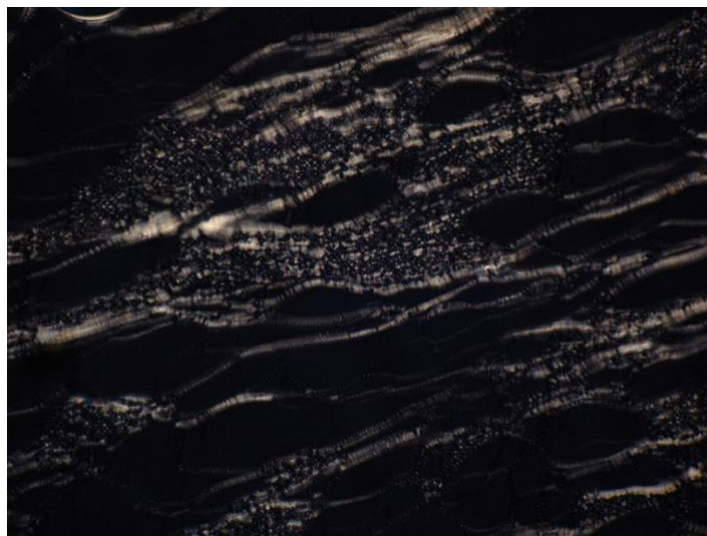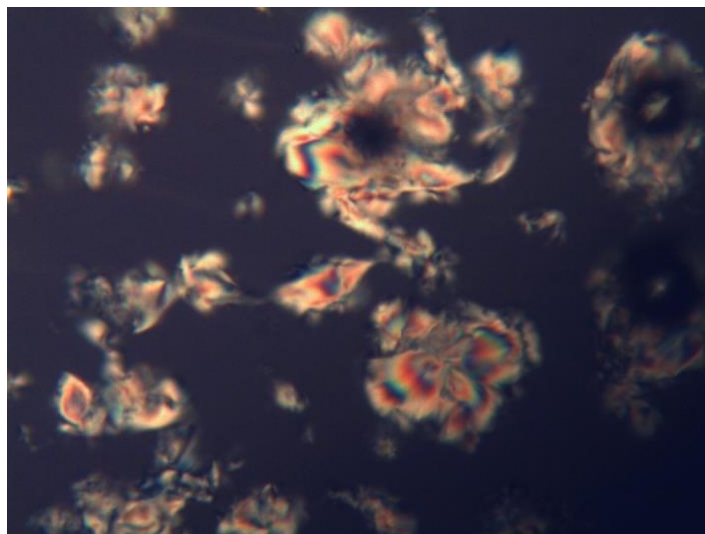


**Figure S63**: Optical microscopic texture of the mesophase (Smectic A) observed under crossed polarizers at elevated temperature for [$C_{18:0}E_{(2)}$ImMe]$p$TsO ($T_m$ = 81 °C, $T_{LC}$ = 172 °C), T = 100 °C (oily streak texture).
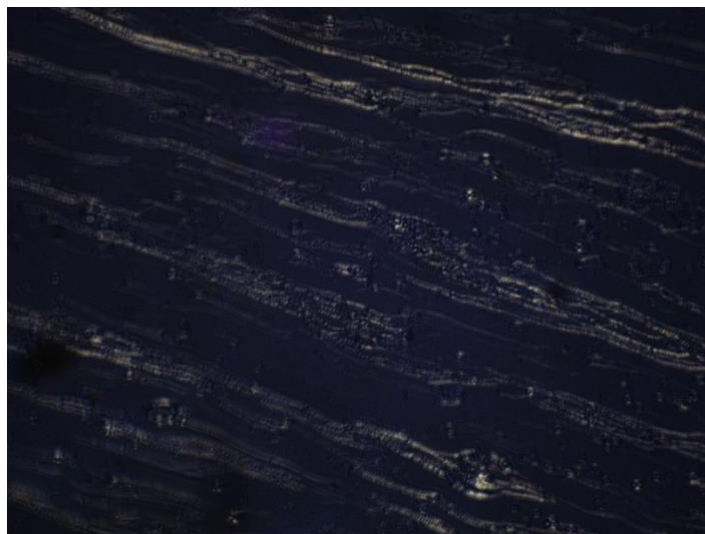
**Figure S64**: Optical microscopic texture of the mesophase (Smectic A) observed under crossed polarizers at elevated temperature for [$C_{18:1}E_{(2)}$ImMe]$p$TsO ($T_m$ = 33 °C, $T_{LC}$ = 148 °C), T = 100 °C (oily streak texture).
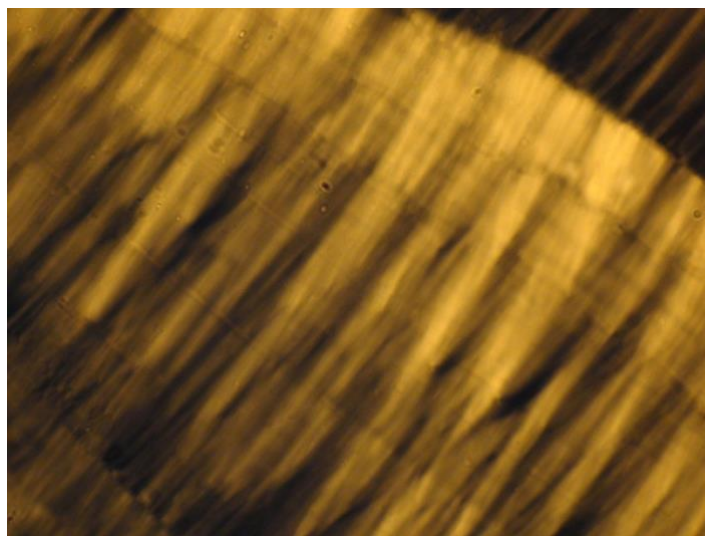


**Figure S65**: Optical microscopic texture of the mesophase (Smectic A) observed under crossed polarizers at elevated temperature for [$C_{12:0}E_{(2)}$ImMe]I ($T_m$ = 63 °C, $T_{LC}$ = 164 °C), T = 110 °C.
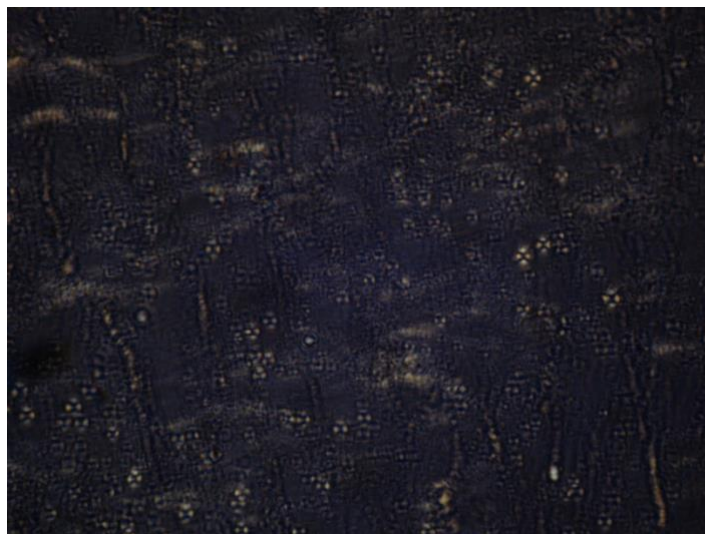
**Figure S66**: Optical microscopic texture of the mesophase (Smectic A) observed under crossed polarizers at elevated temperature for [$C_{18:0}E_{(2)}$ImMe]I ($T_m$ = 81 °C, $T_{LC}$ > 200 °C), T = 100 °C (oily streak texture).



**Figure S67**: Optical microscopic texture of the mesophase (Smectic A) observed under crossed polarizers at elevated temperature for [$C_{18:1}E_{(2)}$ImMe]I ($T_m$ = 29 °C, $T_{LC}$ > 200 °C), T = 100 °C (oily streak texture).

**Figure S68**: Optical microscopic texture of the mesophase (Smectic A) observed under crossed polarizers at elevated temperature for [C$_{12:0}$E$_{(2)}$ImMe]BF$_4$ ($T_m$ = 43 °C, $T_{LC}$ = 144 °C), T = 100 °C.

# 9. Fully extended length of the cations



L = 20.9 Å

$[C_{11:1}E_{(2)}ImMe]$

L = 21.0 Å

$[C_{11:0}E_{(2)}ImMe]$

L = 22.1 Å

$[C_{12:0}E_{(2)}ImMe]$

L = 26.1 Å

$[C_{18:1}E_{(2)}ImMe]$

L = 29.6 Å

$[C_{18:0}E_{(2)}ImMe]$
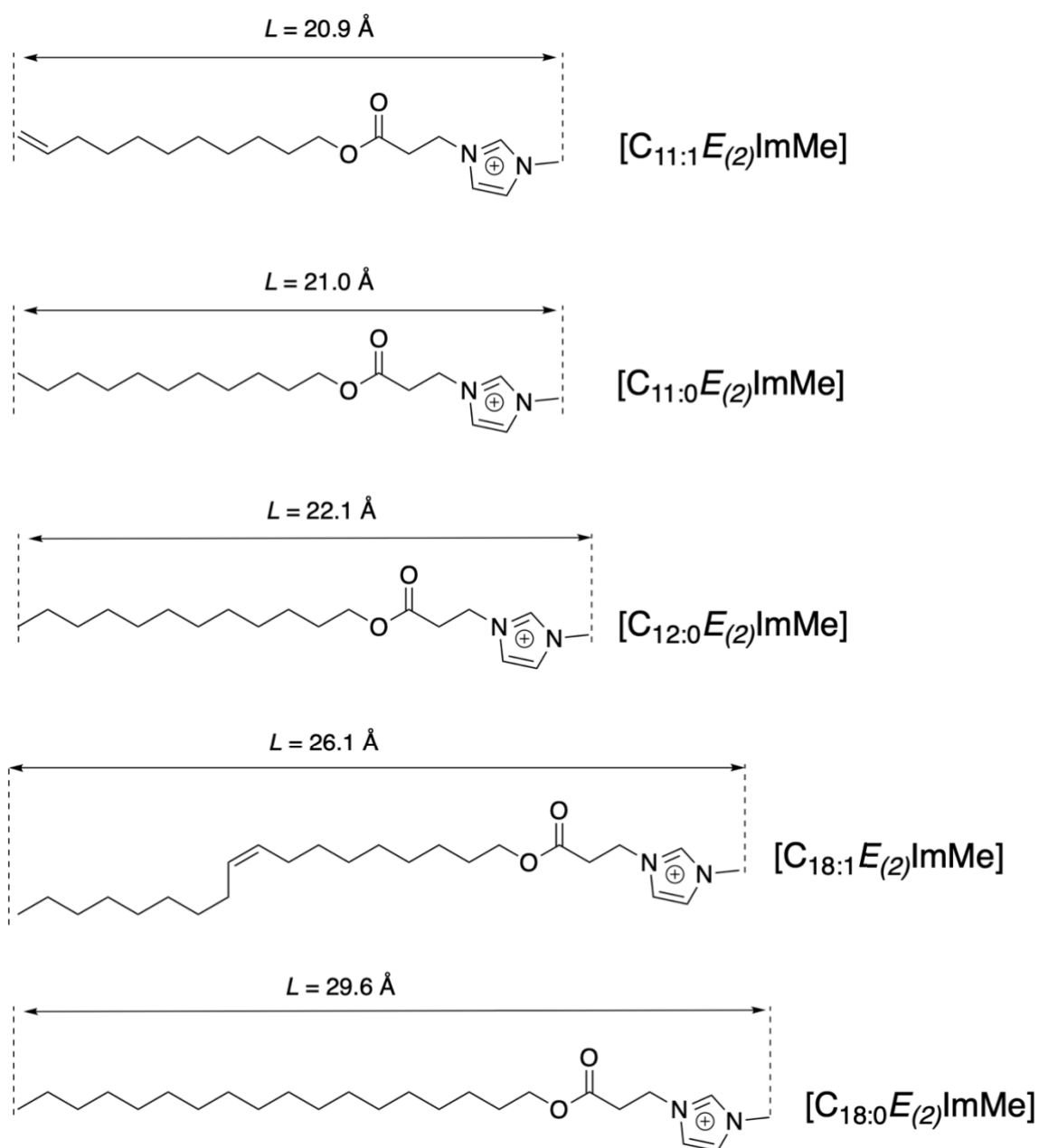
**Figure S69**: Fully extended length of the cation used in this study calculated using Chem3D®

# 10. Temperature dependent Small angle X-ray scattering (SAXS) of IL(C)s
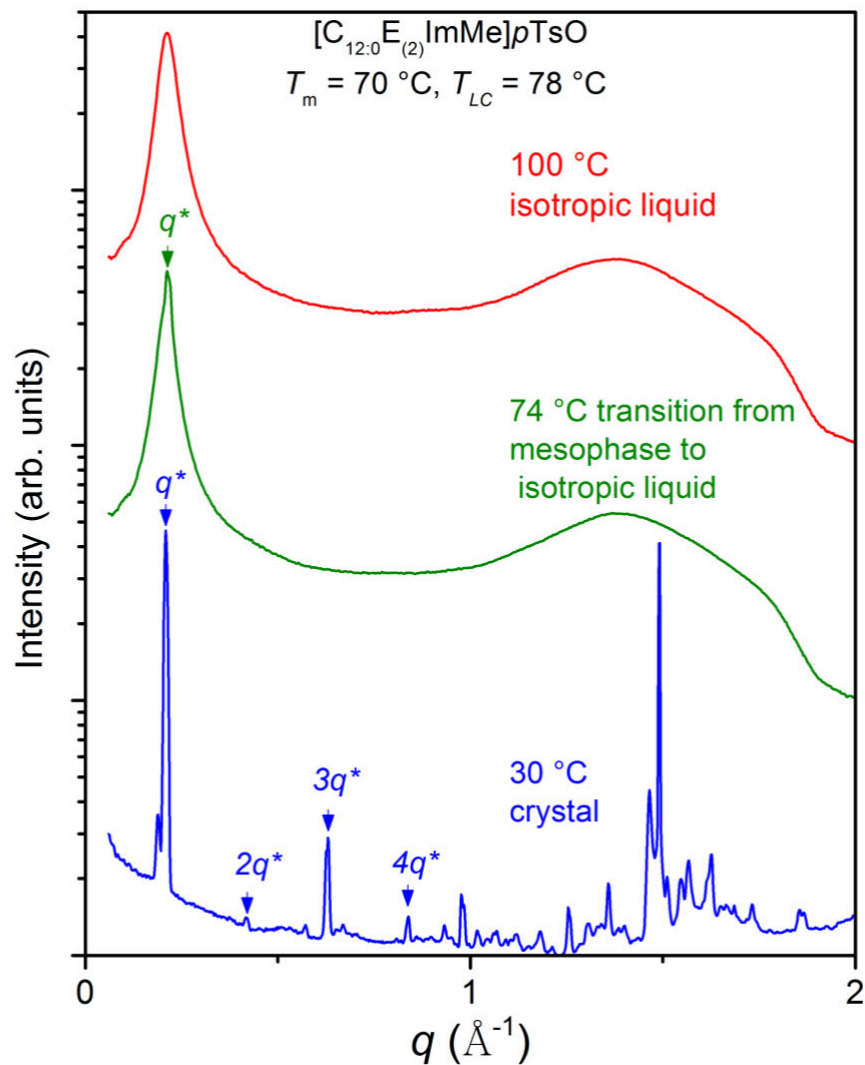


**Figure S70**: Small angle X-ray scattering patterns for [C$_{12:0}$E$_{(2)}$ImMe]pTsO ($T_m$ = 70 °C, $T_{LC}$ = 78 °C) in the crystal (30 °C), the SmA (74 °C) and isotropic (100 °C) phases. The patterns were acquired during a heating cycle. In the crystal phase and the mesophase the principal scattering peak ($q^*$) and the higher order reflection peaks (multiple of $q^*$) are indicated by pointed down triangles.
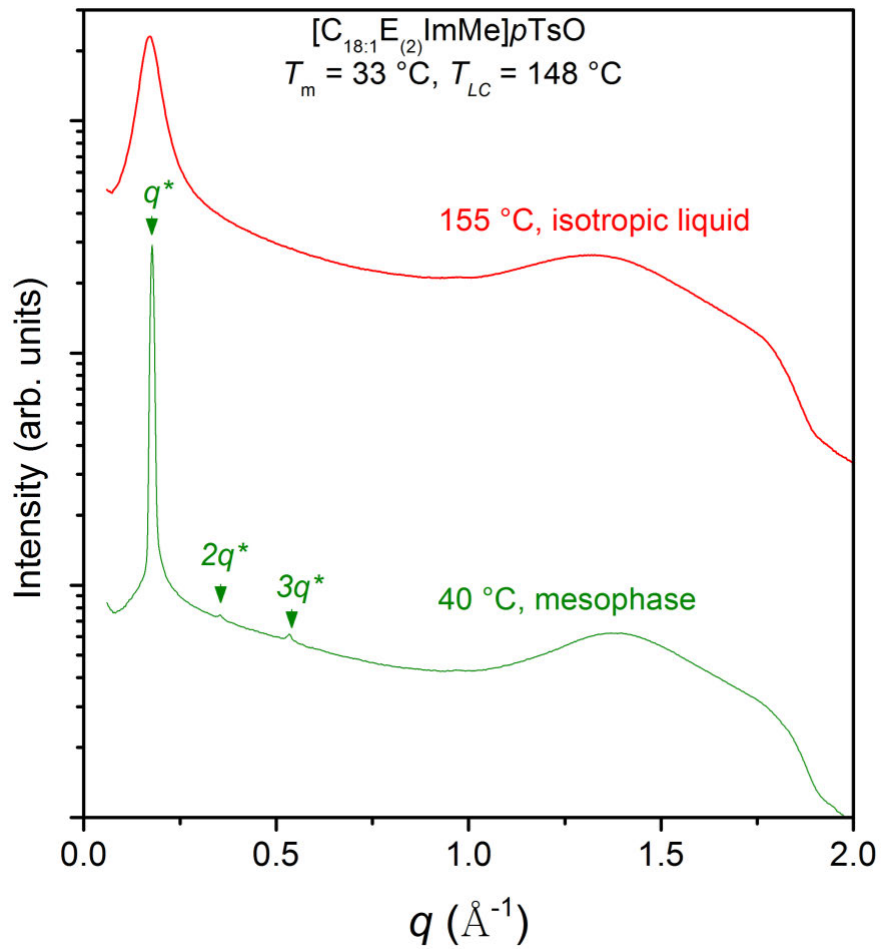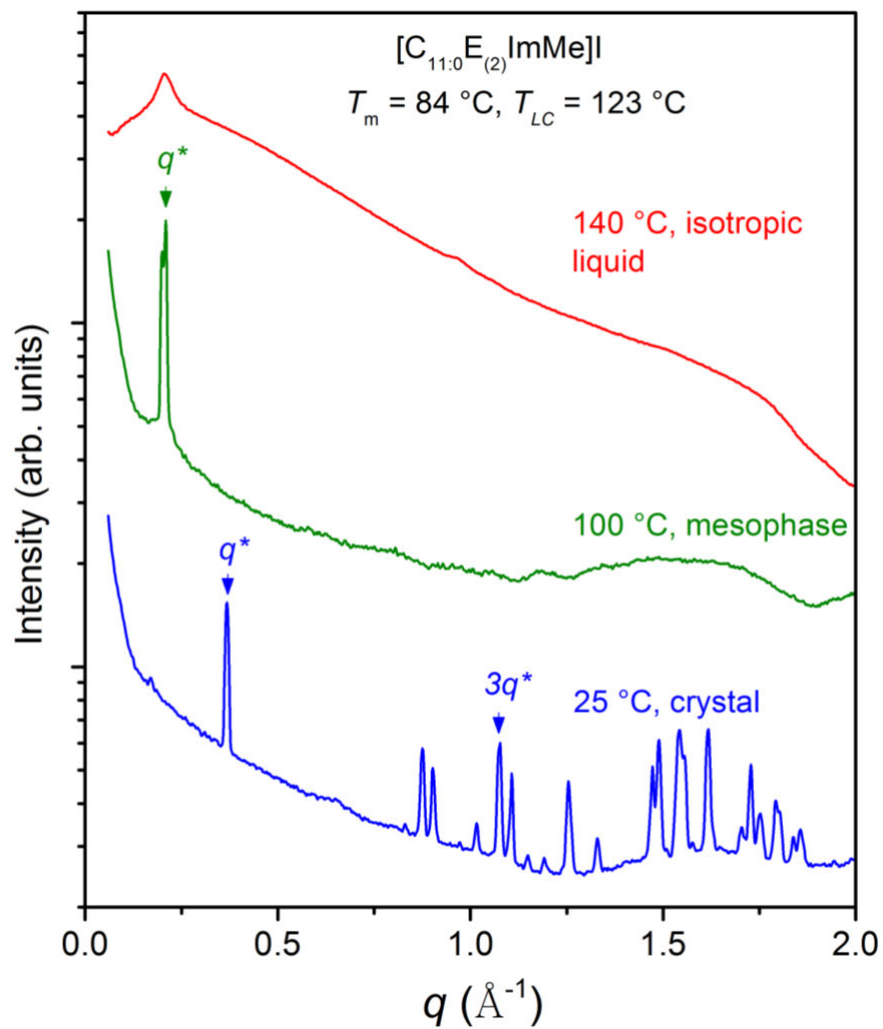
**Figure S71**: Small angle X-ray scattering patterns for [C$_{18:1}$E$_{(2)}$ImMe]pTsO ($T_m$ = 33 °C, $T_{LC}$ = 148 °C) in the SmA (40 °C) and isotropic (155 °C) phases. The patterns were acquired during a heating cycle. In the crystal phase and the mesophase the principal scattering peak ($q*$) and the higher order reflection peaks (multiple of $q*$) are indicated by pointed down triangles.
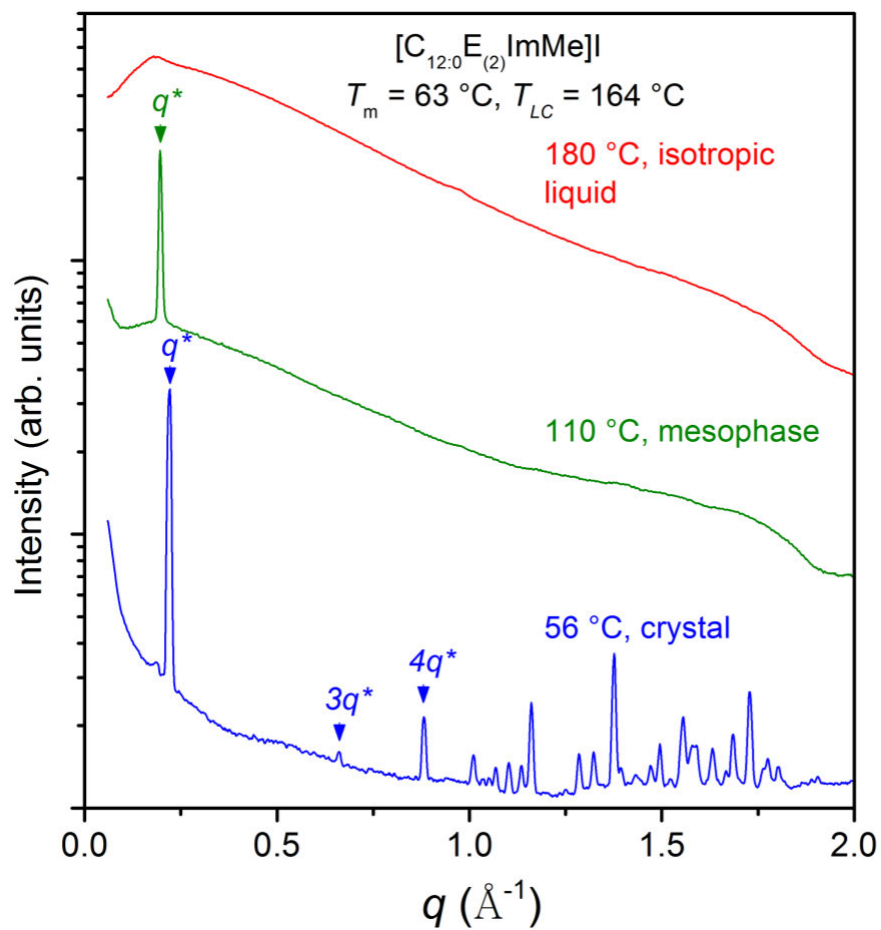
**Figure S72**: Small angle X-ray scattering patterns for [$C_{11:0}E_{(2)}$ImMe]I ($T_m$ = 84 °C, $T_{LC}$ = 123 °C) in the crystal (25 °C), the SmA (100 °C) and isotropic (140 °C) phases. The patterns were acquired during a heating cycle. In the crystal phase and the mesophase the principal scattering peak ($q*$) and the higher order reflection peaks (multiple of $q*$) are indicated by pointed down triangles.
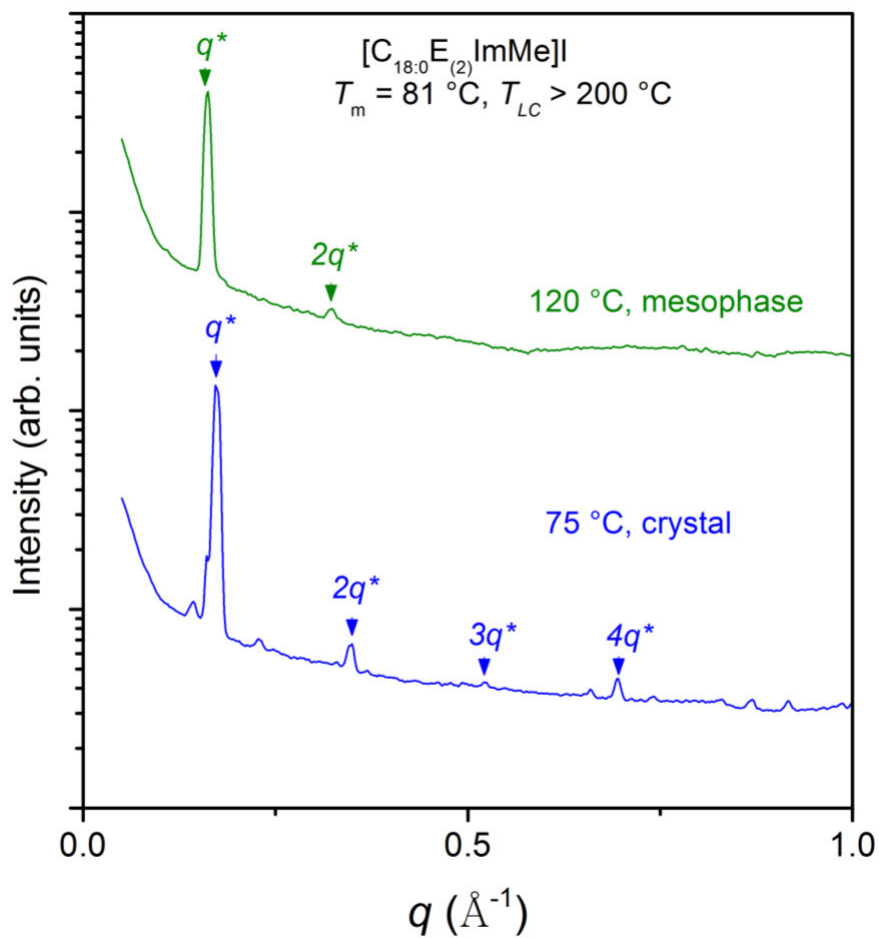
**Figure S73**: Small angle X-ray scattering patterns for [$C_{12:0}E_{(2)}$ImMe]I ($T_m$ = 63 °C, $T_{LC}$ = 164 °C) in the crystal (56 °C), the SmA (110 °C) and isotropic (180 °C) phases. The patterns were acquired during a heating cycle. In the crystal phase and the mesophase the principal scattering peak ($q*$) and the higher order reflection peaks (multiple of $q*$) are indicated by pointed down triangles.

**Figure S74**: Small angle X-ray scattering patterns for [C$_{18:0}$E$_{(2)}$ImMe]I ($T_m$ = 81 °C, $T_{LC}$ > 200 °C) in the crystal (75 °C), the SmA (120 °C) phases. The patterns were acquired during a heating cycle. The principal scattering peak ($q^*$) and the higher order reflection peaks (multiple of $q^*$) are indicated by pointed down triangles.
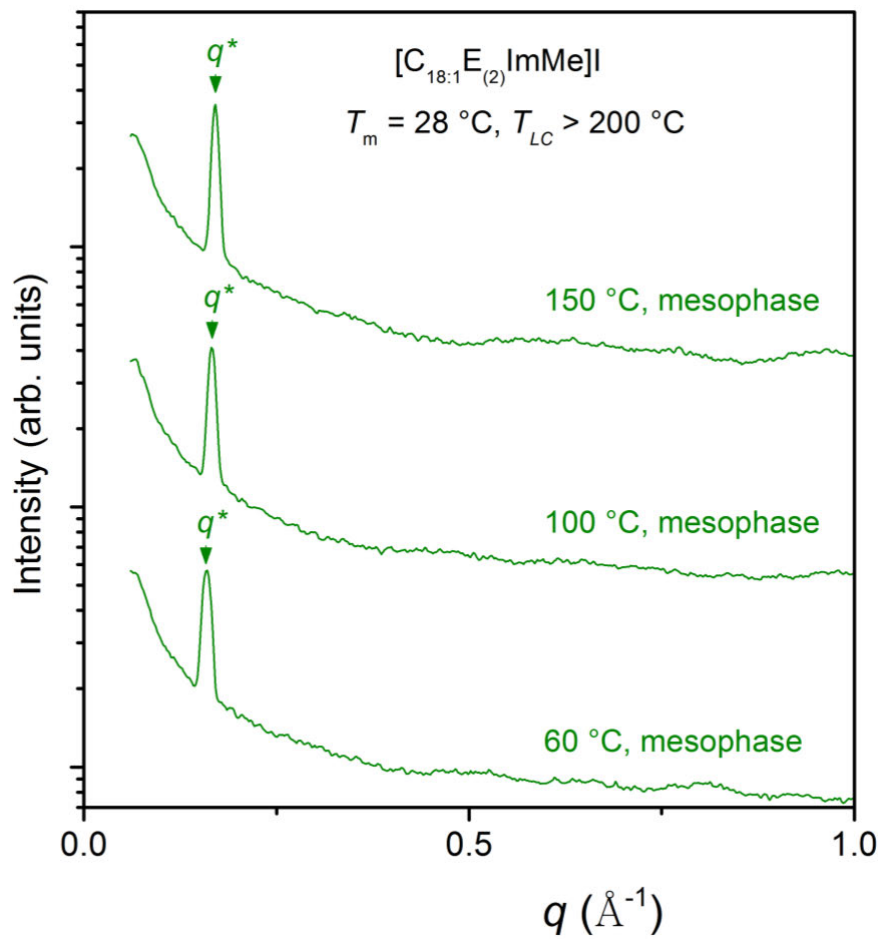
**Figure S75**: Small angle X-ray scattering patterns for [C$_{18:1}$E$_{(2)}$ImMe]I ($T_m$ = 81 °C, $T_{LC}$ > 200 °C) in the SmA phase (60 °C, 100 °C and 150 °C). The patterns were acquired during a heating cycle. The principal scattering peak ($q*$) is indicated by a pointed down triangle.
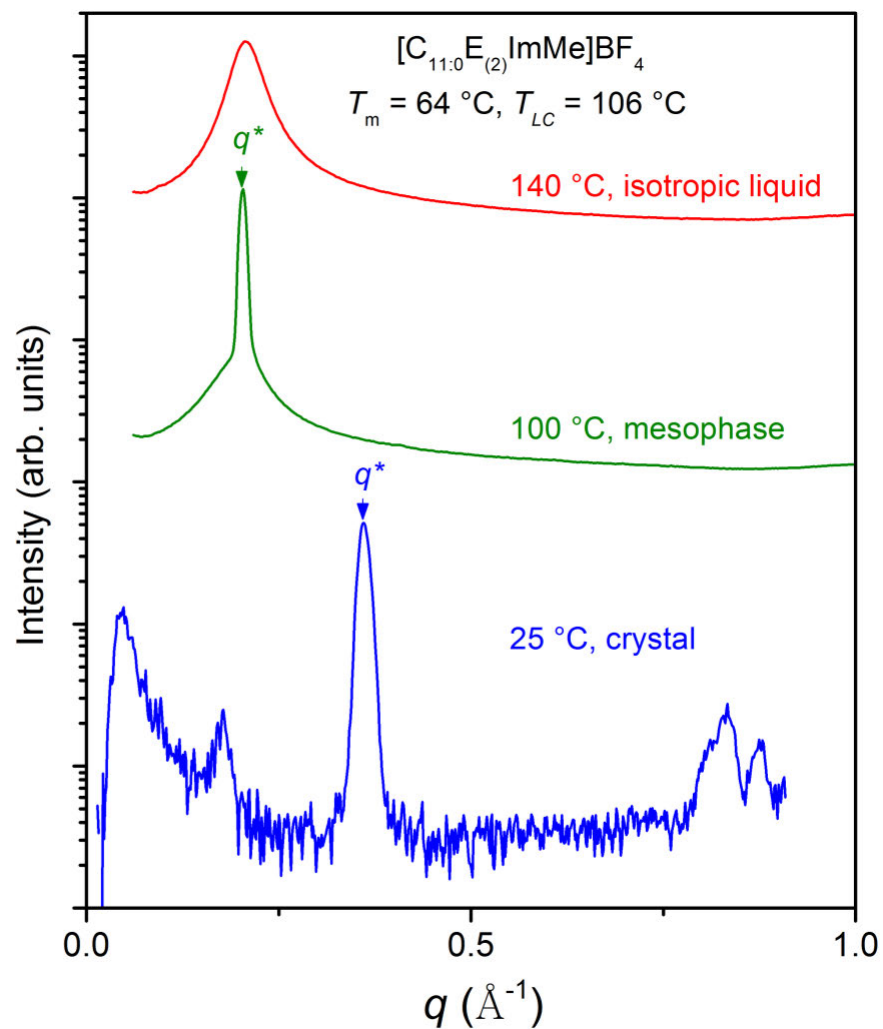
**Figure S76**: Small angle X-ray scattering patterns for [C$_{11:0}$E$_{(2)}$ImMe]BF$_4$ ($T_m$ = 64 °C, $T_{LC}$ = 106 °C) in the crystal (25 °C), the SmA (100 °C) and isotropic (140 °C) phases. The patterns were acquired during a heating cycle. In the crystal phase and the mesophase the principal scattering peak ($q$*) is indicated by a pointed down triangle.
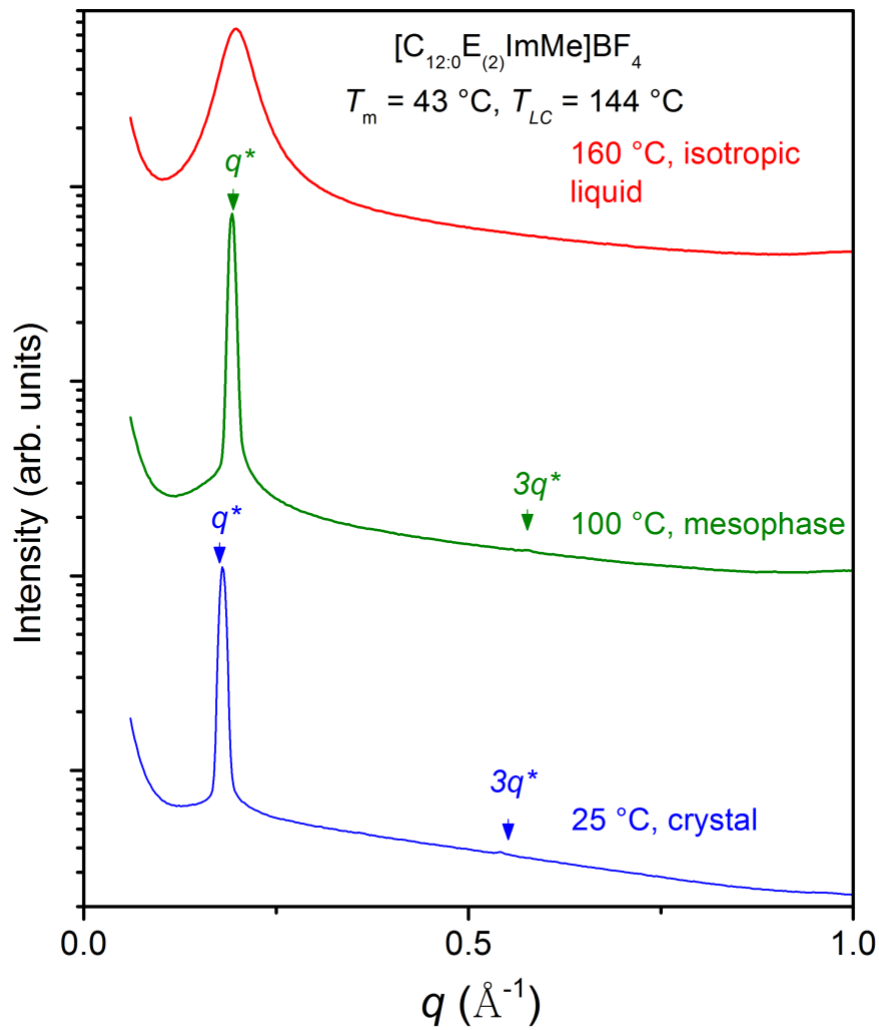
**Figure S77**: Small angle X-ray scattering patterns for [$C_{12:0}E_{(2)}$ImMe]BF$_4$ ($T_m$ = 43 °C, $T_{LC}$ = 144 °C) in the crystal (25 °C), the SmA (100 °C) and isotropic (160 °C) phases. The patterns were acquired during a heating cycle. In the crystal phase and the mesophase the principal scattering peak ($q*$) and the higher order reflection peaks (multiple of $q*$) are indicated by pointed down triangles.

# 11. Single crystal X-ray analysis

| | [C$_{18:0}$E$_{(2)}$ImMe]$p$TsO | [C$_{11:0}$E$_{(2)}$ImMe]I | [C$_{11:0}$E$_{(2)}$ImMe]BF$_4$ |
|---|---|---|---|
| Empirical formula | C$_{32}$ H$_{54}$ N$_2$ O$_5$ S | C$_{18}$ H$_{33}$ N$_2$ O$_2$,I | C$_{18}$ H$_{33}$ N$_2$ O$_2$,B F$_4$ |
| Formula weight (g mol$^{-1}$) | 578.38 | 436.16 | 396.26 |
| Crystal system | Monoclinic | Monoclinic | Monoclinic |
| Space group | $P2_1/c$ | $Pc$ | $P2_1/c$ |
| $a$, Å | 35.58(2) | 17.5768(12) | 17.223(4) |
| $b$, Å | 9.775(5) | 8.2962(2) | 8.252(2) |
| $c$, Å | 9.355(5) | 14.8556(14) | 15.149(4) |
| $\alpha$, ° | 90 | 90 | 90 |
| $\beta$, ° | 93.501(19) | 102.766(7) | 99.137(4) |
| $\gamma$, ° | 90 | 90 | 90 |
| Volume, Å$^3$ | 3247.55 | 2112.7 | 2125.72 |
| $Z$ | 4 | 4 | 4 |
| $\rho$ (g cm$^{-3}$) (calculated) | 1.18 | 1.37 | 1.24 |

**Table S2**: Crystal data for [C$_{18:0}$E$_{(2)}$ImMe]$p$TsO, [C$_{11:0}$E$_{(2)}$ImMe]I and [C$_{11:0}$E$_{(2)}$ImMe]BF$_4$
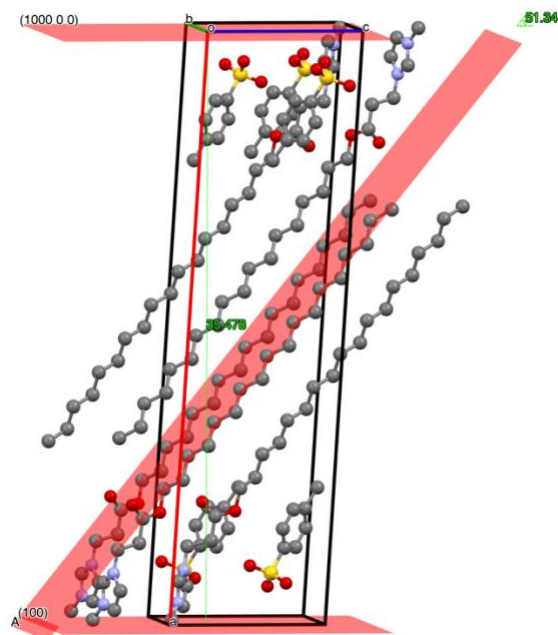


**Figure S78**: The crystal structure of [C$_{18:0}$E$_{(2)}$ImMe]$p$TsO at 25 °C. The distance between the plan (1 0 0) and (1000 0 0) provide the layer distance, $d_{Cr}$ = 35.5 Å. The plan A, formed by symmetrical alkyl chains, intersect plan (1 0 0) and (1000 0 0) with an angle, $\alpha$ = 51.34°. Thus, the tilt angle of the alkyl chains as compared to the layer normal is, $\theta$ = 90° - $\alpha \sim$ 39°
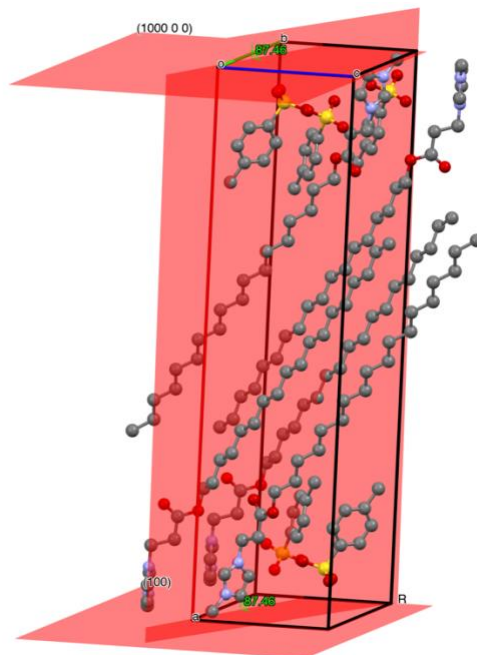
**Figure S79**: The crystal structure of [C$_{18:0}$E$_{(2)}$ImMe]$p$TsO at 25 °C. Plan R is the plan define by the imidazolium ring of a cation. It intersects plan (1 0 0) and (1000 0 0) with an angle $\alpha$ = 87.46°.

The presence of O···H—C weak hydrogen bonds was assessed according to prevailing conventions using the Van der Waals radii of O and C, $R_O$ and $R_C$ respectively. If the O↔C distance is inferior or equal to the sum of the Van der Waals radii of O and C, then a weak hydrogen bond exists, *i.e.*, O↔C ≤ $R_O$ + $R_C$.[8]

The Van der Waals radii[9, 10] $R_X$ are given in Table S3, $R_O$ + $R_C$ = 3.22 Å.

| Atom | X | $R_X$, Å |
|---|---|---|
| Carbon | C | 1.70 |
| Oxygen | O | 1.52 |

**Table S3**: Van der Waals radii

With this convention in hand, the tosylate anion of [C$_{18:0}$E$_{(2)}$ImMe]$p$TsO develops O···H—C weak hydrogen bonds with four cations located within the same layer. One of the oxygens interacts with the C2 carbon of two imidazolium head group (O↔C distance, 3.075 Å and 2.980 Å, Figure S68). Another of the oxygens interacts with the C5 carbon of one imidazolium head group (O↔C distance, 3.190 Å, Figure S68). And another of the oxygens interacts with the carbon in alpha position to the carbonyl group (O↔C distance, 3.196 Å, Figure S69).

A tosylate anion from the in-front bilayer can also develop weak hydrogen bonds with the carbon of the methyl group of an imidazolium head group, as depicted in Figure S68 (O↔C distance, 3.298 Å). It is worth noting that in that case, O↔C is slightly superior to $R_O$ + $R_C$ (3.22 Å). However, 3.6 Å is often consider as the threshold value to rule out the presence of O···H—C weak hydrogen bonds.[8]
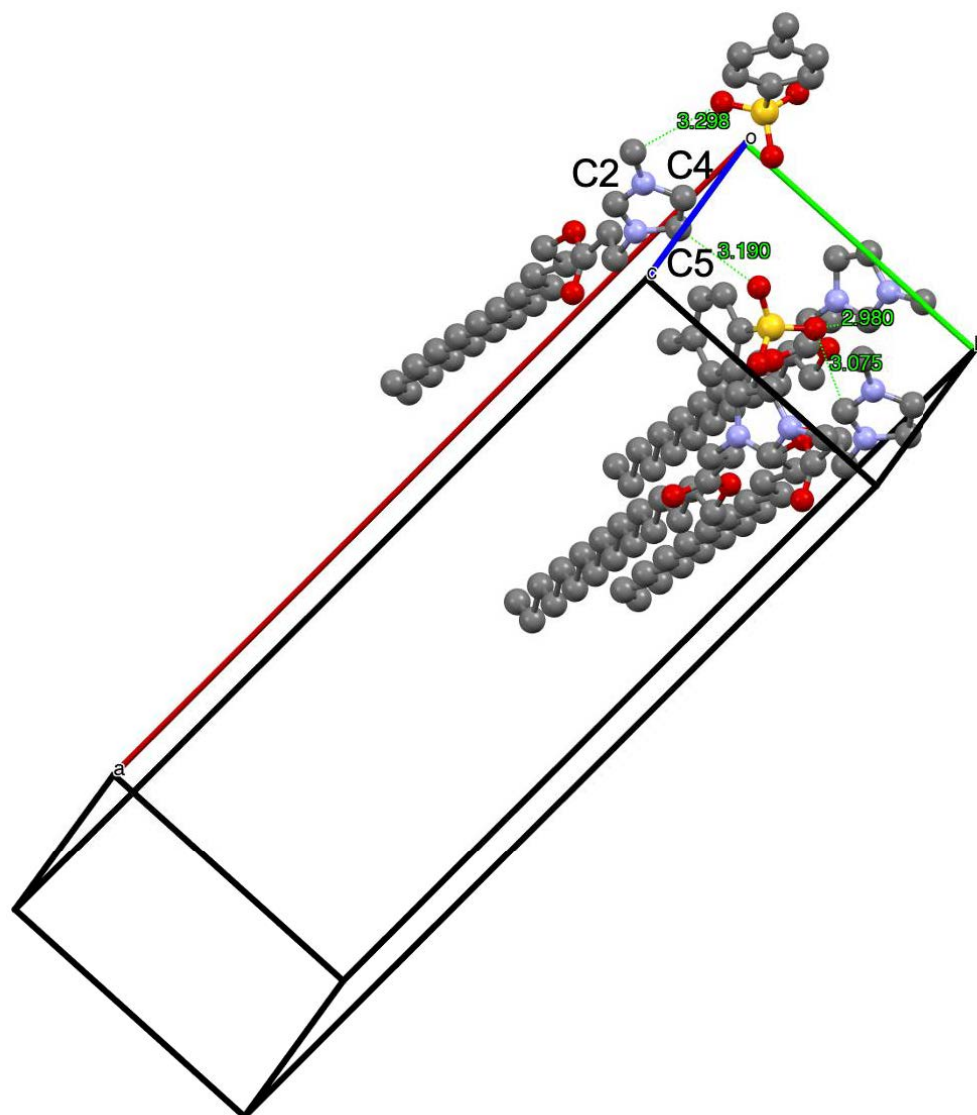
**Figure S80**: Visualization of the distances between the atoms developing weak hydrogen bonds in the crystal structure of [C$_{18:0}$E$_{(2)}$ImMe]$p$TsO. These weak hydrogen bonds are formed between the tosylate anion and the imidazolium head groups both inside a bilayer and in-between neighboring layers.
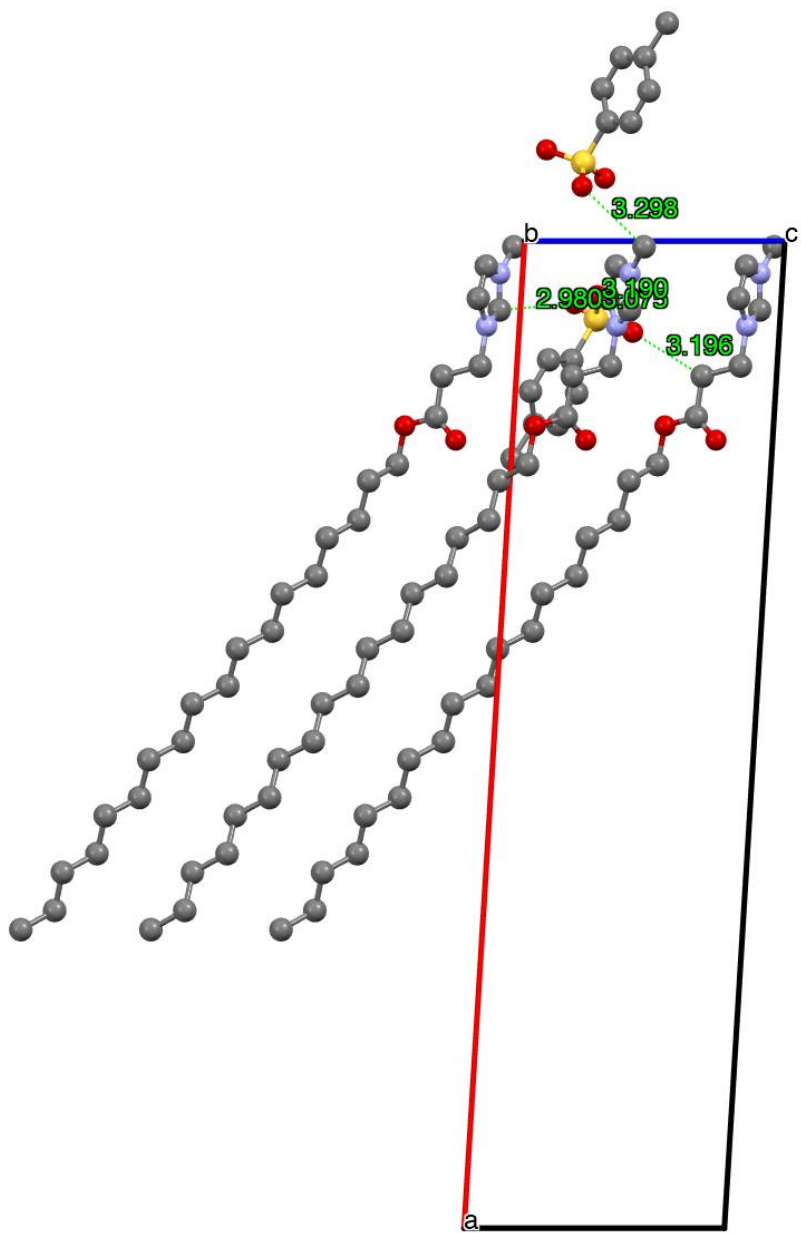
**Figure S81**: Visualization of the distances between the atoms developing weak hydrogen bonds in the crystal structure of [C$_{18:0}$E$_{(2)}$ImMe]$p$TsO. These weak hydrogen bonds are formed between the tosylate anion and the imidazolium head groups both inside a bilayer and in-between neighboring layers. View along b axis for a special emphasize on the weak hydrogen bond developed between one oxygen of the tosylate group and the carbon in alpha position to the carbonyl group (O↔C distance, 3.196 Å).
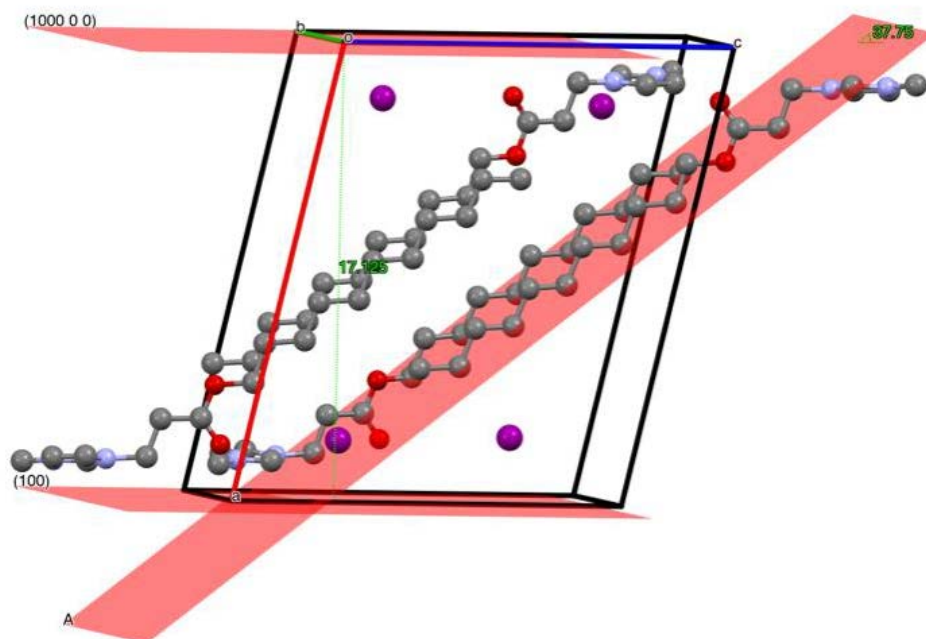
**Figure S82**: The crystal structure of [$C_{11:0}E_{(2)}$ImMe]I at 25 °C. The distance between the plan (1 0 0) and (1000 0 0) provide the layer distance, $d_{Cr}$ = 17.1 Å. The plan A, formed by symmetrical alkyl chains, intersect plan (1 0 0) and (1000 0 0) with an angle, $\alpha$ = 37.75°. Thus, the tilt angle of the alkyl chains as compared to the layer normal is, $\theta$ = 90° - $\alpha \sim 52°$

The oxygen of the carbonyl groups of [$C_{11:0}E_{(2)}$ImMe]I develops O···H−C weak hydrogen bonds with two cations located within the same layer. It interacts with the C4 and C5 carbons of one imidazolium head group (O↔C distance, 3.062 Å and 3.210 Å, respectively, Figure S71a) and with the carbon of the methyl group of another imidazolium head group (O↔C distance, 3.200 Å, Figure S71a).

It also develops weak hydrogen bonds with the carbon of the methyl group of imidazolium head groups located in the in-front layer, as depicted in Figure S71b (O↔C distance, 3.484 Å). It is worth noting that in that case, O↔C is slightly superior to $R_O + R_C$ (3.22 Å). However, 3.6 Å is often consider as the threshold value to rule out the presence of O···H−C weak hydrogen bonds.[8]
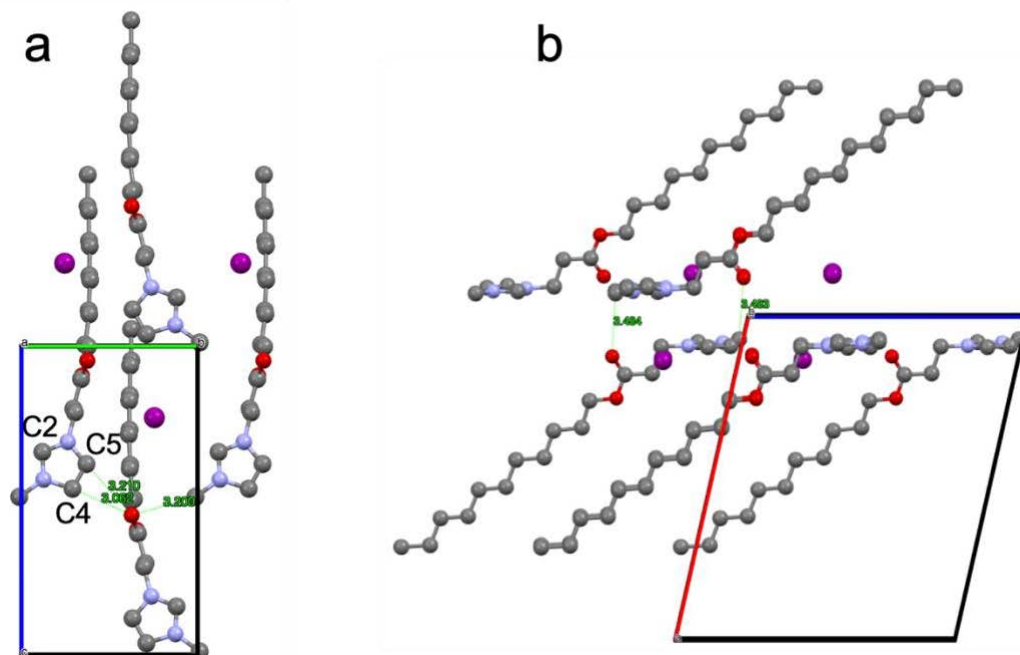
**Figure S83**: Visualization of the distances between the atoms developing weak hydrogen O···H−C bonds in the crystal structure of [$C_{11:0}E_{(2)}$ImMe]I. These weak hydrogen bonds are formed between the carbonyle groups and the imidazolium head groups both inside a bilayer (a) and in-between neighboring layers (b).
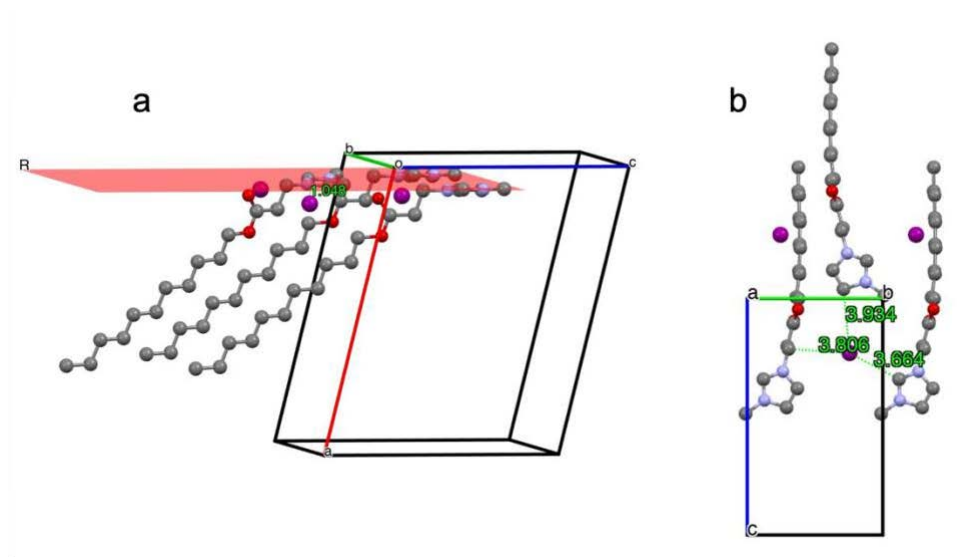


**Figure S84**: (a) Localization of the iodide anion as compared to the plan, R, formed by the imidazolium head group in the crystal structure of [$C_{11:0}E_{(2)}$ImMe]I. (b) The iodide anion is located in the center of the triangle formed by the imidazolium rings of three cations. It develops weak interactions with one hydrogen per surrounding cation (Hydrogen located on the carbon with I↔C≤ $R_I$ + $R_C$, where $R_I$ = 2.10 Å[10]).
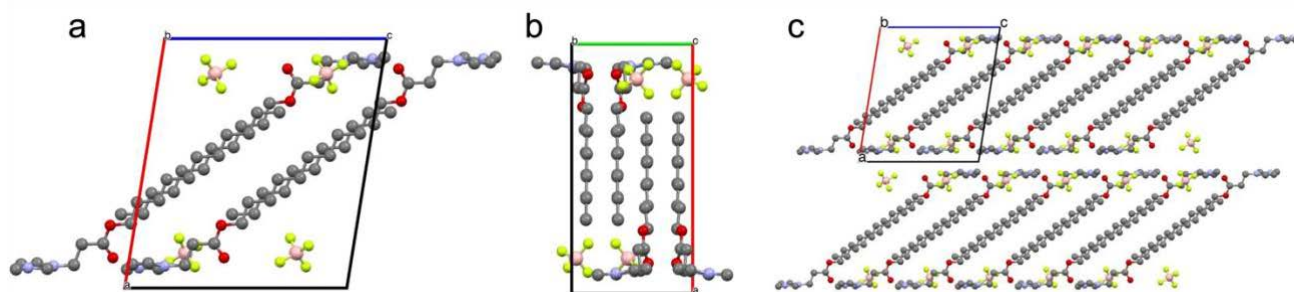
**Figure S85**: Crystal structure of $[C_{11:0}E_{(2)}ImMe]BF_4$ at 25 °C. (a) unit cell along *b* axis, (b) unit cell along *c* axis, (c) overall bilayer structure showing the interdigitation and the tilted alkyl chains along *b* axis.
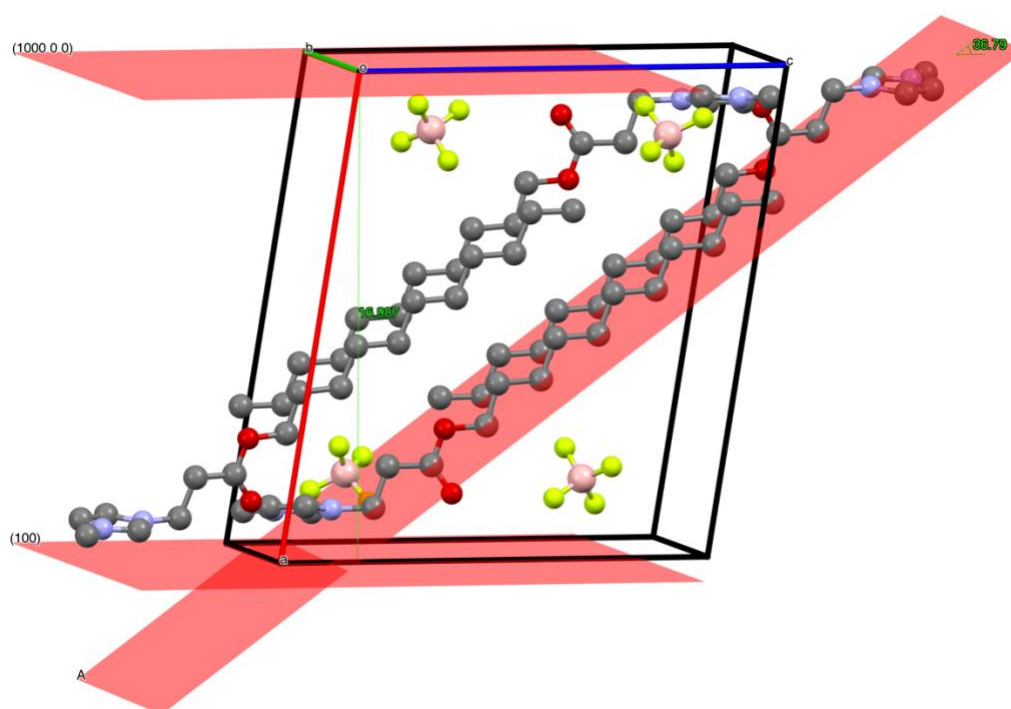


**Figure S86**: The crystal structure of $[C_{11:0}E_{(2)}ImMe]BF_4$ at 25 °C. The distance between the plan (1 0 0) and (1000 0 0) provide the layer distance, $d_{Cr}$ = 17.0 Å. The plan A, formed by symmetrical alkyl chains, intersect plan (1 0 0) and (1000 0 0) with an angle, $\alpha$ = 36.79°. Thus, the tilt angle of the alkyl chains as compared to the layer normal is, $\theta$ = 90° - $\alpha \sim$ 53°

# 12. References

1.      Sheldrick, G. M., A short history of SHELX. *Acta Crystallographica a-Foundation and Advances* **2008,** *64*, 112-122.

2.      Khong, S. N.; Kwon, O., Chiral Aminophosphines as Catalysts for Enantioselective Double-Michael Indoline Syntheses. *Molecules* **2012,** *17* (5), 5626-5650.

3.      Efimova, A.; Varga, J.; Matuschek, G.; Saraji-Bozorgzad, M. R.; Denner, T.; Zimmermann, R.; Schmidt, P., Thermal Resilience of Imidazolium-Based Ionic Liquids-Studies on Short- and Long-Term Thermal Stability and Decomposition Mechanism of 1-Alkyl-3-methylimidazolium Halides by Thermal Analysis and Single-Photon Ionization Time-of-Flight Mass Spectrometry. *Journal of Physical Chemistry B* **2018,** *122* (37), 8738-8749.

4.      Garcia, M. T.; Ribosa, I.; Perez, L.; Manresa, A.; Comelles, F., Aggregation Behavior and Antimicrobial Activity of Ester-Functionalized Imidazolium- and Pyridinium-Based Ionic Liquids in Aqueous Solution. *Langmuir* **2013,** *29* (8), 2536-2545.

5.      Maton, C.; De Vos, N.; Stevens, C. V., Ionic liquid thermal stabilities: decomposition mechanisms and analysis tools. *Chemical Society Reviews* **2013,** *42* (13), 5963-5977.

6.      Ohtani, H.; Ishimura, S.; Kumai, M., Thermal Decomposition Behaviors of Imidazolium-type Ionic Liquids Studied by Pyrolysis-Gas Chromatography. *Analytical Sciences* **2008,** *24* (10), 1335-1340.

7.      Garcia, M. T.; Gathergood, N.; Scammells, P. J., Biodegradable ionic liquids - Part II. Effect of the anion and toxicology. *Green Chemistry* **2005,** *7* (1), 9-14.

8.      Lakshmi, B.; Samuelson, A. G.; Jose, K. V. J.; Gadre, S. R.; Arunan, E., Is there a hydrogen bond radius? Evidence from microwave spectroscopy, neutron scattering and X-ray diffraction results. *New Journal of Chemistry* **2005,** *29* (2), 371-377.

9.      Bondi, A., VAN DER WAALS VOLUMES + RADII. *Journal of Physical Chemistry* **1964,** *68* (3), 441-+.

10.     Batsanov, S. S., Van der Waals radii of elements. *Inorganic Materials* **2001,** *37* (9), 871-885.